



regime. Self-starting characteristics of these new designs are also characterized; results indicate that two new designs can maintain self-starting capability into the Mach 6-7 range. Full external and internal flow properties of the new designs are determined using the characteristics model. Mach number, total pressure ratio, temperature, pressure and mass flow properties (and their levels of distortion) are quantified at the inlet exit plane for all cases considered.

AXISYMMETRIC INLET DESIGN FOR COMBINED CYCLE ENGINES

By

Jesse R. Colville

Thesis submitted to the Faculty of the Graduate School of the  
University of Maryland, College Park, in partial fulfillment  
of the requirements for the degree of  
Master of Science  
2005

Advisory Committee:  
Professor Mark J. Lewis, Chairman/Advisor  
Associate Professor Kenneth Yu  
Assistant Professor Christopher Cadou

© Copyright by  
Jesse R. Colville  
2005

## **DEDICATION**

To my parents, Donald and Diane Colville, for their support through the first twenty-three years of my life (including the turbulent times).

## **ACKNOWLEDGEMENTS**

First and foremost, I have to thank my advisor Dr. Mark J. Lewis. His advice, guidance and support have been unwavering since I first approached his office as a measly little sophomore in September of 2000. Second, I would like to thank my committee members, Dr. Kenneth Yu and Dr. Christopher Cadou, for their time and constructive criticism in critiquing this thesis.

An exorbitant amount of appreciation is expressed to Dr. Ryan Starkey for essentially being my mentor for the past four to five years. I honestly do not know where I would be at in this work without your help and insight. Thank you for letting me bug you so often without you (at least openly) getting annoyed! Maybe I'll see you at Aerojet in 2 years!

I would also like to express some gratitude to those who backed this project. This work has been sponsored by the Space Vehicle Technology Institute, under grant NCC3-989, one of the NASA University Institutes, with joint sponsorship from the Department of Defense. Appreciation is expressed to Claudia Meyer, Mark Klem and Harry Cikanek of the NASA Glenn Research Center, and to Dr. John Schmisser and Dr. Walter Jones of the Air Force Office of Scientific Research.

Now to the office. Thank you to Andy, Justin, Kerrie, Josh, Marc, Greg, Amardip, etc. for creating a comfortable atmosphere in which to work in and for putting up with my insanity and outbursts while finishing this work (and whenever Andy bugs me!).

I also have to thank my entire family for their love and support from day one. I know I have not been the easiest child to raise or brother to befriend, but you all have stood by and helped me grow.

Finally, I have to thank my fiancée Michelle. You have been my crutch for the past three years. You have put up with every one of my mood swings and dealt with the many, many six to seven day work weeks that I had to undertake the past two years. You are now about to venture across the country with me as I move on into the industry. I can only hope to be able to fully repay you at some point in the future.

## TABLE OF CONTENTS

ABSTRACT.....	i
DEDICATION.....	ii
ACKNOWLEDGEMENTS.....	iii
TABLE OF CONTENTS.....	v
LIST OF FIGURES.....	viii
LIST OF SYMBOLS.....	xii
1 Introduction.....	1
1.1 Motivation.....	1
1.2 Inlet Design.....	1
1.2.1 Previous Work.....	5
1.3 Objective.....	16
2 Model Development.....	19
2.1 Program Description.....	19
2.2 Method of Characteristics.....	20
2.2.1 Supersonic Potential Flow with Axial Symmetry.....	21
2.2.2 Supersonic Rotational Flow with Axial Symmetry.....	22

2.3	Solution Procedure.....	23
2.3.1	Initial Data Line .....	24
2.3.2	Flowfield Calculations .....	27
2.3.3	Shock Point Calculations .....	31
2.3.4	Isentropic Flow Procedure .....	36
2.4	Thermodynamic Relations .....	37
2.4.1	Flowfield Relations .....	37
2.4.2	Shock Relations .....	38
3	SR-71-Type Inlet Analysis & Results.....	40
3.1	Geometry Definition .....	40
3.2	Self-Starting Characteristics .....	42
3.3	Flowfield Properties.....	44
3.4	Throat Conditions .....	51
4	CFD Validation.....	55
4.1	Inviscid Analysis.....	55
4.2	Viscous Analysis.....	62
5	Modification Analysis & Results.....	65
5.1	Re-extension of the Original Inlet.....	66
5.1.1	Self-Starting Characteristics .....	66
5.1.2	Flowfield Properties.....	67
5.1.3	Throat Conditions .....	72
5.2	Variable Cowl Leading Edge.....	76
5.2.1	Self-Starting Characteristics .....	76

5.3	Re-extension with a Widened Shoulder.....	77
5.3.1	Self-Starting Characteristics .....	78
5.3.2	Flowfield Properties.....	79
5.3.3	Throat Conditions .....	85
5.4	Variable Cone Centerbody.....	88
5.4.1	Self-Starting Characteristics .....	89
5.5	Variable Cone Centerbody with Re-extension .....	89
5.5.1	Self-Starting Characteristics .....	90
5.5.2	Flowfield Properties.....	91
5.5.3	Throat Conditions .....	98
6	Summary and Conclusions .....	101
7	Future Work.....	107
7.1	Model Modifications.....	107
7.2	Future Research Topics.....	108
	Bibliography .....	111

## LIST OF FIGURES

Figure 1.1 Lockheed SR-71 <sup>9</sup> .....	7
Figure 1.2 Pratt & Whitney J-58D Engine <sup>9</sup> .....	7
Figure 1.3 SR-71 Inlet <sup>9</sup> .....	8
Figure 1.4 D-21 Drone <sup>18</sup> .....	9
Figure 1.5 D-21 Inlet <sup>9</sup> .....	10
Figure 1.6 NASA's Hypersonic Research Engine <sup>23</sup> .....	11
Figure 1.7 HRE Inlet <sup>24</sup> .....	11
Figure 1.8 Boeing XB-70 Supersonic Bomber <sup>26</sup> .....	13
Figure 1.9 XB-70 Inlet <sup>26</sup> .....	13
Figure 1.10 Concorde Supersonic Transport <sup>28</sup> .....	15
Figure 1.11 Concorde Inlet <sup>28</sup> .....	15
Figure 2.1 Illustration of Characteristic Lines .....	20
Figure 2.2 Diagram of Captured Ray Angle Geometry .....	26
Figure 2.3 Diagram of Initial Data Line Geometry .....	27
Figure 2.4 Example of Characteristics Mesh and Reflected Shock System .....	28
Figure 2.5 Diagram of Boundary Point Calculation .....	29
Figure 2.6 Diagram of Flowfield Point Calculation .....	31

Figure 2.7 Diagram of Shock Point Calculation nearest to Boundary.....	33
Figure 2.8 Diagram of Shock Point Calculation in Flowfield .....	34
Figure 2.9 Diagram of Lambda Shock and Triple Point Location .....	36
Figure 2.10 Diagram of an Isentropic Inlet Procedure .....	37
Figure 3.1 YF-12 Inlet Schematic <sup>38</sup> .....	41
Figure 3.2 Assumed Inlet Geometry.....	41
Figure 3.3 Self-Starting Characteristics of the SR-71 Inlet .....	43
Figure 3.4 Full Vehicle Mach 3.2 CFD Shockwave Patterns (top view) <sup>39</sup> .....	44
Figure 3.5 SR-71 Inlet Mach Number Contours.....	46
Figure 3.6 SR-71 Inlet Total Pressure Ratio Contours .....	47
Figure 3.7 SR-71 Inlet Temperature Ratio Contours.....	48
Figure 3.8 SR-71 Inlet Pressure Ratio Contours.....	49
Figure 3.9 SR-71 Inlet Mass Flow Ratio Contours.....	50
Figure 3.10 Supersonic SR-71 Throat Properties .....	53
Figure 3.11 Subsonic SR-71 Throat Properties .....	54
Figure 4.1 External Grid used for CFD Analysis (1/5 <sup>th</sup> the resolution).....	57
Figure 4.2 Internal Grid used for CFD Analysis (1/5 <sup>th</sup> the resolution).....	57
Figure 4.3 Mach Number Contour Comparison (CFD above) .....	58
Figure 4.4 Temperature Ratio Contour Comparison (CFD above) .....	59
Figure 4.5 Pressure Ratio Contour Comparison (CFD above) .....	60
Figure 4.6 Surface Mach Number Comparison .....	61
Figure 4.7 Surface Temperature Ratio Comparison .....	61
Figure 4.8 Surface Pressure Ratio Comparison .....	62

Figure 4.9 Viscous CFD Results.....	64
Figure 5.1 Self-Starting Characteristics of the Re-extended Spike .....	67
Figure 5.2 Re-extended Spike Inlet Mach Number Contours.....	68
Figure 5.3 Re-extended Spike Inlet Total Pressure Ratio Contours .....	69
Figure 5.4 Re-extended Spike Inlet Temperature Ratio Contours.....	70
Figure 5.5 Re-extended Spike Inlet Pressure Ratio Contours.....	71
Figure 5.6 Re-extended Spike Inlet Mass Flow Ratio Contours .....	72
Figure 5.7 Supersonic Re-extended Spike Throat Properties .....	74
Figure 5.8 Subsonic Re-extended Spike Throat Properties .....	75
Figure 5.9 Diagram of the Variable Cowl Leading Edge .....	76
Figure 5.10 Self-Starting Characteristics of the Variable Cowl Leading Edge .....	77
Figure 5.11 Diagram of the Re-extension with a Widened Shoulder .....	78
Figure 5.12 Self-Starting Characteristics of the Widened Shoulder Centerbody .....	79
Figure 5.13 Widened Shoulder Centerbody Inlet Mach Number Contours .....	80
Figure 5.14 Widened Shoulder Centerbody Inlet Total Pressure Ratio Contours .....	81
Figure 5.15 Widened Shoulder Centerbody Inlet Temperature Ratio Contours .....	82
Figure 5.16 Widened Shoulder Centerbody Inlet Pressure Ratio Contours .....	83
Figure 5.17 Widened Shoulder Centerbody Inlet Mass Flow Ratio Contours .....	84
Figure 5.18 Supersonic Widened Shoulder Centerbody Throat Properties .....	86
Figure 5.19 Subsonic Widened Shoulder Centerbody Throat Properties .....	87
Figure 5.20 Variable Cone Centerbody Diagram .....	88
Figure 5.21 Self-Starting Characteristics of the Variable Cone Centerbody .....	89
Figure 5.22 Variable Cone Centerbody with Re-extension diagram .....	90

Figure 5.23 Self-Starting Characteristics of the Variable Cone with Re-extension ...	91
Figure 5.24 Variable Cone with Re-extension Inlet Mach Number Contours .....	93
Figure 5.25 Variable Cone with Re-extension Inlet Total Pressure Ratio Contours ..	94
Figure 5.26 Variable Cone with Re-extension Inlet Temperature Ratio Contours.....	95
Figure 5.27 Variable Cone with Re-extension Inlet Pressure Ratio Contours .....	96
Figure 5.28 Variable Cone with Re-extension Inlet Mass Flow Ratio Contours .....	97
Figure 5.29 Supersonic Variable Cone with Re-extension Throat Properties .....	99
Figure 5.30 Subsonic Variable Cone with Re-extension Throat Properties .....	100
Figure 6.1 Comparison of Area-Averaged Supersonic Throat Properties .....	105
Figure 6.2 Comparison of Area-Averaged Subsonic Throat Properties .....	106

## LIST OF SYMBOLS

$A$	=	Area, ft <sup>2</sup>
$C$	=	Characteristic Line
$M$	=	Mach number
$P$	=	Pressure, lb/ft <sup>2</sup>
$R$	=	gas constant, 1716 ft-lb/ (slug-°R)
$T$	=	Temperature, °R
$V$	=	Velocity, ft/s
$\bar{V}$	=	Non-dimensional velocity
$V_l$	=	Limiting velocity
$W$	=	Ratio of velocity to limiting velocity
$a$	=	speed of sound, ft/s
$h$	=	enthalpy per unit mass, Btu/slug
$n$	=	normal component of vector
$r$	=	radial direction or component of vector
$s$	=	entropy per unit mass, Btu/ (slug-°R)
$u$	=	axial component of velocity
$v$	=	radial component of velocity

$x$	=	axial direction or component of vector
$\beta$	=	shockwave angle, degrees (or radians)
$\chi$	=	any flowfield property
$\phi$	=	potential function
$\gamma$	=	ratio of specific heats, held constant at 1.4 for air
$\mu$	=	Mach angle, $\sin^{-1}(1/M)$
$\theta$	=	flow angle; deflection angle; angle of centerline
$\rho$	=	density, slug/ft <sup>3</sup>
$\psi$	=	stream function

#### Subscripts

1	=	upstream point in the flow
2	=	at cowl station; downstream point in the flow
4	=	at throat station
+	=	first family characteristic
-	=	second family characteristic
avg	=	average quantity
max	=	maximum quantity
min	=	minimum quantity
l	=	limiting condition
o, t	=	total condition
x	=	derivative in axial direction
r	=	derivative in radial direction

$\theta$  = derivative in angular direction

$\infty, \text{inf}$  = freestream condition

# 1 Introduction

## 1.1 Motivation

The development of turbine-based combined-cycle (TBCC) engines could pave the way for future single-stage-to-orbit and/or two-stage-to-orbit reusable launch vehicles and high speed missiles. TBCC systems are designed to merge the low speed attributes of turbojets with the high speed capabilities of ramjets and scramjets. The integration of the TBCC cycle modes (gas turbine, ramjet and scramjet) into a single system poses a considerable challenge; each requires unique flow properties in order to operate properly. Of particular importance is that the inlet must provide efficient compression for all three modes across a wide Mach spectrum. Recent TBCC cycle analysis<sup>1</sup> has demonstrated that inlet performance imposes a significant constraint on the overall operation of the engine and can be, in fact, the limiting factor for maximum operational performance.

## 1.2 Inlet Design

The basic criteria for designing both supersonic and hypersonic inlets have been well documented in the literature<sup>2-4</sup>. Some key issues are as follows:

- Diffusing the required amount of air needed for engine performance with minimum total pressure loss
- Supplying the air with tolerable flow distortion
- Minimizing the amount of added external drag to the vehicle
- Minimizing both shockwave and viscous losses for good total pressure recovery
- Minimizing added mass to the vehicle
- Providing a self-starting capability at the required Mach number

Fernandez et al<sup>5</sup> discuss some of the major design issues specifically concerning combined cycle inlets and outline a roadmap for an advanced inlet program to develop the critical inlet technologies. The particular topics addressed in the paper are the transition from one cycle mode to another, boundary layer control, distortion, unstart and overall performance. Their analysis, conducted with 1D, 2D and 3D computational models, showed that the distortion, performance degradation, and total pressure recovery issues need to be corrected before any practical design is realized.

Another design issue for TBCC inlets is identifying a specific design speed. Inlets for a cruising vehicle are traditionally designed at the cruise speed since a large amount of time is spent flying at that velocity. On the other hand, an inlet for an accelerating aircraft (such as the first stage of a two-stage-to-orbit vehicle) must transition through a wide range of velocities, so choosing a single, or even multiple discrete design points for the inlet poses a tougher task. Variable geometry is likely

needed attain multiple design points.

The main issues that are dealt with in the present work are total pressure recovery, flow distortion and inlet starting. Total pressure recovery is important as it plays a key role in engine thrust and efficiency; the lower the recovery, the lower the thrust. In theory, the pressure losses can be augmented with an increase in fuel flow rate, but this leads to larger tank sizes and larger vehicle sizes (and lower specific impulse).

A flow is said to be distorted if the profiles of velocity, mass flux and thermodynamic properties vary when looking at a cross sectional piece of the flowfield. Compressors and combustors favor uniform flow properties—highly non-uniform flowfields can lead to these components performing poorly. For the purpose of this study, the distortion (or non-uniformity) is quantified as the difference between the minimum and maximum property (for example,  $\chi$ ) value divided by the area averaged value at a cross section (from Seddon and Goldsmith<sup>2</sup>), or

$$\frac{\chi_{\max} - \chi_{\min}}{\chi_{\text{avg}}} = \frac{\Delta\chi}{\chi_{\text{avg}}}. \quad (1.1)$$

The issue of inlet starting is highly critical because, as previously mentioned, inlets for TBCC engines must function properly during transition from one cycle mode to another across the entire flight regime. Hill and Peterson<sup>6</sup> provide a very good description of the starting phenomenon. In an inlet that utilizes internal supersonic compression, the flow typically passes through a converging-diverging section. For an inlet to be self-started, supersonic flow must exist at the minimum area (or throat) of the duct. In essence, the inlet remains self-started if flow

disturbances (both external and internal) do not change the captured air characteristics and the inlet is able to maintain supersonic flow at the throat. These disturbances could be a sudden rise in back pressure downstream of the throat, a gust of wind external to the inlet or boundary layer separation. Preliminary estimates of internal contraction ratios that will self-start can be obtained by calculating the Kantrowitz limit<sup>7</sup>. This limit is determined by first assuming a normal shockwave at the beginning of the internal compression section. The internal area ratio that produces sonic flow at the throat is then found by assuming one-dimensional, isentropic flow through the duct. For a perfect gas, the limit can be calculated as follows:

$$\left(\frac{A_2}{A_4}\right) = \frac{1}{M_2} \left(\frac{(\gamma+1)M_2^2}{(\gamma-1)M_2^2+2}\right)^{\frac{\gamma}{\gamma-1}} \cdot \left(\frac{\gamma+1}{2\gamma M_2^2 - (\gamma-1)}\right)^{\frac{1}{\gamma-1}} \cdot \left(\frac{1 + \frac{\gamma-1}{2}M_2^2}{\frac{\gamma+1}{2}}\right)^{\frac{\gamma+1}{2(\gamma-1)}} \quad (1.2)$$

Note the  $M_2$  in the Equation 2 is the mass-averaged Mach number across the cowl face. The maximum isentropic contraction ratio can be calculated as follows:

$$\left(\frac{A_4}{A_\infty}\right) = M_\infty \left(\frac{\gamma+1}{2}\right)^{\frac{\gamma+1}{2(\gamma-1)}} \cdot \left(1 + \frac{\gamma-1}{2}M_\infty^2\right)^{-\frac{\gamma+1}{2(\gamma-1)}} \quad (1.3)$$

Van Wie<sup>8</sup> discusses experimental data found from a wide variety of inlets and compares their starting characteristics to that predicted by the Kantrowitz limit. This work shows that the Kantrowitz limit can be, under some circumstances, exceeded with bleed holes and/or bypasses. However, for the purposes of this research, the Kantrowitz limit is held as a design constraint.

### 1.2.1 Previous Work

To this date, flight-ready hardware for a turbine-based combined-cycle engine has yet to be developed. Likewise, the inlet for such an engine has not been designed either. However, supersonic airplanes and missiles have been flying for decades. While the engines operating on aircraft may not be (or even similar to) combined cycles, their inlet characteristics are very analogous to that needed on a TBCC inlet. The following sections will discuss a sample of supersonic aircraft, along with their engines and inlets, to gain insight into the design strategies of existing supersonic inlets. It should be noted that some of the vehicles reported on were (or are still) considered sensitive so the available technical information, in some cases, is rather scarce. For the most part, this work has relied upon open-literature NASA reports.

#### 1.2.1.1 Lockheed SR-71

The Lockheed SR-71 (Figure 1.1) is still the world's fastest manned air-breathing aircraft. The airplane was designed to serve as a long range reconnaissance vehicle and could fly at speeds upwards of Mach 3.2 with a ceiling of about 85,000 ft<sup>9</sup>. The SR-71 was powered by two Pratt & Whitney J-58D engines (Figure 1.2). Each engine was an axial flow turbojet using a nine stage compressor, two stage turbine with bypass and produced 34,000 lbs of thrust with the afterburner. It was the first jet engine designed to operate over long periods of time using its afterburner. At high Mach numbers, the turbo-machinery was heavily bypassed thereby creating a quasi-ramjet mode. In this way, the J-58D was an early combined-cycle. Interestingly, a study<sup>10,11</sup> was completed in the mid-90's looking at the SR-71 as the

first stage of a small payload launch vehicle.

The SR-71 engine inlet (Figure 1.3) operated as a mixed internal/external compression system. Ben Rich, program manager for the propulsion system of the SR-71, called the design of the inlets the “single most complex and vexing engineering problem of the entire project<sup>12</sup>.” He also went on to add that “developing this [system] was the most exhausting, difficult, and nerve-racking work of my professional life.” An intensive review of the inlet operation is given in the *SR-71 Flight Manual*<sup>13</sup>. The external system utilized a translating conical spike that retracted  $1 \frac{5}{8}$  inches per 0.1 Mach number starting near Mach 1.6 and ending at Mach 3.2 with shock-on-lip condition. The internal system consisted of a series of reflected shock waves followed by a terminal shock that is created by a step, effectively tripping the flow; the inlet self-starts when the spike begins to translate. Originally controlled by the pilot, the inlet system was outfitted with a Digital Automated Flight and Inlet Control System (DAFICS)<sup>14</sup> in the early 1980’s to allow for faster response to unstart.

The purpose of the translation, along with a complex sequence of bleeds<sup>15-17</sup> and bypasses, is to control the amount of flow entering the engine and to hold the terminal shock downstream of the throat (when  $M_\infty > 1.6$ ) to avoid unstart. At low Mach numbers, the forward air inlet bypass doors open to exhaust air that is not needed by the engine. As the spike translates, the forward bypass doors begin to close in order to position the shock downstream of the throat. Shock trap and centerbody bleeds, along with aft bypass doors, also aid in the process of keeping the terminal shock in the correct position and to mitigate the effects of

shockwave/boundary layer interactions. The spike translation increases the captured stream tube area from 8.7 ft<sup>2</sup> to 18.5 ft<sup>2</sup>. In the event of unstart of one of the engines, the DAFICS would push both engine spikes forward and control the bleeds and bypasses such that normal operation and normal shock position could be reobtained within seconds.



Figure 1.1 Lockheed SR-71<sup>9</sup>

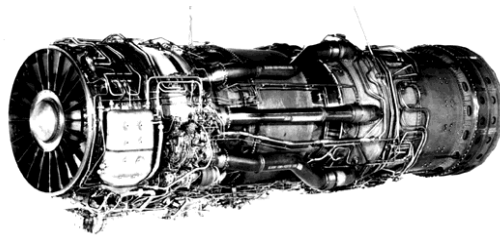


Figure 1.2 Pratt & Whitney J-58D Engine<sup>9</sup>

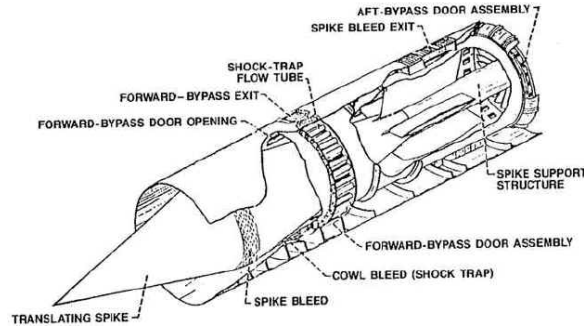


Figure 1.3 SR-71 Inlet<sup>9</sup>

### 1.2.1.2 Lockheed D-21 Drone

One of the most secret aircraft ever developed, the D-21 Drone was an unmanned, expendable reconnaissance vehicle that flew in excess of Mach 3.5 above 90,000 ft.<sup>9</sup> Shown in Figure 1.4, The 42 ft. long vehicle was originally launched from an M-21 (a cousin of the SR-71); however, after a fatal crash during separation, the drone was fixed with a carrier rocket and launched from a modified B-52 instead. The spy vehicle was designed to eject the reconnaissance data prior to crashing. The drone was outfitted with a Marquardt XRJ-43-MA20S-4 ramjet capable of run times upwards of 2 hours<sup>12</sup>.

The D-21 inlet is shown in Figure 1.5. Due to the intense secrecy of the program, there are no open-literature sources detailing the exact performance and geometry of the D-21 inlet. However, the inlet used on the Bomarc B Missile Interceptor used a similar ramjet (XRJ-43-MA20) and its inlet was a fixed geometry, Mach 2.35 axisymmetric isentropic inlet<sup>19</sup>. In all likelihood, since the D-21 was able to fly past Mach 3.5, its design Mach number was not Mach 2.35. However, the inlet

does appear to have an isentropic spike. The original spike was probably fixed, as well, since the flight envelope of the D-21 was not very wide. Interestingly, in 1999 NASA and Lockheed Martin prepared a study<sup>20</sup> to determine the feasibility of outfitting the D-21 with a Rocket Based Combined Cycle (RBCC) engine. The program was called DRACO (Demonstration of Rocket and Air-breathing Combined-cycle Operation). The modification to the inlet system required the replacement of the original fixed geometry axisymmetric inlet with a translating axisymmetric inlet capable of operation into the Mach 5-6 range<sup>21</sup>.

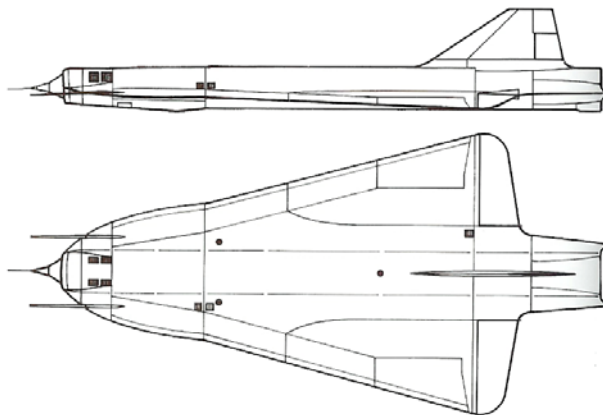


Figure 1.4 D-21 Drone<sup>18</sup>



Figure 1.5 D-21 Inlet<sup>9</sup>

### 1.2.1.3 NASA's Hypersonic Research Engine

In the 1960's, NASA undertook an effort to design, develop, and construct a hypersonic research ramjet/scramjet and to flight test the concept from Mach numbers 3 through 8—this project was known as the Hypersonic Research Engine (HRE)<sup>22</sup>. Shown in Figure 1.6, the HRE was intended to be the first project to integrate years of research in high speed inlets and nozzles, and the first to use a direct-connect scramjet combustor. Numerous ground tests were conducted at Mach number of 5, 6 and 7; however, because of the cancellation of the X-15 program, no flight tests were ever performed.

A schematic of the inlet used on the HRE is show in Figure 1.7. It was a mixed compression system that utilized an axisymmetric translating spike. The spike consisted of a 10° initial half angled cone that isentropically turned the flow up to a 22° surface angle. The spike was fixed from Mach 4 to 6 with the spike tip shock falling outside of the cowl lip. Starting at Mach 6, the spike tip shock impinged on the cowl leading edge—this condition was maintained through Mach 8 by pushing the centerbody forward to maintain the shock on lip criteria. The engine was operated in

a ramjet mode (i.e. subsonic combustion) from Mach 4 to 6. However, starting between Mach 5 and 6, the engine transitioned from ramjet to scramjet mode. The engine was regeneratively cooled using the hydrogen fuel.



Figure 1.6 NASA's Hypersonic Research Engine<sup>23</sup>

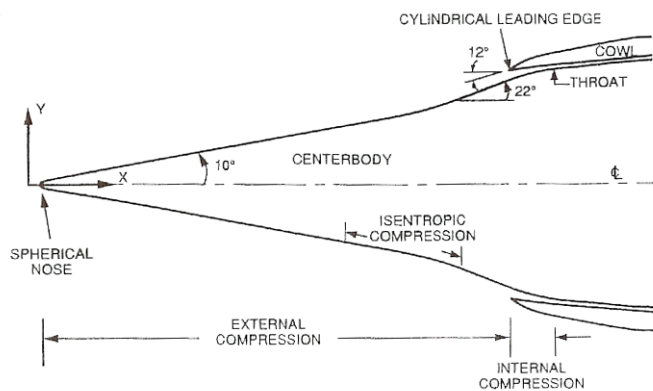


Figure 1.7 HRE Inlet<sup>24</sup>

#### 1.2.1.4 Boeing XB-70

The XB-70 was designed and built to be a long-range, supersonic cruise, bomber with a gross weight of about 500,000 pounds and a cruising speed of Mach 3<sup>25</sup>. The schematic in Figure 1.8 shows the design features. The design highlighted a 65.6° swept back leading edge delta wing with folding wing tips (creating a quasi-

waverider design). The vehicle propulsion system resided underneath the aircraft and consisted of two, two-dimensional inlets mounted side-by-side. Each inlet fed three YJ93-GE-3 afterburning turbojet engines that generated 30,000 pounds of thrust. Each engine consisted of an 11-stage, axial flow compressor, an annular combustor, a two-stage turbine and a variable area, converging-diverging nozzle.

The inlet<sup>26</sup> was designed as a mixed-compression system as shown in Figure 1.9. The inlet started at Mach 2.0 (i.e. the terminal shock laid across the inlet cowl face). Each inlet was composed of variable ramps and bypass doors that could be positioned to maximize performance through the flight profile. The boundary layer was controlled through a porous wall bleed system in the throat region. Each intake had six bypass doors installed just forward of the engine face that, used in conjunction with the variable throat, would position the normal shock and match engine airflow requirements. Control of the inlet system was both manual and semiautomatic in the first prototype XB-70; however, the second was fully automatic. The purpose of the variable throat and bypass system, as with the SR-71, was to position the terminal normal shock slightly downstream of the aerodynamic throat to promote stable operation and to maintain self-starting.

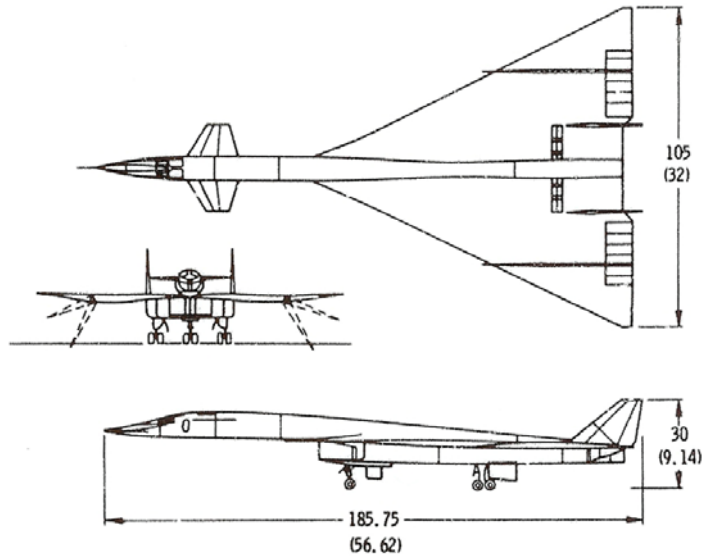


Figure 1.8 Boeing XB-70 Supersonic Bomber<sup>26</sup>

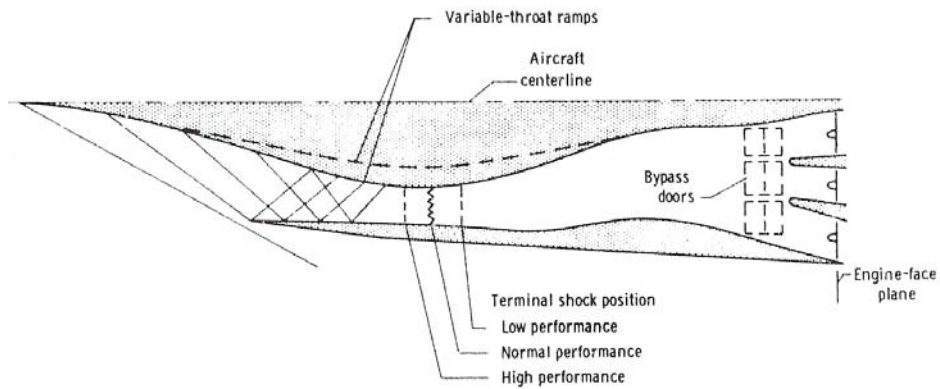


Figure 1.9 XB-70 Inlet<sup>26</sup>

#### 1.2.1.5 Concorde

For over 25 years, up until 2003, the Concorde (Figure 1.10) was the only operational civil supersonic transport. It was designed for a maximum cruise speed of Mach 2.2<sup>27</sup>. The major design features of the vehicle area modified delta wing, no variable-geometry high-lift devices, four engines mounted underneath the wing, variable geometry two-dimensional inlets and a variable geometry exhaust nozzle.

Each engine (OL 593) was capable of generating over 38,000 pounds of thrust at takeoff. The engines consisted of a seven-stage low-pressure and seven-stage high pressure compressor, an annular combustor, a single-stage high pressure turbine and a single-stage low pressure turbine, both with cooled stator and rotor blades. An afterburner was also used to provide adequate thrust at takeoff and for transonic acceleration.

The schematic of the four inlets is shown in Figure 1.11. Each two-dimensional inlet consists of an initial, fixed ramp, followed by a second hinged ramp that utilizes isentropic compression<sup>28</sup>. A terminal, strong oblique shock emanates off of the cowl lip. Below Mach 1.3, both ramps are fully open and the bleed door is closed. Above Mach 1.3, the ramps and dump door are moved per the engine requirements. The boundary layer diverter and ramp bleed slot are employed to reduce the negative effects of boundary layer growth. The design combines a high measure of internal recovery and flow quality with low external drag. Control of the variable ramps and doors relies on analog and digital computers.

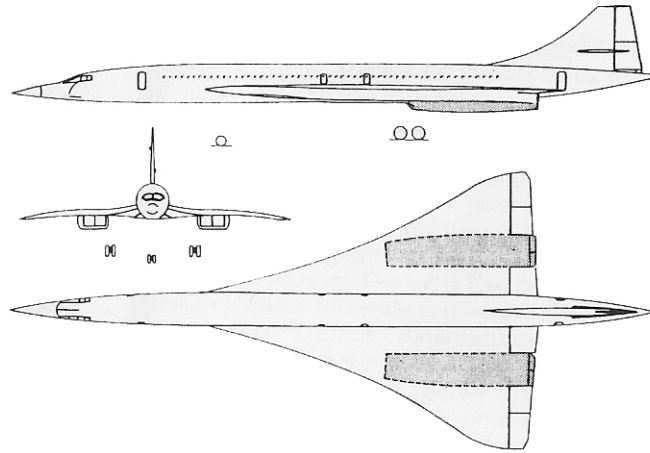


Figure 1.10 Concorde Supersonic Transport<sup>28</sup>

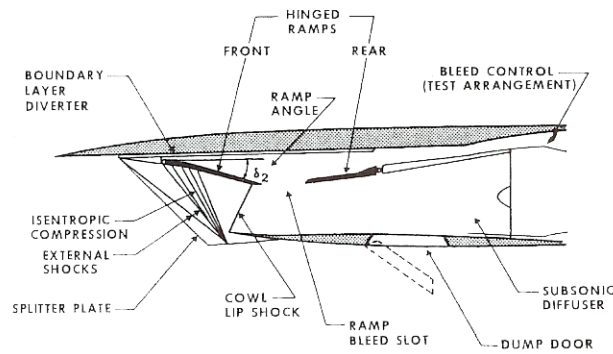


Figure 1.11 Concorde Inlet<sup>28</sup>

#### 1.2.1.6 Inlet Comparisons

The preceding five sections detailed the inlet design and operation for five distinct supersonic systems. The designs showed that both two-dimensional (XB-70 and Concorde) and axisymmetric (SR-71, D-21 and HRE) schemes are viable options for the design of a supersonic inlet. With the exception of the original D-21 inlet, every design shown incorporated some sort of variable geometry, be it a translating

spike, hinged doors or a variable throat. Variable geometry was needed, of course, because the range of flight speeds for the vehicle (or engine) required operation under a variety of conditions. The variable geometry was used to improve aerodynamic performance, match engine airflow requirements, and to maintain inlet starting.

### 1.3 Objective

The objective of this research project is to investigate novel inlets to be used in conjunction with TBCC engines. Instead of designing an inlet from scratch, the approach will be to build on the knowledge of existing supersonic inlets used on previous TBCC-like engines. The process will examine the effects of overspeeding a known inlet, and then incorporate design changes from lessons learned in an attempt to increase its operational range into the hypersonic flight regime. To this end, the limit of previous high-speed inlet designs will be explored, to both determine their maximum speeds and identify means of extending their operational velocities.

For this present work, the benchmark for a TBCC-like engine was chosen to be the Pratt & Whitney J-58D used on the Lockheed SR-71 Blackbird previously discussed in Section 1.2.1.1. As stated above, the inlet will be analyzed for its traditional use to fully understand its normal operational characteristics and will then be oversped, employing design changes in order to improve its high speed capabilities and to conceptualize the design needs for future TBCC inlets. Obviously, the J-58D could not work much past its intended design speed; however, for the purposes of this thought experiment, the modified inlet(s) will be decoupled from the engine and studied by itself. A method of characteristics (MOC) solution will be used to analyze

the inlet. The advantage this type of analysis has over higher order computational methods, such as computational fluid dynamics (CFD), is that MOC solutions are much faster and the results are more readily available. However, CFD will be used to validate the characteristics model developed for this project and to preview the effects of viscosity on the system. Additionally, the effects of drag and added installation mass are not considered in this report.

This work makes the following contributions:

- An axisymmetric method of characteristics computer program has been developed to study supersonic inlets. The program calculates both the external and internal supersonic flowfield, including the reflected shock system within a duct. The functions developed within the program are wholly interchangeable, say for use with a two-dimensional flowfield.
- A detailed study of the inviscid properties of the SR-71-type inlet is performed. The inlet geometry was reverse engineered from NASA YF-12 reports. Mach number, total pressure, temperature, pressure and mass flow properties are found for flight speeds of Mach 1.7 to 3.2. Final flow properties through a prescribed lambda-shock system are also shown. The self-starting characteristics of the inlet are also calculated.
- Various methods to modify the SR-71-type inlet are surmised with the purpose of extending the inlet's operation into the hypersonic flight regime. Each of these methods is evaluated based upon their self-starting characteristics and the flowfield properties of each design. Both the

supersonic and subsonic conditions are resolved at the exit plane.

- This work represents a starting point in the design process of turbine-based combined-cycle engine inlets and provides a means to conceptualize the requirements for the development of future systems. No optimization of any design is performed.

## 2 Model Development

### 2.1 Program Description

All of the inlets considered in this report consisted of a centerbody spike acting as the lower surface and a cowl acting as the upper boundary. A method of characteristics algorithm was written in C to perform full external and internal supersonic flow analysis on axisymmetric combined cycle inlets. The program begins by calculating the supersonic flow over a cone, with the condition that the external tip shockwave lay outside of or on the cowl leading edge. From that point on, the remainder of the flow is analyzed by calculating the reflected internal shockwaves until the point where a normal shockwave was prescribed – the downstream regions of subsonic flow will not be considered here. The ratio of specific heats ( $\gamma$ ) was held constant throughout the procedure and level, steady flight was assumed at zero angle of attack. All cases were run on a Dell Latitude D600 with a 1.6 GHz Pentium M processor and 1 GB of RAM. The initial data line always begins with 402 points—typical run times were on the order of 15-20 seconds.

## 2.2 Method of Characteristics

Because of the importance to this work, the method of characteristics will be reviewed. The equations governing steady, inviscid, supersonic flow are hyperbolic by nature. A solution to these equations can be found by employing the method of characteristics<sup>29</sup> which reduces the governing hyperbolic partial differential equations into compatibility relations. The compatibility equations are an algebraic system of equations for irrotational, two-dimensional flow or a system of ordinary differential equations for axially symmetric flow. The characteristic lines for two-dimensional or axially symmetric flow are Mach lines as shown in Figure 2.1. Solutions can be found only along these lines, i.e. information can only propagate downstream in supersonic flow. For the present work, solutions to the equations governing supersonic, axially symmetric flow will be used. The equations, as shown by Ferri<sup>30</sup>, are briefly introduced below. The following sections are meant only as a brief introduction to characteristics methods. A more detailed description can be found in Ref.'s 29 and 30.

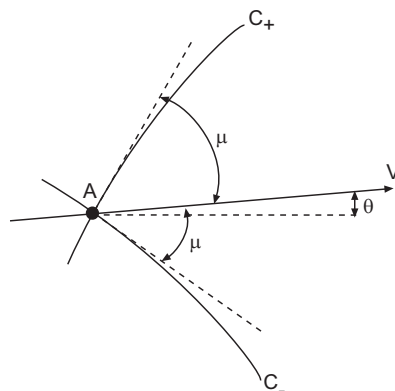


Figure 2.1 Illustration of Characteristic Lines

### 2.2.1 Supersonic Potential Flow with Axial Symmetry

In a velocity field, if the curl of the velocity is equal to zero at every point within the flow, the flow is called irrotational. This implies that each fluid element has no angular velocity. This type of flow is also called potential flow. The velocity potential applies to one, two and three-dimensional irrotational flows only. The partial differential equation governing supersonic potential flow with axial symmetry is

$$\left(1 - \frac{\phi_x^2}{a^2}\right) \frac{\partial^2 \phi}{\partial x^2} + \left(1 - \frac{\phi_r^2}{a^2}\right) \frac{\partial^2 \phi}{\partial r^2} - \frac{2\phi_x \phi_r}{a^2} \frac{\partial^2 \phi}{\partial r \partial x} + \frac{v}{r} = 0 \quad (2.1)$$

The + (plus) characteristic (also known as the first family) is defined by

$$\frac{dr}{dx} = \tan(\theta + \mu) \quad (2.2)$$

and the – (minus) characteristic (also known as the second family) is defined by

$$\frac{dr}{dx} = \tan(\theta - \mu). \quad (2.3)$$

By defining  $W$  as the ratio of velocity to limiting velocity (the velocity corresponding to expansion into vacuum)

$$\left(\frac{V_l}{V}\right)^2 = \frac{1}{W^2} = 1 + \frac{2}{\gamma - 1} \sin^2(\mu) \quad (2.4)$$

the following compatibility relations are found

$$\frac{dW}{W} - d\theta \tan(\mu) - \frac{dx}{r} \frac{\sin(\mu) \sin(\theta) \tan(\mu)}{\cos(\theta + \mu)} = 0 \quad (2.5)$$

along the  $C_+$  characteristic and along the  $C_-$  characteristic

$$\frac{dW}{W} + d\theta \tan(\mu) - \frac{dx}{r} \frac{\sin(\mu) \sin(\theta) \tan(\mu)}{\cos(\theta - \mu)} = 0. \quad (2.6)$$

Equations (2.5) and (2.6) can be numerically solved using first order differences for the derivatives.

## 2.2.2 Supersonic Rotational Flow with Axial Symmetry

The flow downstream of a conical shockwave is non-uniform. When this non-uniform flow is turned into itself, the resulting shockwave is curved. When a shockwave is curved, an entropy gradient is developed, and the flow downstream of the shock is no longer isentropic. Therefore, the flow must be considered rotational. Stream functions can be defined for two-dimensional (and axisymmetric) rotational or irrotational flows. If the flow is described by a stream function, instead of a potential equation, the following set of equations apply:

$$\begin{aligned} \psi_r &= ru(1 - W^2)^{\frac{1}{\gamma-1}} \\ \psi_x &= -rv(1 - W^2)^{\frac{1}{\gamma-1}} \end{aligned} \quad (2.7)$$

and

$$f(\psi) = -\frac{v_x - u_r}{r(1 - W^2)^{\frac{\gamma}{\gamma-1}}}. \quad (2.8)$$

The following equation can be obtained from the equations of state, continuity and energy (assuming steady flow)

$$\left(1 - \frac{u^2 V_l^2}{a^2}\right) \psi_{xx} - \frac{2uvV_l^2}{a^2} \psi_{xr} + \left(1 - \frac{v^2 V_l^2}{a^2}\right) \psi_{rr} - \frac{\psi_r}{r} - r^2 (1 - W^2)^{\frac{\gamma+1}{\gamma-1}} \left(\frac{W^2 V_l^2}{a^2} - 1\right) f(\psi) = 0 \quad (2.9)$$

After a considerable derivation, the characteristic lines become the same as Eqns. (2.2) and (2.3) for the  $C_+$  and  $C_-$  characteristics, respectively, and the compatibility equations become

$$\frac{dW}{W} - \tan(\mu)d\theta - \frac{dx}{r} \frac{\sin(\mu)\sin(\theta)\tan(\mu)}{\cos(\theta + \mu)} + \frac{dx}{\gamma R} \frac{ds}{dn} \frac{\sin^3(\mu)}{\cos(\theta + \mu)} = 0 \quad (2.10)$$

along the  $C_+$  characteristic and along the  $C_-$  characteristic,

$$\frac{dW}{W} + \tan(\mu)d\theta - \frac{dx}{r} \frac{\sin(\mu)\sin(\theta)\tan(\mu)}{\cos(\theta - \mu)} - \frac{dx}{\gamma R} \frac{ds}{dn} \frac{\sin^3(\mu)}{\cos(\theta - \mu)} = 0. \quad (2.11)$$

Again, just as with the potential flow equations, Eqns. (2.10) and (2.11) are solved using first order differences for the derivatives. However, the entropy derivative must be handled in a particular manner and is outlined in Ref. 30. Comparing Eq.'s 2.5 and 2.10 along with Eq.'s 2.6 and 2.11, the rotational flow equations are the potential flow equations with an entropy correction term. This is expected since (for two-dimensional or axisymmetric flows) the stream function applies to irrotational flows as well (i.e. the  $ds/dn$  term is equal to zero).

### 2.3 Solution Procedure

The following is a brief overview of the procedure used to calculate the flowfield within the inlet including flowfield points, boundary points and shockwave points.

### 2.3.1 Initial Data Line

In order to implement the method of characteristics, an initial line of data (an initial characteristic line in which all the flow properties are known) must be found. For all of the cases analyzed in this report, the initial data line was found by solving for the flow over a cone. The solution to supersonic flow over a cone for any given freestream Mach number and cone angle is given by the Taylor-Maccoll equation<sup>31</sup>

$$\frac{\gamma-1}{2} \left[ V_{\max}^2 - V_r^2 - V_\theta^2 \right] \left[ 2V_r + V_\theta \cot(\theta) + \frac{dV_\theta}{d\theta} \right] - V_\theta \left[ V_r V_\theta + \frac{dV_r}{d\theta} \frac{dV_\theta}{d\theta} \right] = 0 \quad (2.12)$$

where  $V_r$  is the radial component of the velocity,  $\theta$  is the angle from the centerline of the cone to the ray of the solution, and  $V_{\max}$  is the maximum theoretical velocity when the flow has been expanded to zero temperature given by

$$V_{\max} = \sqrt{2h_o} \quad (2.13)$$

where  $h_o$  is the freestream total enthalpy. The normal component of the velocity can be found by

$$V_\theta = V_r' = \frac{dV_r}{d\theta}. \quad (2.14)$$

By defining a nondimensional velocity  $\bar{V}$  as

$$\bar{V} = \frac{V}{V_{\max}} \quad (2.15)$$

the Taylor-Maccoll equation can be re-written as

$$\frac{\gamma-1}{2} \left[ 1 - \bar{V}_r^2 - \left( \frac{d\bar{V}_r}{d\theta} \right)^2 \right] \left[ 2\bar{V}_r + \frac{d\bar{V}_r}{d\theta} \cot(\theta) + \frac{d^2\bar{V}_r}{d\theta^2} \right] - \frac{d\bar{V}_r}{d\theta} \left[ \bar{V}_r \frac{d\bar{V}_r}{d\theta} + \frac{d\bar{V}_r}{d\theta} \left( \frac{d^2\bar{V}_r}{d\theta^2} \right) \right] = 0 \quad (2.16)$$

Equation (2.16) can be rearranged and solved for the second derivative of the normalized radial velocity, yielding an ordinary differential equation in terms of the ray angle, the normalized radial velocity and the first derivative of the normalized radial velocity. The equation can be integrated numerically, for instance using the fourth-order Runge-Kutta method<sup>32</sup>. Using the shooting method outlined in Anderson<sup>33</sup>, the freestream Mach number and cone angle are prescribed and the resulting shockwave angle can be found.

Now that the shockwave angle is known, the initial data line can be calculated. From the Taylor-Maccoll equation, the flow properties (Mach number and flow angle) can be found as a function of ray angle. To start the solution, these flow properties need to be transformed into physical (x, r) coordinates, i.e. the creation of an initial data line. Conical flow is non-uniform, meaning the flow angle relative to the axis decreases (and Mach number increases) from the surface to the shock. Therefore, the initial characteristic line is curved. The angle from the tip of the centerbody to the leading edge of the cowl is known as the capture angle as shown in Figure 2.2. This angle is always less than or equal to (in the case of shock on lip) the shockwave angle.

To start the process, the Taylor-Maccoll equation is integrated in very small ray angle increments from the shockwave until the cowl. Two methods to generate

the initial data line from the cowl have been investigated. The first is the simplest but has some drawbacks. Using the geometry as shown in Figure 2.3, the initial data line is generated by marching in equal ray angle increments from the cowl (the first point  $i$ ) and intersecting the  $C_+$  characteristic with the ray angle at the next point ( $i+1$ ). The angle of the  $C_+$  characteristic line is the average of the flow angles plus the average of the Mach angles of the  $i$  and  $i+1$  points. The process is repeated until the centerbody surface is reached. The drawback of using this method is that the mesh tends to be highly concentrated towards the surface, creating an unequally spaced mesh—this can tend to incur errors when marching downstream using the method of characteristics. Instead of marching in equal ray angle increments, the second method divides the initial characteristic into equal changes in  $x$  and solves for the subsequent changes in ray angle at each point—again, the process marches from the cowl to the centerbody. This produces an initial characteristic that is equally spaced in the  $x$ -direction from the cowl lip to the centerbody intersection.

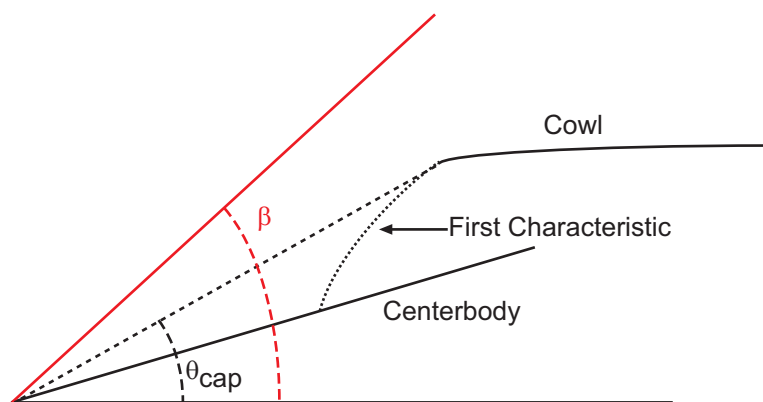


Figure 2.2 Diagram of Captured Ray Angle Geometry

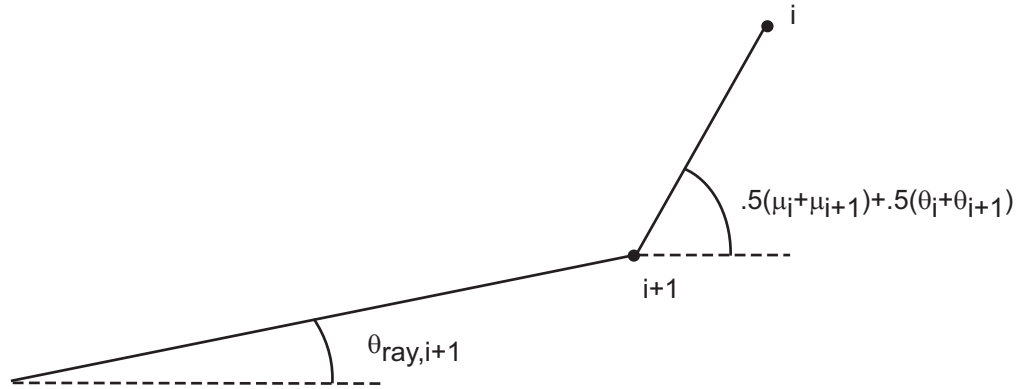


Figure 2.3 Diagram of Initial Data Line Geometry

### 2.3.2 Flowfield Calculations

From the initial data line, the solution proceeds to calculate the next characteristic line and the internal reflected shock system, an example of which is shown in Figure 2.4. As the characteristics net is formed, the shock waves are propagated through the system. In the first zone, the area between the initial data line and the first reflected cowl shock, the flow is isentropic so the potential flow compatibility relations are used. In the remaining zones, since all of the reflected shockwaves will be curved, the rotational flow compatibility relations are used [In reality, the compatibility relations found from the stream function can be used for the entire flowfield]. The remaining subsections discuss how each point in the flow is handled.

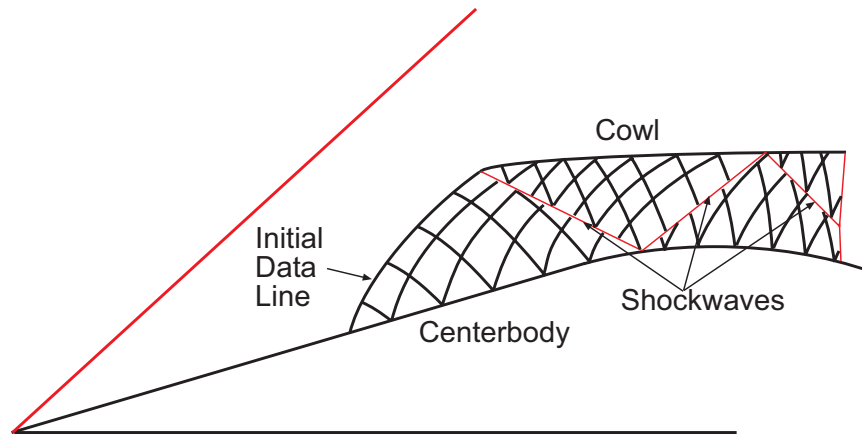


Figure 2.4 Example of Characteristics Mesh and Reflected Shock System

### 2.3.2.1 Boundary Point Calculation

The procedure to calculate the next downstream boundary point is shown in Figure 2.5. The nearest point to the boundary on the working characteristic (the  $C_+$  characteristic in the figure) is used to find the next boundary point. The  $C_-$  characteristic from point 1 is intersected with the boundary (at point 2') as shown by the dashed line. At this new location, the flow angle is set equal to the angle of the surface (since all streamlines must be parallel to the surface) and the correct compatibility equation is solved at this point for the remaining variables (Mach number, entropy, Mach angle, etc.)—if the flow is irrotational (i.e. in the region upstream of the first reflected shock), Eqn. (2.6) is used; otherwise, if the flow is rotational (i.e. downstream of the first reflected shockwave), Eqn. (2.11) is used. Note that if the working characteristic is the  $C_-$  curve, then the  $C_+$  characteristic is intersected with the boundary and the respective compatibility equation is solved. However, point 2' is not the “exact” location of the intersection since it is approximating the characteristic curve with a straight line. A correction can be made

in which the C. characteristic line slope from point 1 is set to the average of the flow angles and Mach angles at both points 1 and 2' and the new flow properties and the new point 2' are found. This process is repeated until the location of point 2' does not change (within a margin of error of 0.00001) at successive iterations. However, for the majority of cases, the solution is held to 1 or 2 iterations because in some instances the solution tended to diverge. The equations used to calculate the thermodynamic properties at each point are discussed in Section 2.4.

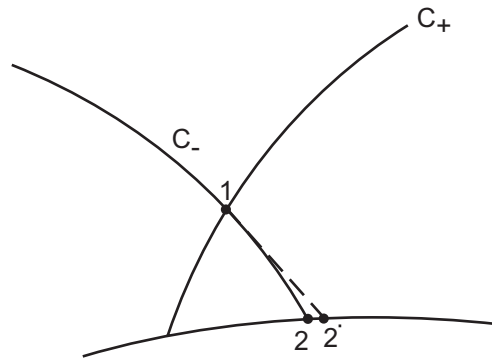


Figure 2.5 Diagram of Boundary Point Calculation

### 2.3.2.2 Flowfield Point Calculation

The procedure to calculate the downstream flowfield points is shown in Figure 2.6. The  $C_+$  characteristic from point 2 (which could be the first boundary point or another flowfield point) is intersected with the C. characteristic from point 1 which is located on the previous data line. Point 3' is the intersection of these lines. At this point, no flow properties are yet known. A coupled solution of Eqns. (2.5) and (2.6) (for potential flow) or Eqns. (2.10) and (2.11) (for rotational flow) is found. From the solution, the flow properties (flow angle, Mach number, entropy, etc.) at

point 3' are found. Again, using the updated properties at point 3', a correction is found setting the slopes of the characteristic lines to be the average of the upstream and downstream Mach lines. The process is iterated until the location of point 3' does not change within a margin of error at successive iterations. As mentioned earlier, the solution is generally held to 1 or 2 iterations to avoid any potential divergence problems. This procedure is repeated throughout the remainder of the flowfield along the working characteristic until point 1 is the final point on the previous data line. One of the drawbacks of the method of characteristics, is that at each successive step, the new data line is one point shorter in length; however, with a sufficiently fine starting grid, the resulting decrease in numerical accuracy because of the lost data point is not an issue. The process is simply reversed when the working characteristic is the C. curve. Again, the thermodynamics relations are discussed in a future section.

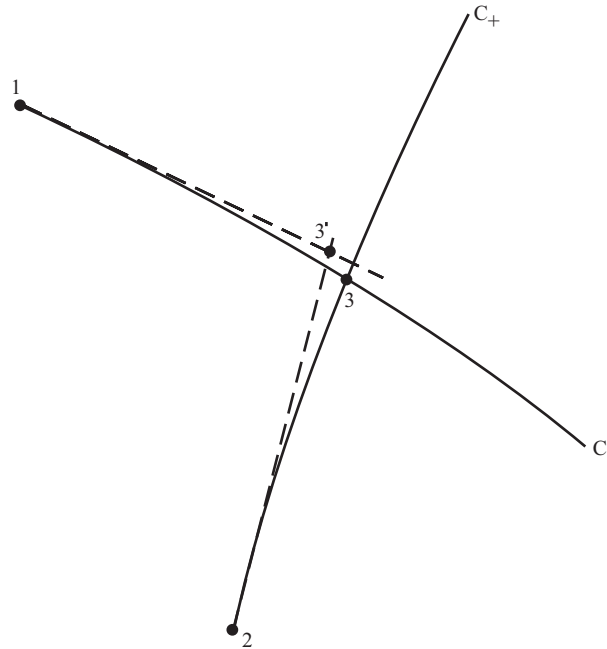


Figure 2.6 Diagram of Flowfield Point Calculation

### 2.3.3 Shock Point Calculations

A shockwave forms when supersonic flow is turned into itself. Likewise, a shock also is generated when two characteristic lines of the same family cross each other. In the present model, the shockwaves are fit to the system, i.e. the shock is treated as a discontinuity in the flowfield. The following sections discuss how the shocks are propagated through the flowfield in the present work. All of the internal shock segments are assumed to be two-dimensional, planar shockwaves.

#### 2.3.3.1 Shock Point Calculation near Boundary

The location of the first reflected cowl shock is always known a priori. It is the leading edge of the cowl. At the leading edge, the upstream flow properties, as well as the angle of the cowl surface, are known values. Since the flow downstream

of the shock must be parallel to the surface, the shock deflection angle is set equal to the difference between the upstream flow angle and surface angle. The shockwave angle is determined by solving the  $\theta$ - $\beta$ - $M$  equation which is presented, along with the shockwave thermodynamic properties, in Section 2.4. With the origin of the shockwave known, it can be propagated through the flowfield.

The procedure to calculate the second shock point (the point nearest to the boundary) is shown in Figure 2.7. The shockwave segment from the origin is intersected with the next characteristic line (in the case of the figure, the next  $C_-$  characteristic). This is shown by point 1 in the figure. The properties at point 1 upstream of the shock are found by a linear interpolation of the data at the two points before and after point 1. The deflection angle is assumed to be the same as the at the previous shock point. The properties behind the shock are calculated using the oblique shock relations. Next, using the new downstream shock properties, points 2 and 3 in the figure are found by sending the  $C_+$  and  $C_-$  characteristics, respectively, to intersect the surface and solving each respective compatibility relation to find the flow properties at both points. The characteristics at points 2 and 3 are then sent back and intersected to find updated downstream properties at point 1. The new flow angle is then used to calculate a new deflection angle at point 1. The process of calculating the shock properties and finding points 2 and 3 is repeated using the new deflection angle. This procedure is iterated until the downstream flow angle and flow angle found from the intersection of the characteristics from points 2 and 3 agree. For further correction, the location of point 1 is then updated by averaging the slope of the shock at the origin and the new shock angle at point 1. The entire process is repeated

until the location of point 1 and the properties of point 1 do not change (within a margin of error) between successive iterations. Point 3 is saved because it is the starting point of the next downstream  $C_+$  characteristic and is used to calculate the next shock point in the flow (as is discussed in the next section). The procedure is simply mirrored if the shock reflection is off of the upper surface instead of the lower surface as shown in the figure.

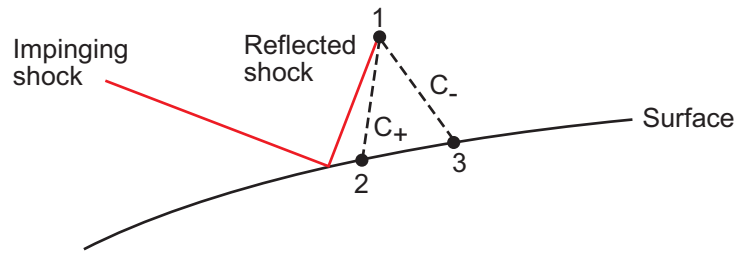


Figure 2.7 Diagram of Shock Point Calculation nearest to Boundary

### 2.3.3.2 Shock Point Calculation in Flowfield

The procedure to calculate the shock points within the flowfield is very similar to that of the previous section and is shown in Figure 2.8. Points 0 (the previous shock point) and 2 (the previous downstream flowfield point) can be thought of as points 1 and 3, respectively, in the previous figure. Point 1 is found by intersecting the shock with the next working characteristic line. Again, the deflection angle is assumed to be the same as that of the previous shock point. The properties behind the shockwave are found using the shock relations. Point 3 is found by intersecting the  $C_-$  characteristic with the  $C_+$  characteristic from point 2 and solving the coupled compatibility relations to find the flow properties at point 3. Point 2' is found by intersecting the  $C_+$  characteristic from point 1 with the  $C_-$  characteristic that

runs from point 0 to point 2. The properties at point 2' are found by a linear interpolation of the data at points 0 and 2. Then, as in the previous section, the characteristics from point 3 and 2' are sent back to point 1 and a new flow angle at point 1 downstream of the shock is found. Again, the entire process is repeated until the flow properties and location of point 1 do not change with successive iterations.

This process is repeated until the shock propagates to the other boundary, in which case the location of point 1 is found by intersecting point 0 with the surface. However, because the shockwave is curved, the downstream characteristic line (points 2 and 3 in the below figure) will inevitably reflect off of the shock boundary. In the event that point 3 crosses the shock boundary, the method of characteristics (as described in Section 2.3.2) is performed on the downstream characteristic line to form a new characteristic line. The procedure to find points 1 and 3 is then repeated. The more curved the shock, the more times a new downstream characteristic line will need to be found. Once the shock is transmitted through the flowfield to the other boundary, the downstream characteristic line that was found when calculating the shock propagation becomes the new working characteristic line that is used to determine the location of properties of the next reflected shockwave.

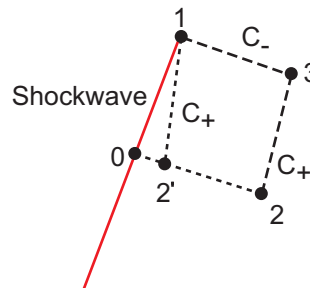


Figure 2.8 Diagram of Shock Point Calculation in Flowfield

### 2.3.3.3 Lambda Shock and Triple Point Calculation

The entire procedure of calculating the reflected shockwaves is repeated until (in the case of this report) the flow is tripped by a normal shockwave as is shown in Figure 2.9. At point A, it is assumed there is a step (as shown in the figure) in the cowl which would trigger the normal shock. From point A, a normal shockwave (shock angle of 90 degrees) is propagated until it intersects with the last reflected shockwave at point T. Both types of intersection are shown in the figure. This is an approximation to the real system. In reality, a bow shockwave would be generated at the trip point and would position itself according to the back pressure in the inlet. However, for the purpose of this research, assuming the constant 90 degree normal shock is adequate.

Point T is known as the triple point. At this point, a reflected shock is generated and a slip line (shown by the dashed line at point T) is formed. Across a slip line, flow angle and pressure must equal but temperature and velocity are not necessarily equal. However, because of the initial approximation, meeting both of these criteria is impossible without a higher order solution. It was chosen to match flow angle instead of pressure. This decision was made because the slip line could, in theory, adjust quickly downstream of the triple point to match the pressure since the flow is subsonic and information is able to pass across the slip line. The alternative situation of having the flow angle be different at a single point is more non-physical. As a result, the reflected shock angle is determined by matching the flow angle at the triple point. This shock angle (another approximation) is held constant for the remainder of the reflected shock propagation until it intersects the centerbody from

point T. At this stage, the flow is subsonic and the program is complete.

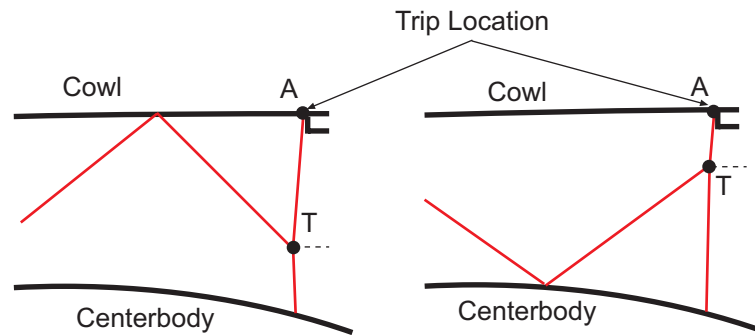


Figure 2.9 Diagram of Lambda Shock and Triple Point Location

#### 2.3.4 Isentropic Flow Procedure

A sketch of an isentropic surface is shown in Figure 2.10. An isentropic surface is designed such that small increases in surface angle compress the flow without causing the characteristic lines to cross (causing shock waves to form). Ideally, this is done so that all working characteristic lines intersect at the cowl leading edge as shown in the figure. From the initial data line, as in Section 2.3.2.1, the nearest point to the boundary is sent to intersect the surface. However, the second surface point is an unknown at this point. To start the solution, two guesses are made, a change in surface angle that is large and one that is very small. The remaining flowfield points are calculated for both starting guess. Then, using the false position method<sup>32</sup>, the change in surface angle is iterated until the next characteristic line intersects at the cowl leading edge. This process is repeated until the desired surface angle and/or surface Mach number is reached. This procedure was validated by successfully testing the program with the design cases used in Reference 34.

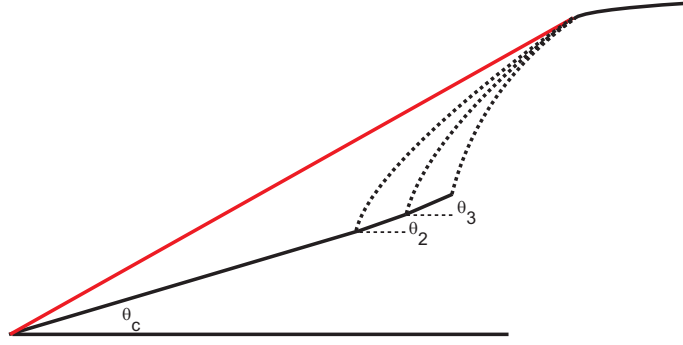


Figure 2.10 Diagram of an Isentropic Inlet Procedure

## 2.4 Thermodynamic Relations

### 2.4.1 Flowfield Relations

The following relations were used to calculate the change in thermodynamic properties for a calorically perfect gas from point-to-point. The equations were found by relating the adiabatic total properties between two points 1 and 2 and then relating point 2 to freestream conditions.

$$\frac{P_2}{P_\infty} = \frac{P_1}{P_\infty} \frac{P_{t2}}{P_{t1}} \left( \frac{1 + \frac{\gamma-1}{2} M_1^2}{1 + \frac{\gamma-1}{2} M_2^2} \right)^{\frac{\gamma}{\gamma-1}} \quad (2.17)$$

$$\frac{T_2}{T_\infty} = \frac{T_1}{T_\infty} \left( \frac{P_{t2}}{P_{t1}} \right)^{\frac{\gamma-1}{\gamma}} \left( \frac{1 + \frac{\gamma-1}{2} M_1^2}{1 + \frac{\gamma-1}{2} M_2^2} \right) \quad (2.18)$$

$$\frac{\rho_2}{\rho_\infty} = \frac{\rho_1}{\rho_\infty} \left( \frac{P_{t2}}{P_{t1}} \right)^{\frac{1}{\gamma}} \left( \frac{1 + \frac{\gamma-1}{2} M_1^2}{1 + \frac{\gamma-1}{2} M_2^2} \right)^{\frac{1}{\gamma-1}} \quad (2.19)$$

The total pressure is found from entropy as

$$\frac{P_{t2}}{P_{t1}} = e^{\frac{-\Delta s}{R}} \quad (2.20)$$

Of course, when the flow is isentropic between two points the total pressure ratio is equal to 1. The mass flow ratio (defined as the ratio of the local density times velocity to the freestream density times velocity) is found from the conservation of mass as

$$\frac{A_\infty}{A_i} = \frac{\rho_i u_i}{\rho_\infty u_\infty} = \frac{\rho_i}{\rho_\infty} \frac{M_i}{M_\infty} \sqrt{\frac{T_i}{T_\infty}} = \sqrt{\frac{\rho_i}{\rho_\infty} \frac{M_i}{M_\infty} \frac{P_i}{P_\infty}} \quad (2.21)$$

## 2.4.2 Shock Relations

The well known  $\theta$ - $\beta$ - $M$  relation that describes the relationship between upstream Mach number, deflection angle and the corresponding shockwave angle for a calorically perfect gas is given by<sup>33</sup>

$$\frac{\tan(\beta - \theta)}{\tan(\beta)} = \frac{(\gamma - 1)M_1^2 \sin^2(\beta) + 2}{(\gamma + 1)M_1^2 \sin^2(\beta)} \quad (2.22)$$

Solution to the above equation for the shockwave angle requires an iterative approach. However, closed form solutions have been developed. The solution given by Wellmann<sup>35</sup> provides a very fast and accurate solution to the equation<sup>36</sup> and is used in the present work.

The thermodynamic relationships for a calorically perfect gas governing flow

through a shockwave are given by<sup>33</sup>

$$\frac{P_2}{P_\infty} = \frac{P_1}{P_\infty} \left[ 1 + \frac{2\gamma}{\gamma+1} (M_1^2 \sin^2(\beta) - 1) \right] \quad (2.23)$$

$$\frac{\rho_2}{\rho_\infty} = \frac{\rho_1}{\rho_\infty} \left[ \frac{(\gamma+1)M_1^2 \sin^2(\beta)}{(\gamma-1)M_1^2 \sin^2(\beta) + 2} \right] \quad (2.24)$$

$$\frac{T_2}{T_\infty} = \frac{T_1}{T_\infty} \left[ 1 + \frac{2\gamma}{\gamma+1} (M_1^2 \sin^2(\beta) - 1) \right] \left[ \frac{(\gamma+1)M_1^2 \sin^2(\beta)}{(\gamma-1)M_1^2 \sin^2(\beta) + 2} \right]^{-1} \quad (2.25)$$

$$\frac{P_{t2}}{P_{t\infty}} = \frac{P_{t1}}{P_{t\infty}} \left[ 1 + \frac{2\gamma}{\gamma+1} (M_1^2 \sin^2(\beta) - 1) \right]^{-\frac{1}{\gamma-1}} \left[ \frac{(\gamma+1)M_1^2 \sin^2(\beta)}{(\gamma-1)M_1^2 \sin^2(\beta) + 2} \right]^{\frac{\gamma}{\gamma-1}} \quad (2.26)$$

and

$$M_2 = \frac{1}{\sin(\beta - \theta)} \sqrt{\frac{M_1^2 \sin^2(\beta) + \frac{2}{\gamma-1}}{\left[ \frac{2\gamma}{\gamma-1} \right] M_1^2 \sin^2(\beta) - 1}} \quad (2.27)$$

where the subscript 1 corresponds to the condition before the shockwave and the subscript 2 corresponds to the condition after the shockwave. Note all thermodynamics ratios are related to the freestream conditions.

### 3 SR-71-Type Inlet Analysis & Results

#### 3.1 Geometry Definition

No comprehensive diagrams of the SR-71 inlet were identified, so a representative geometry had to be inferred from various YF-12<sup>37,38</sup> reports and the *SR-71 Flight Manual*. Figure 3.1 is a detailed schematic of the YF-12 inlet. The dimensions given in the figure are in terms of  $x/R$  (length normalized by the radius of the cowl). The radius of the cowl was determined by assuming that the inlet had zero spillage at the design Mach number. The captured stream tube area at the cruise Mach number was given as  $18.5 \text{ ft}^2$  in Section 1.2.1.1. From that number, a cowl radius of about 2.43 ft. was assumed—this allowed the true dimensions in Figure 3.1 to be found. From Ref. 37 and the newly determined dimensions of the figure, the angle of the conical spike was found to be  $13^\circ$ . The shoulder of the inlet (the transition from the linear spike to the linear rear section of the centerbody) was approximated by a cubic spline. The inner cowl was assumed to be a circular arc. After several iterations of the method of characteristics solution, the initial cowl angle was found to be  $3^\circ$ —at this angle the reflected shock waves remain attached at Mach 1.7 (the starting Mach number) but not at Mach 1.6. The resultant geometry is shown

in Figure 3.2, where the solid line is the position of the spike in the most forward position and the dashed line is the position of the spike in the most aft (at the cruise speed) position. [Note the step in the figure at about  $x = 3.5$  is the location of the throat section where the computer code assumes the start of a lambda shock structure].

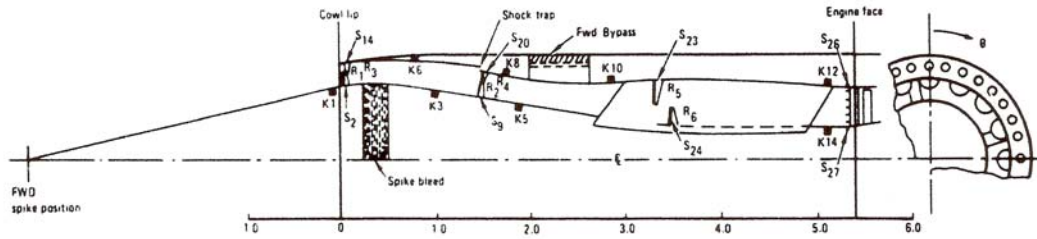


Figure 3.1 YF-12 Inlet Schematic<sup>38</sup>

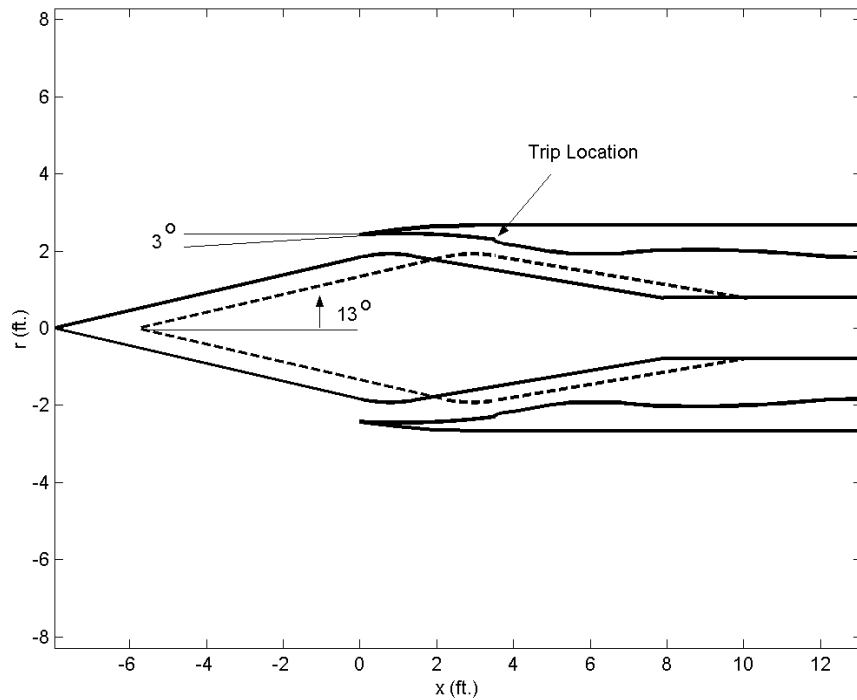


Figure 3.2 Assumed Inlet Geometry

## 3.2 Self-Starting Characteristics

Since the geometry is now known, the area across the cowl face and at the throat can be calculated. Using those two areas and the mass-averaged Mach number entering the cowl (found from the solution to the Taylor-Maccoll equation), the self-starting characteristics are calculated using the Kantrowitz limit, Eq. (1.2). Figure 3.3 is the resulting plot. As the figure shows, the inlet does indeed self-start at Mach 1.7 (i.e. the area ratio is below the Kantrowitz limit) and then proceeds to move away from the Kantrowitz limit, in parallel with the isentropic limit. Note this figure does not take into account any of the bleed or bypass losses that would invariably change the amount of mass flow in the internal contraction section and change the properties of the figure.

It should also be noted that the properties of the SR-71-type inlet (and the proposed modifications) were calculated under the assumption that the incoming air is uniform and traveling at the flight Mach number. In reality, the flow will be perturbed depending upon the placement of the inlet on the aircraft. In the real case of the SR-71, the flow going into the inlet is disturbed by the conical shock coming off of the nose ( $\sim 18^\circ$  cone) of the vehicle. CFD analysis<sup>39</sup> performed on the SR-71 showed that the nose shock fell outside of the inlet at the design speed of Mach 3.2 as shown in Figure 3.4. Johnson and Montoya<sup>37</sup> state that on average the local Mach number at the spike tip of the YF-12 (from flight data) was never more than 3 percent less than the freestream Mach number. This perturbation is less than the theoretical Mach number behind a conical shock off of an  $18^\circ$  cone; however, in looking closely

at Figure 3.4, it does appear that the shockwave has weakened before it draws near to the inlet, most likely due to the expansion waves generated on the lateral surfaces of the vehicle. Nevertheless, as previously stated, the effects of the nose shock are ignored in this analysis.

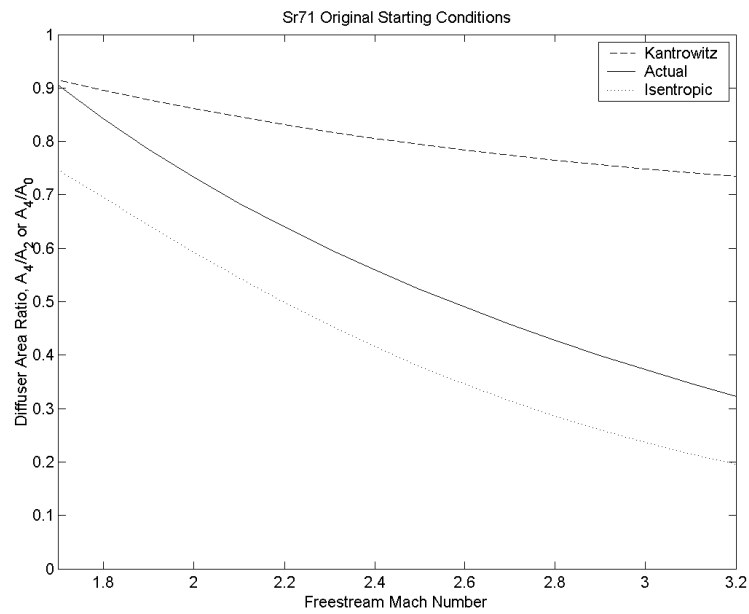


Figure 3.3 Self-Starting Characteristics of the SR-71 Inlet

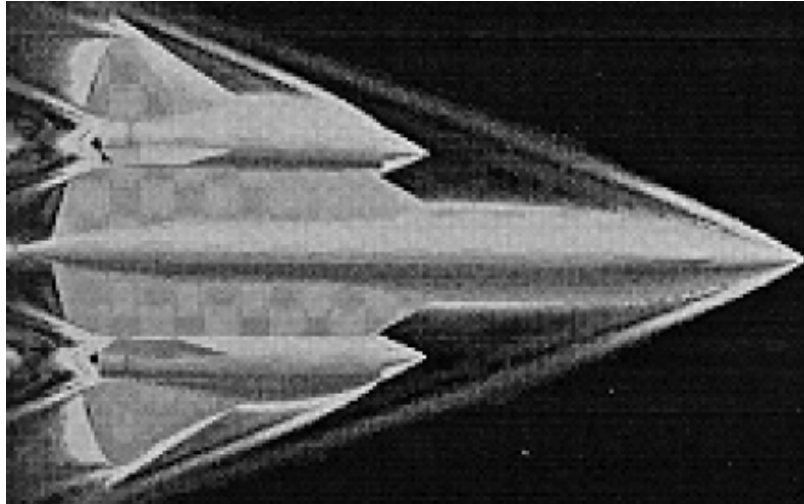


Figure 3.4 Full Vehicle Mach 3.2 CFD Shockwave Patterns (top view)<sup>39</sup>

### 3.3 Flowfield Properties

Contours of the flowfield properties in the SR-71 inlet are presented in Figures 3.5 through 3.9. The figures show contours of Mach number, total pressure ratio, temperature ratio, pressure ratio and mass flow ratio for freestream Mach numbers of 1.7, 2.0, 2.5, 3.0 and the final shock-on-lip design point of Mach 3.2. Note the line emanating off of the tip of the centerbody is the spike tip shock and the first zone of each contour plot represents the first captured, left running characteristic, not a shockwave. The discontinuous breaks in the contours are, however, shockwaves. Also note that the contours only show the supersonic conditions prior to the lambda shock system (plotting a sliver of subsonic flow would distort the contour levels).

Starting at Mach 1.7, the contours indicate that the initial reflected shock off of the cowl leading edge intersects the centerbody on the shoulder (i.e. the curved

segment of the centerbody), causing the flow to re-expand to a higher-than-freestream Mach number (locally). This increase in local Mach number allows the second reflected shock to remain attached (Note the previous discussion of determining the angle of the cowl leading edge). This also produces a near-sonic (choked flow) condition just downstream of the second reflection system. Because the shoulder continues to turn, the flow is able to expand, and subsequent shocks can be formed. The remainder of the shock train progresses (the solutions shows about 6-7 total reflections) and the effect of the expansion waves propagating through the system is readily apparent, especially in the temperature plots. Due to the presence of the expansion waves and shock train, temperature and pressure end up being near to or less than the freestream values at the throat entrance at the lower Mach numbers.

As the freestream Mach number increases and the spike retracts, the plots show the progression of the shock train through the duct. The initial reflection off the cowl leading edge gradually moves off of the shoulder to the conical segment of the centerbody stopping any expansion prior to the first reflection. The expansion wave angles also begin to decrease as is shown by the movement of the expansion system down the duct—this is to be expected with higher speeds. By Mach 2.5, the initial cowl shock has moved onto the conical section of the centerbody and the total number of reflections has been decreased to about 4. At Mach 3.2, only 2 or 3 reflections occur. Local regions of high temperature and pressure on the cowl are also apparent at Mach 3.2 but by the time the flow nears the throat, this effect is mitigated by the presence of the expansion waves.

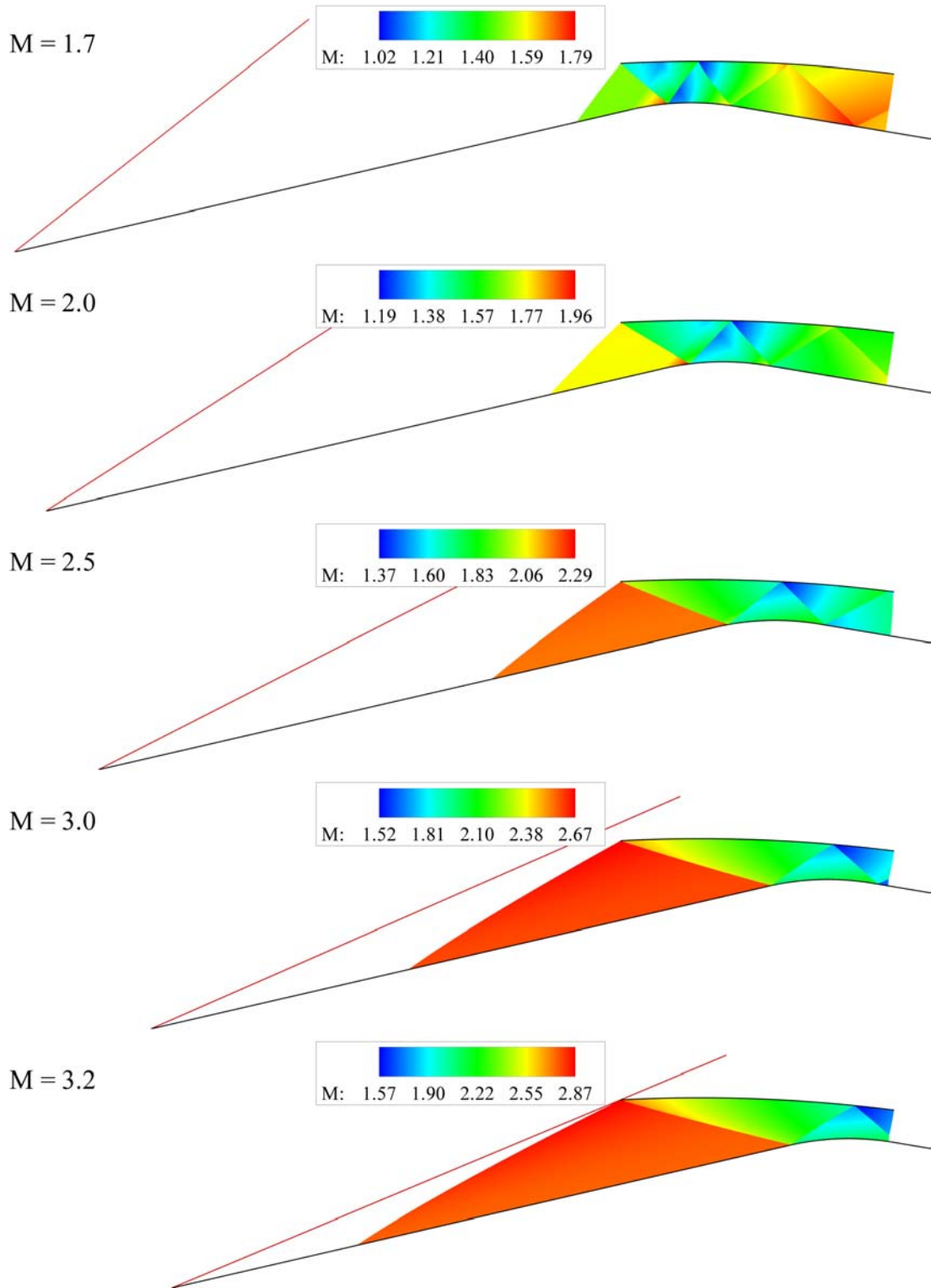


Figure 3.5 SR-71 Inlet Mach Number Contours

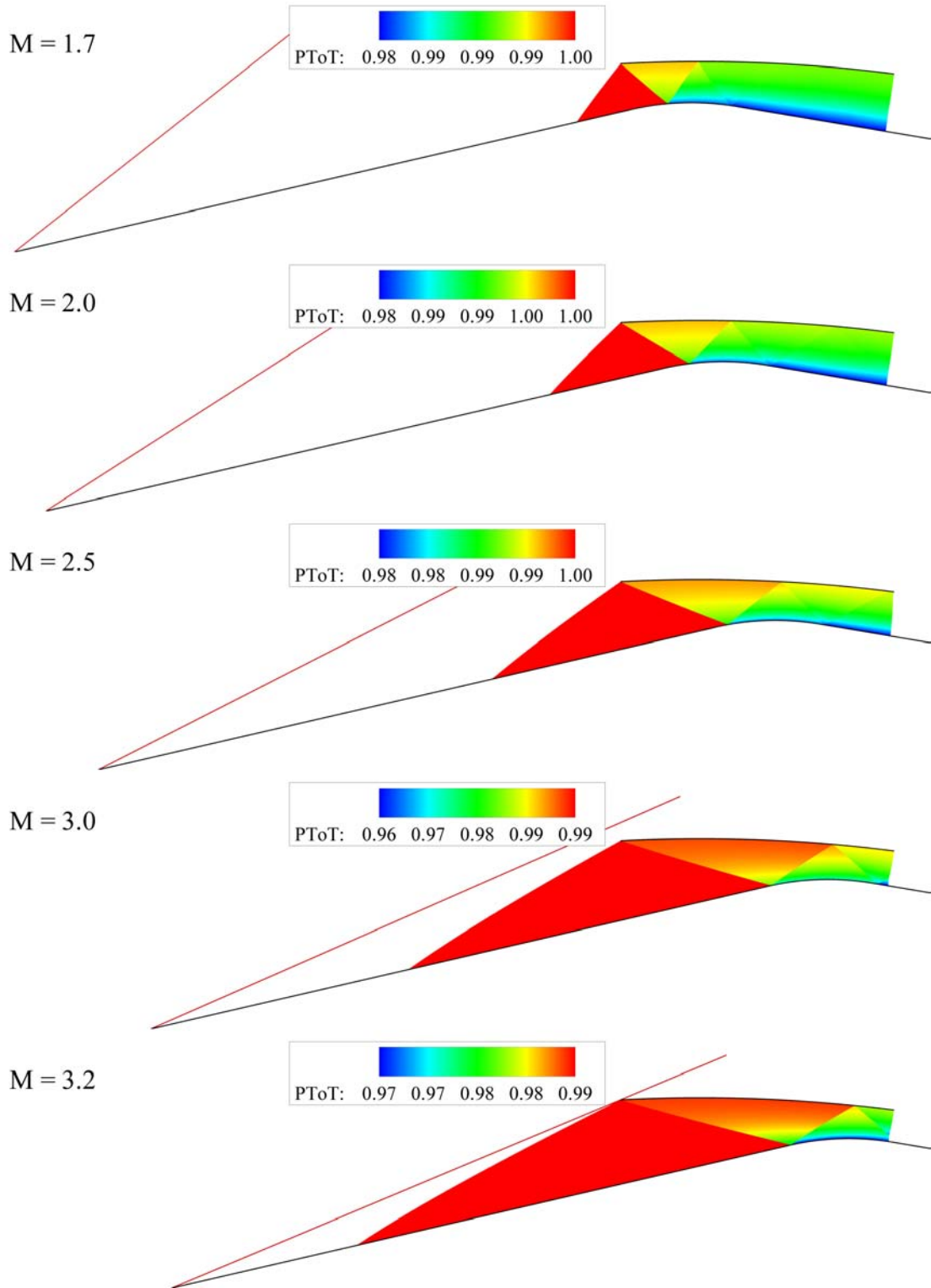


Figure 3.6 SR-71 Inlet Total Pressure Ratio Contours

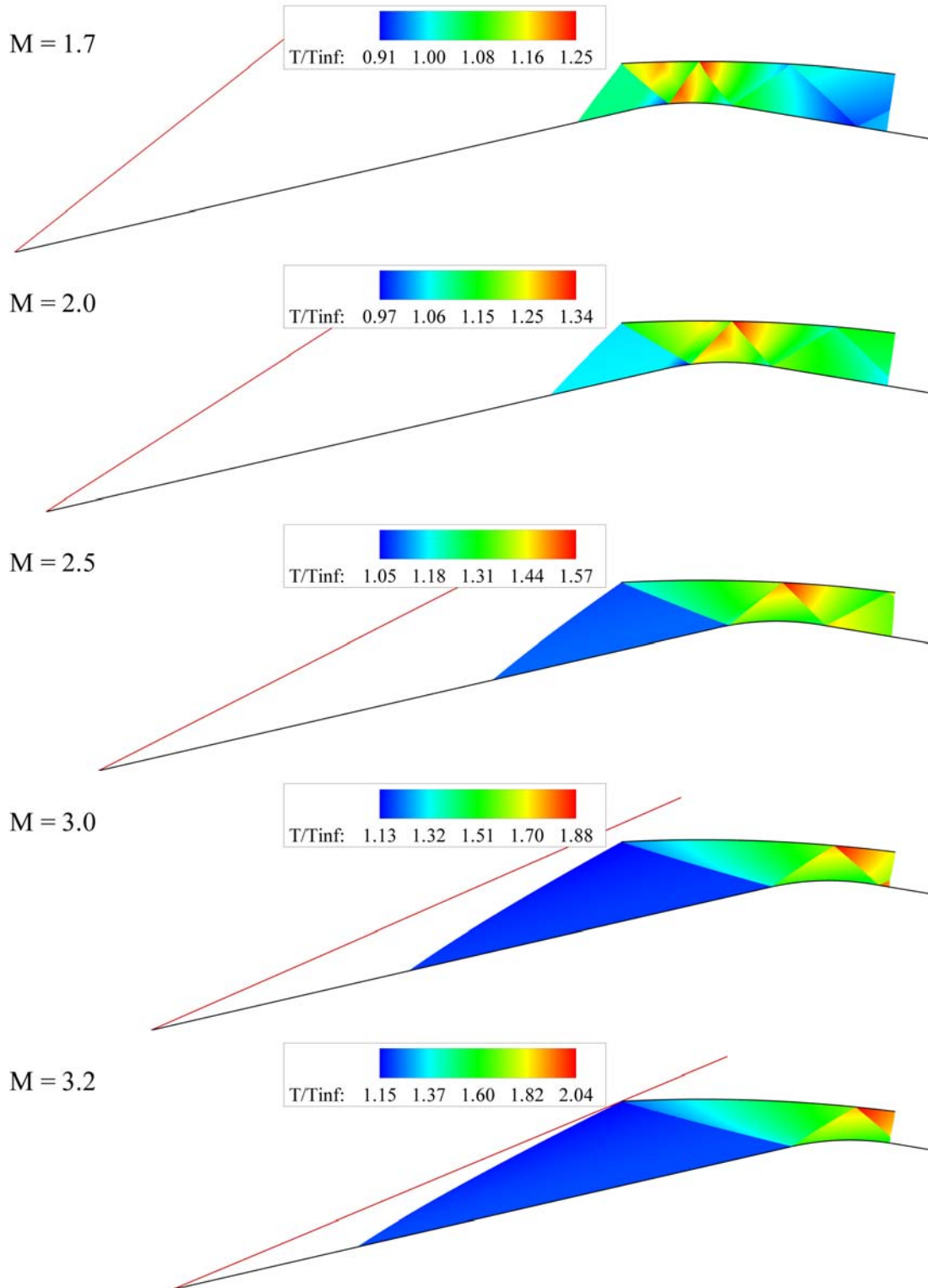


Figure 3.7 SR-71 Inlet Temperature Ratio Contours

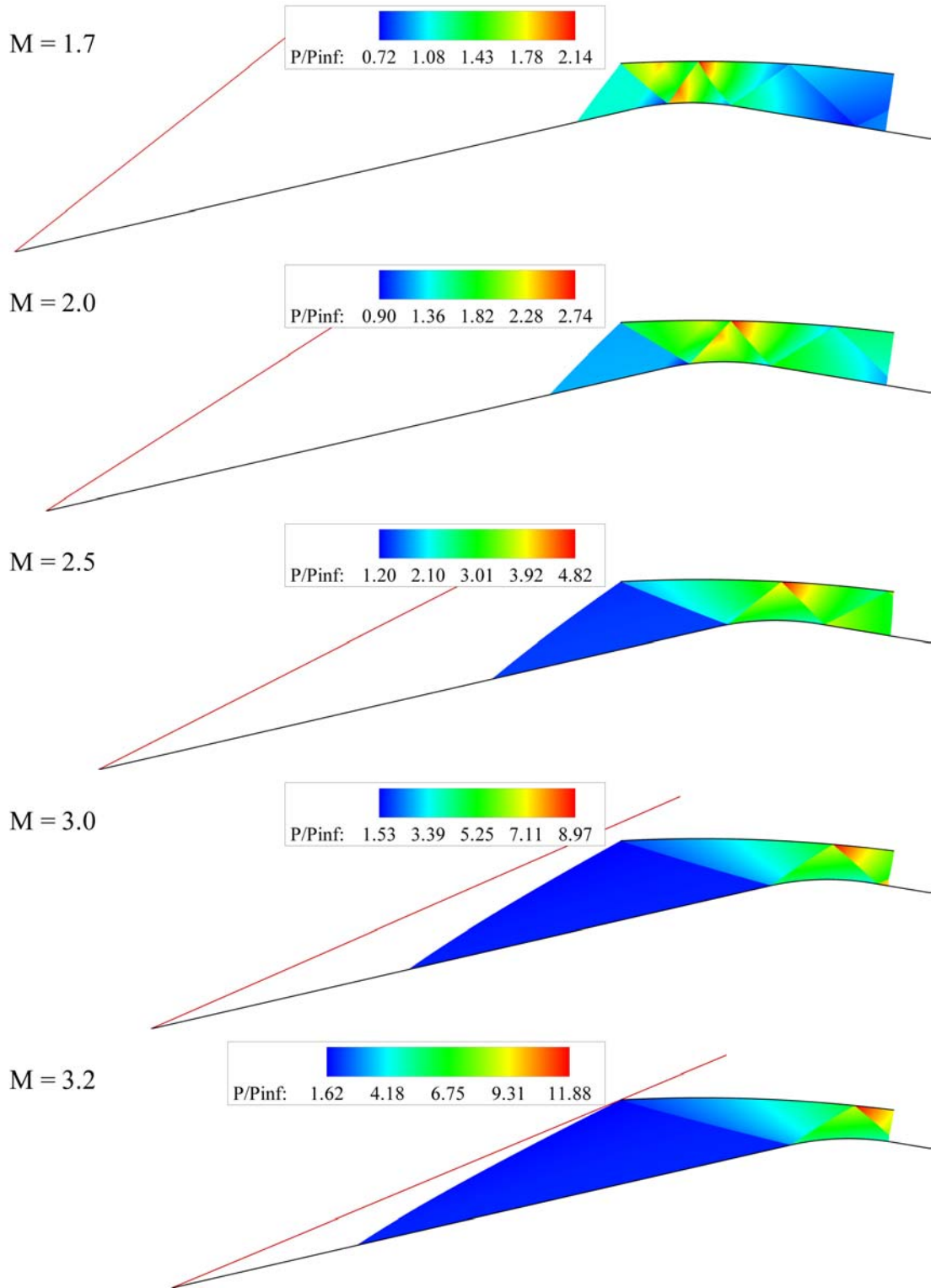


Figure 3.8 SR-71 Inlet Pressure Ratio Contours

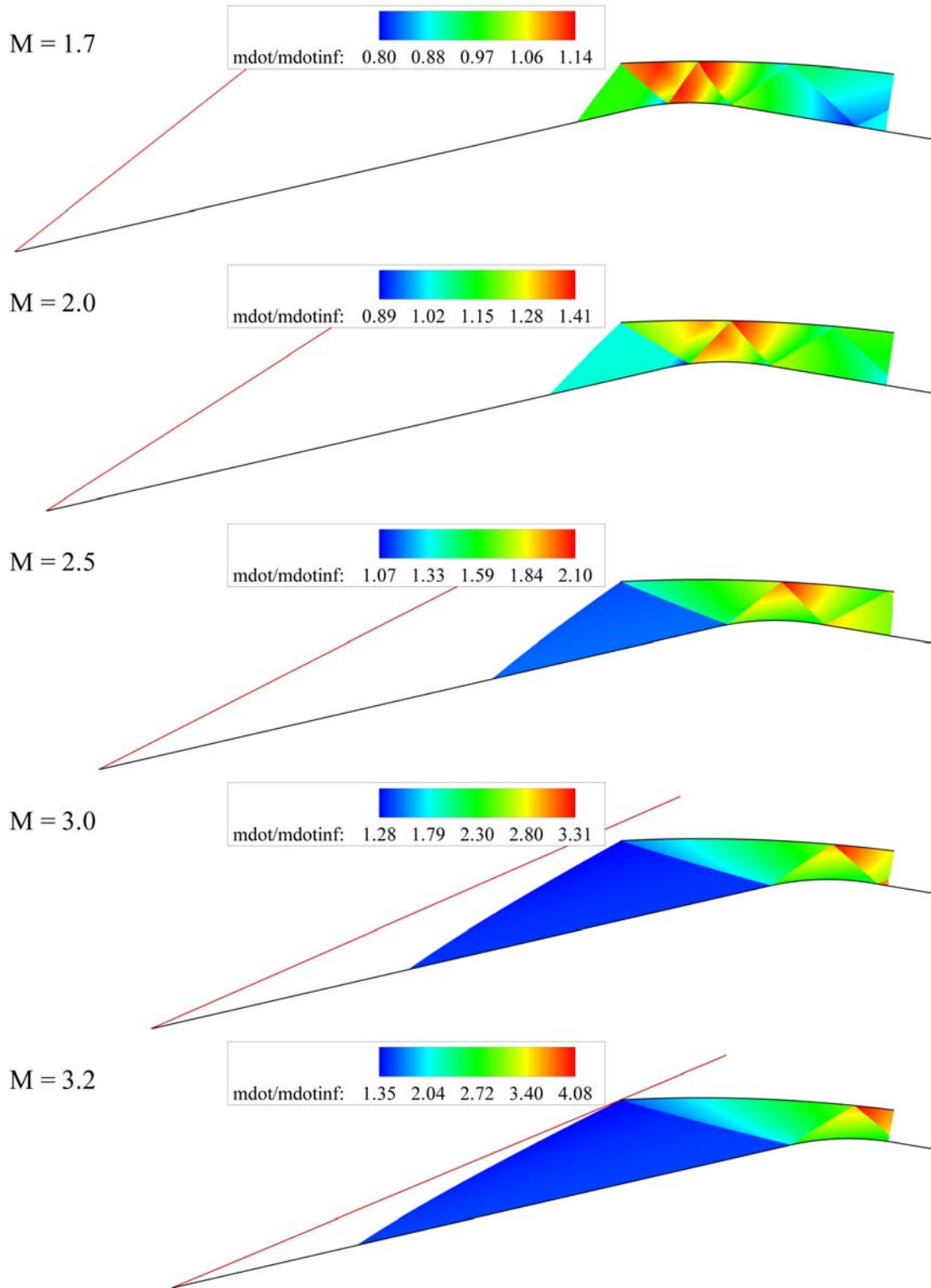


Figure 3.9 SR-71 Inlet Mass Flow Ratio Contours

### 3.4 Throat Conditions

The area-averaged supersonic and subsonic properties at the throat are shown in Figures 3.10 and 3.11, respectively. The levels of distortion are quantified as well. The supersonic plot shows a gradual rise in pressure, temperature and mass flow with freestream Mach number. The supersonic throat Mach number initially decreases and then increases (with a final throat entrance Mach number of about 1.8) whereas the total pressure ratio initially increases and then decreases as the freestream speed is increased. The total pressure ratio distortion is small and always stays below three percent. Distortion levels for Mach number and temperature are moderate, remaining at or below 20 percent. Pressure and mass flow distortion levels are large, rising to ~50 percent and ~30 percent, respectively. However, this is to be expected as the area averaging for the supersonic throat conditions takes place across a shockwave where there would be marked changes in the flow properties.

The subsonic plots agree show that Mach number initially increases and then decreases (with a final throat exit Mach number of about 0.61) whereas all of the other flow properties have the same general trend as the supersonic plot. However, the levels of the distortion of the total pressure ratio increased significantly while the levels of distortion of Mach number, temperature and pressure decreased from the supersonic case (both mass flow plots are identical, as they should be). Any errors in the subsonic properties are a direct result of the assumed lambda shock structure described in Section 2.3.3.3.

As shown, the subsonic temperature and pressure ratios at Mach 3.2 are about

2.8 and 30, respectively. The pressure ratio is lower than the value of 40 reported by Kelly Johnson (former head of the Skunk Works)<sup>18</sup>. The temperature ratio is below the maximum compressor inlet temperature ratio of 3.23 (assuming flight at 90,000 ft.)<sup>13</sup>. However, real gas and viscous effects have been ignored. Additionally, there will be changes to the flowfield as the air moves through the subsonic portion of the inlet prior to entering the compressor. If the flow (at a static pressure ratio of 30) were isentropically compressed to zero velocity, the pressure ratio would rise to 39, much closer to the quoted value.

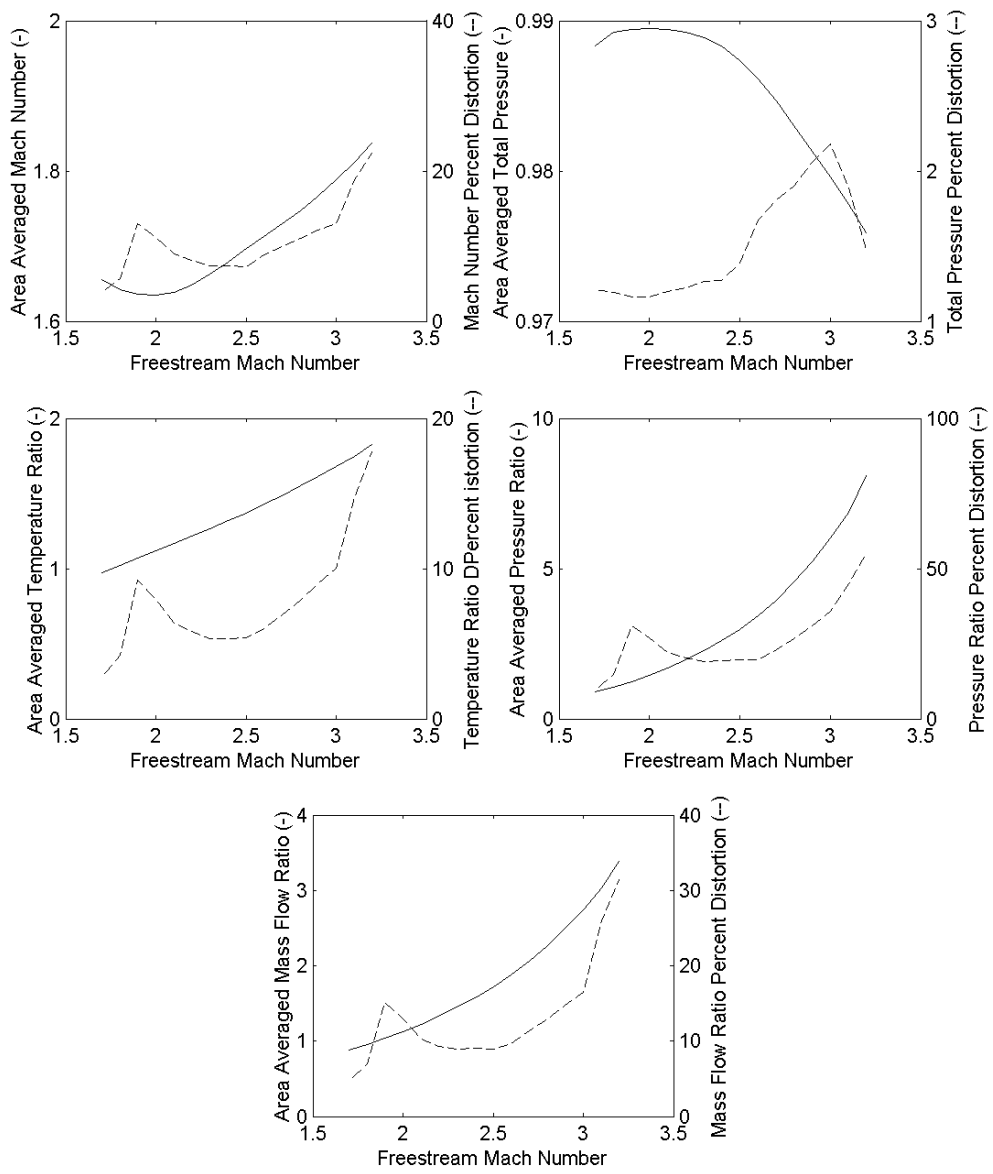


Figure 3.10 Supersonic SR-71 Throat Properties

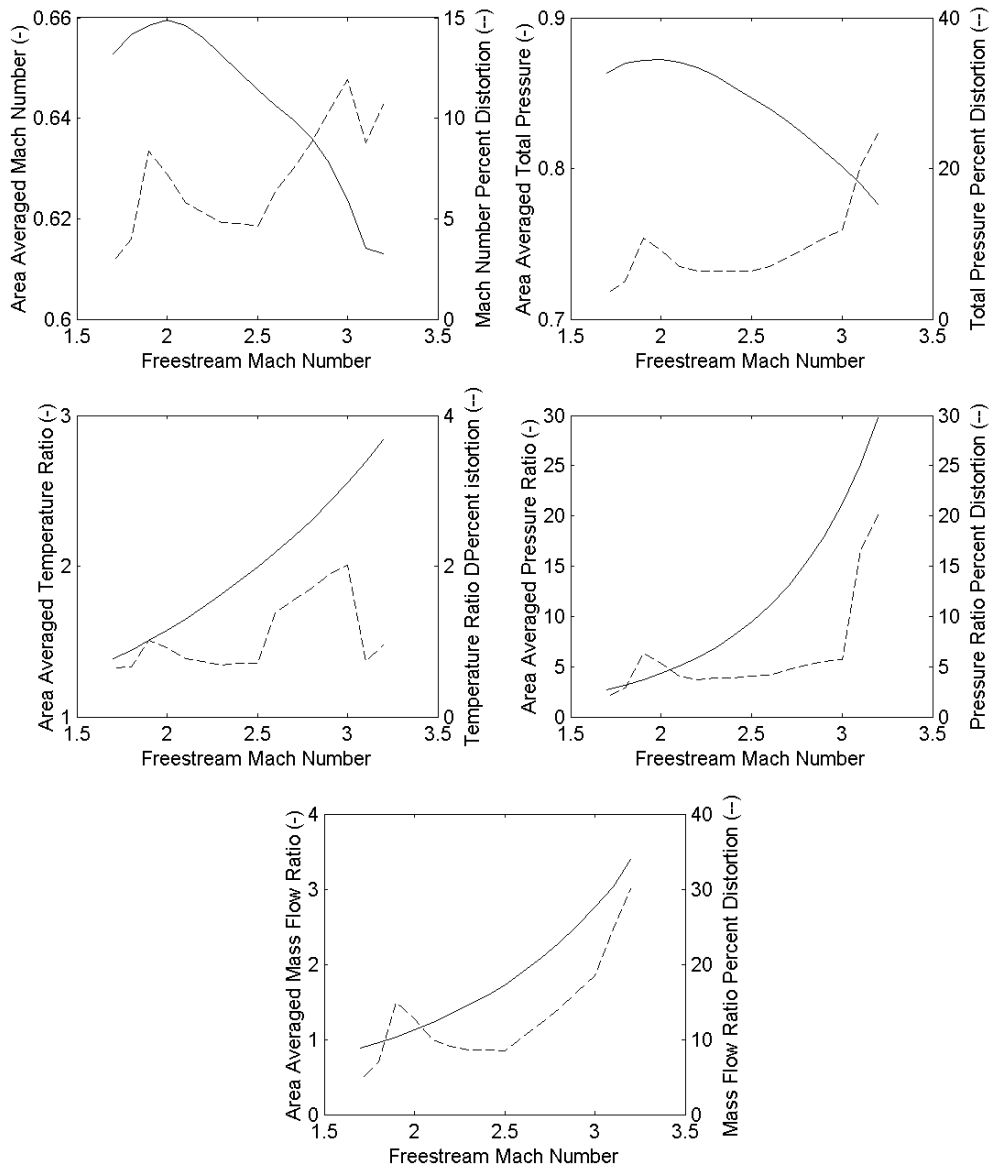


Figure 3.11 Subsonic SR-71 Throat Properties

## 4 CFD Validation

### 4.1 Inviscid Analysis

Computational fluid dynamics analysis was implemented to validate the method of characteristics model. The program used in the validation process is NASA's OVERFLOW2<sup>40</sup>. OVERFLOW2 solves the full Navier-Stokes equations. The accompanying grid generator is called OVERGRID<sup>41</sup>. Its many features include a hyperbolic grid generator and the ability to create separate, overlapping grids.

The grid used in the validation is shown in Figures 4.1 (external mesh) and 4.2 (enhanced internal mesh) with every fifth grid point removed for clarity. It consists of 701 points in the x direction and 101 points in the z. The grid is stretched at both ends of vertical plane to accurately capture the boundary layer (when solving the viscous equations). The grid is also stretched at the  $x = 4$  (on the centerbody surface) and  $x = 10$  (on the cowl surface) to improve the resolution of the shockwaves. For the inviscid analysis, the cowl and the centerbody boundary conditions were set to be inviscid adiabatic walls. The left plane was set to freestream conditions (Mach 3.2 flow at 90,000 ft. altitude) and the right exit plane was set to be an outflow (with

pressure extrapolation). The top horizontal plane between the left plane and the cowl leading edge was set to be a simple supersonic inflow/outflow. The solution used central differencing (fourth order) and the ARC3D 3-factor diagonal scheme. The CFL number was determined locally. The ratio of specific heats was also held constant at 1.4. As with the MOC cases, the code was run on a Dell Latitude D600 with a 1.6 GHz Pentium M processor and 1 GB of RAM.

The results are shown in Figures 4.3 through 4.5 and compared to the contour plots presented earlier in Chapter 3 of Mach number, temperature ratio and pressure ratio. Note the MOC contours are scaled differently (to match the CFD contour levels) from the plots in Section 3.3 because the CFD includes the freestream properties whereas the MOC contours do not. The two solution methods agree quite well. With the exception of a slight over-prediction (.01 %) in the maximum temperature rise and a minor under-prediction (.4 %) of the maximum pressure rise, the MOC solution obtained almost the same results as the CFD. Note in the CFD results, the maximum contour level of Mach number is higher than the freestream value because the CFD had some difficulty resolving the shock at the spike tip. Similarly, the pressure and temperature minimum level is less than freestream. Also included are the prediction of the surface Mach number, temperature and pressure in Figures 4.6 through 4.8. Again, excellent agreement between the CFD and MOC solutions is obtained. The shock locations are accurately predicted by the MOC code (shown by the discontinuities). As previously mentioned, the run times for most cases of the MOC code (depending on the number of shock reflections) was on the order of 15-20 seconds (with a grid 4 times as fine) whereas the CFD (at 500

iterations) results presented here took a little over 3 minutes.

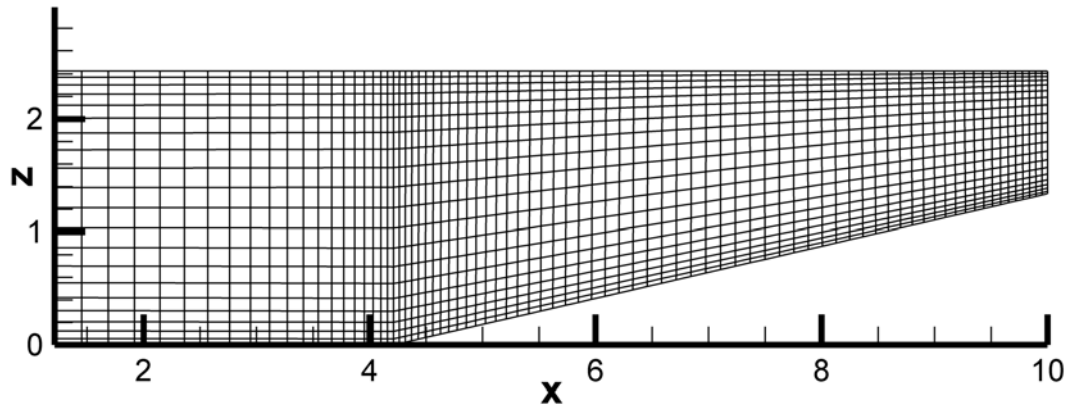


Figure 4.1 External Grid used for CFD Analysis ( $1/5^{\text{th}}$  the resolution)

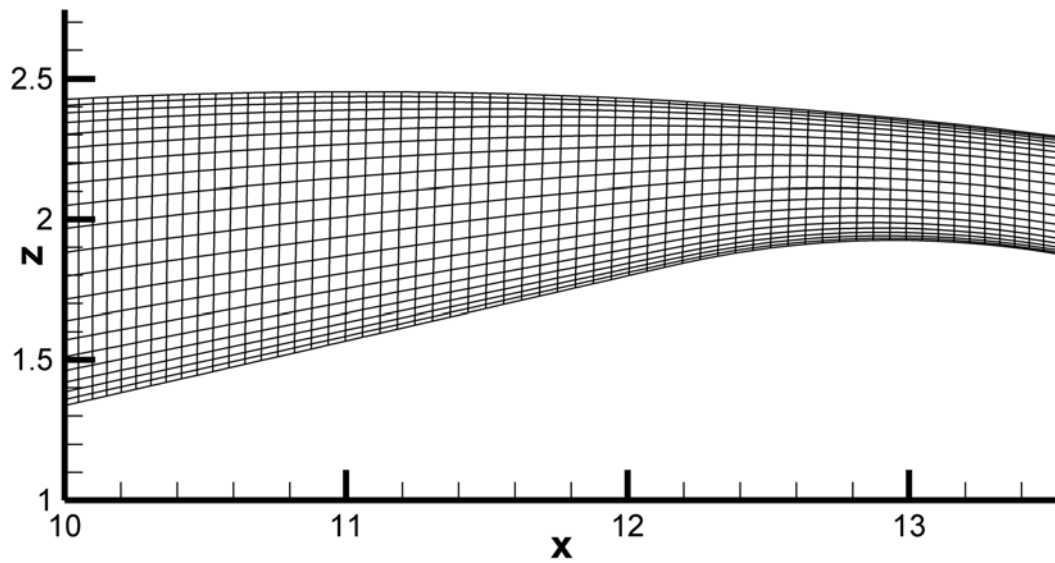


Figure 4.2 Internal Grid used for CFD Analysis ( $1/5^{\text{th}}$  the resolution)

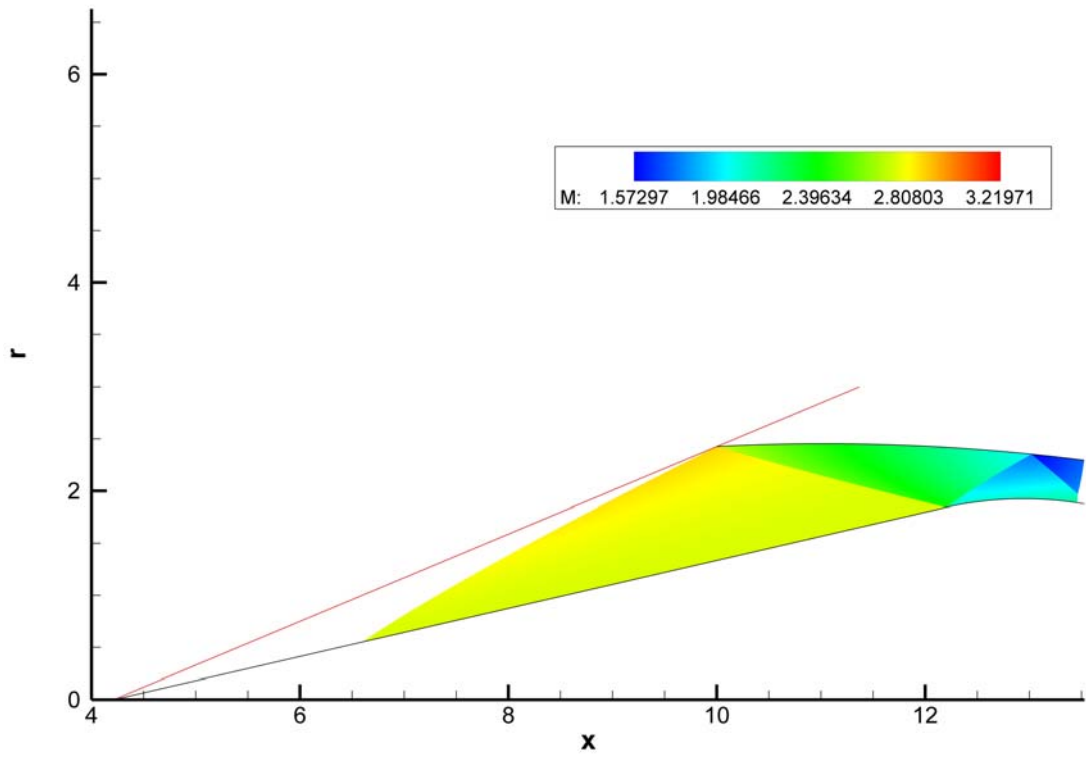
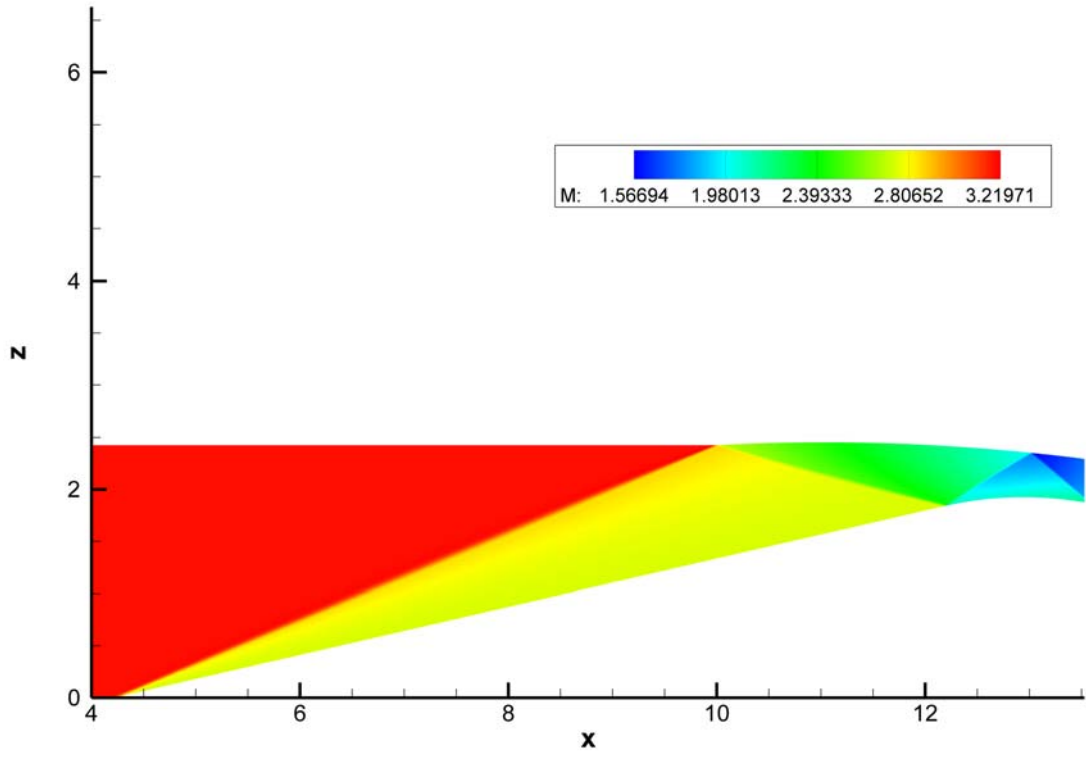


Figure 4.3 Mach Number Contour Comparison (CFD above)

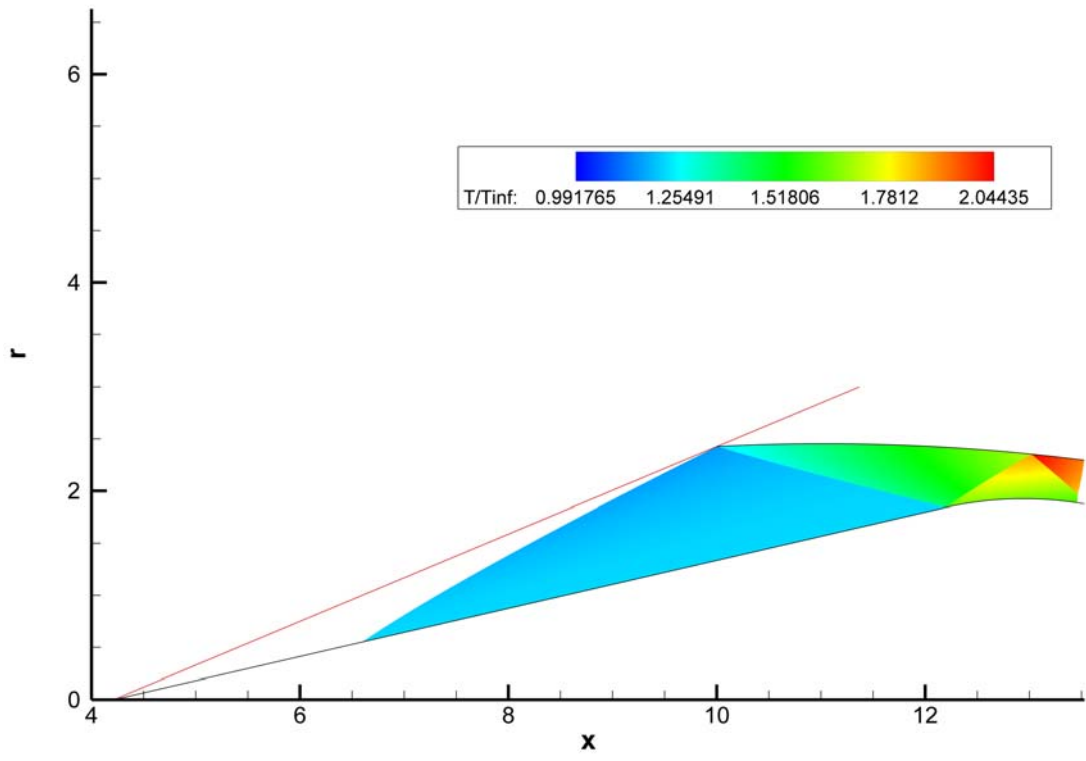
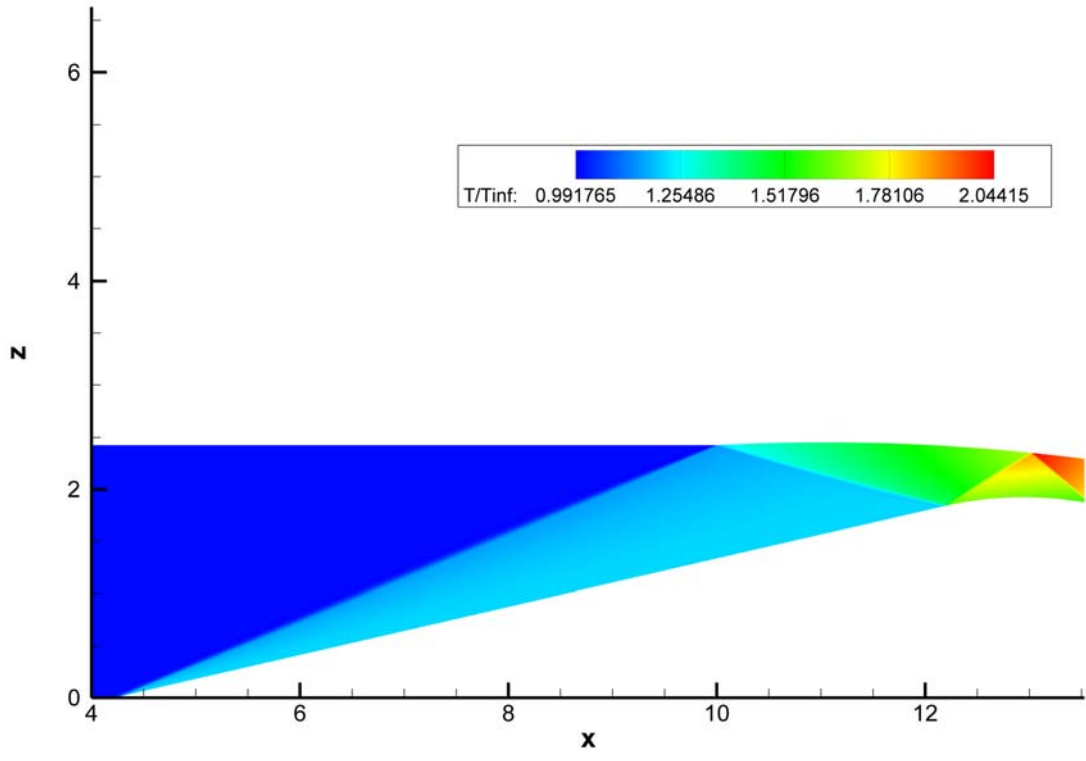


Figure 4.4 Temperature Ratio Contour Comparison (CFD above)

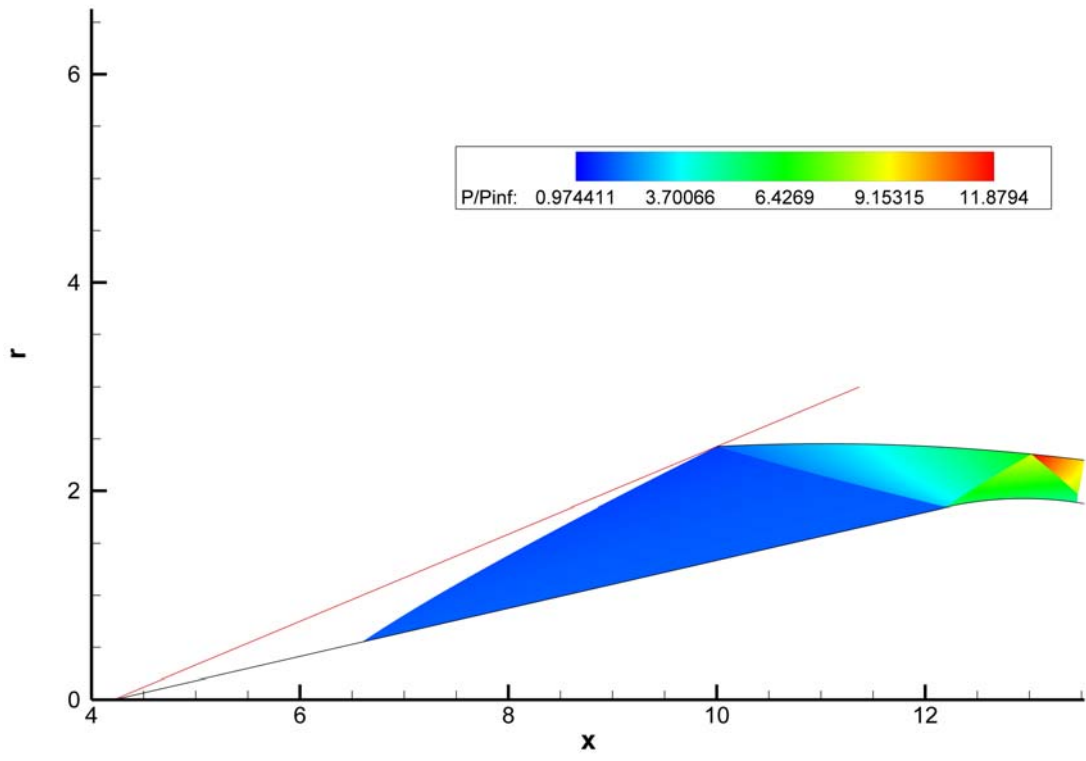
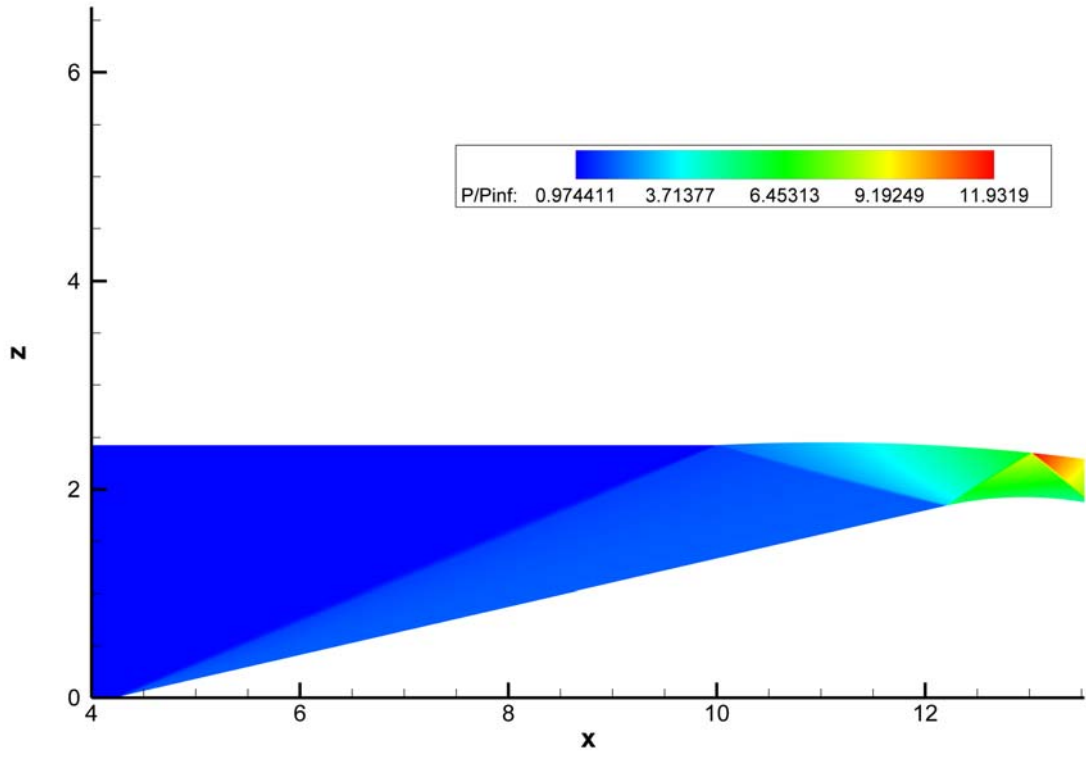


Figure 4.5 Pressure Ratio Contour Comparison (CFD above)

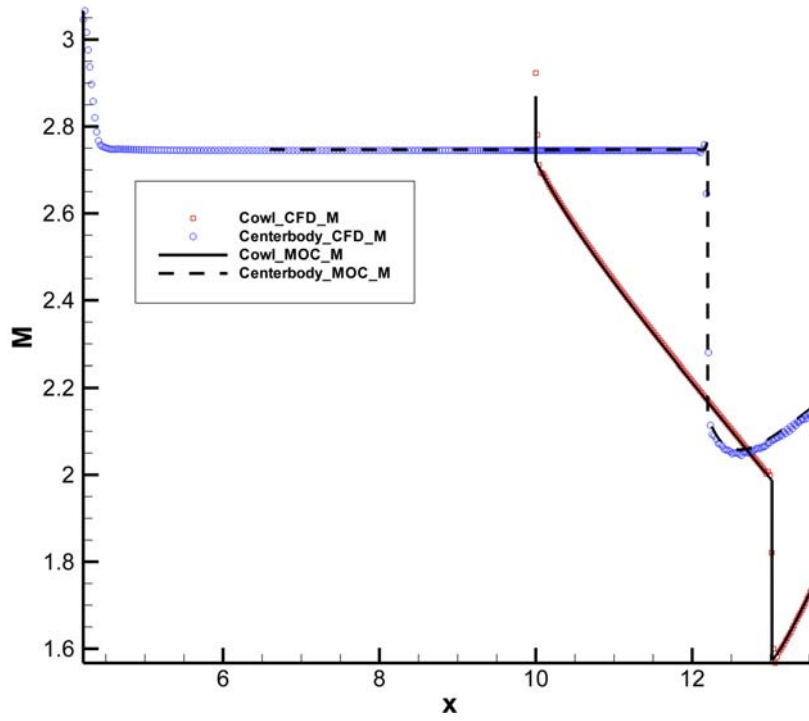


Figure 4.6 Surface Mach Number Comparison

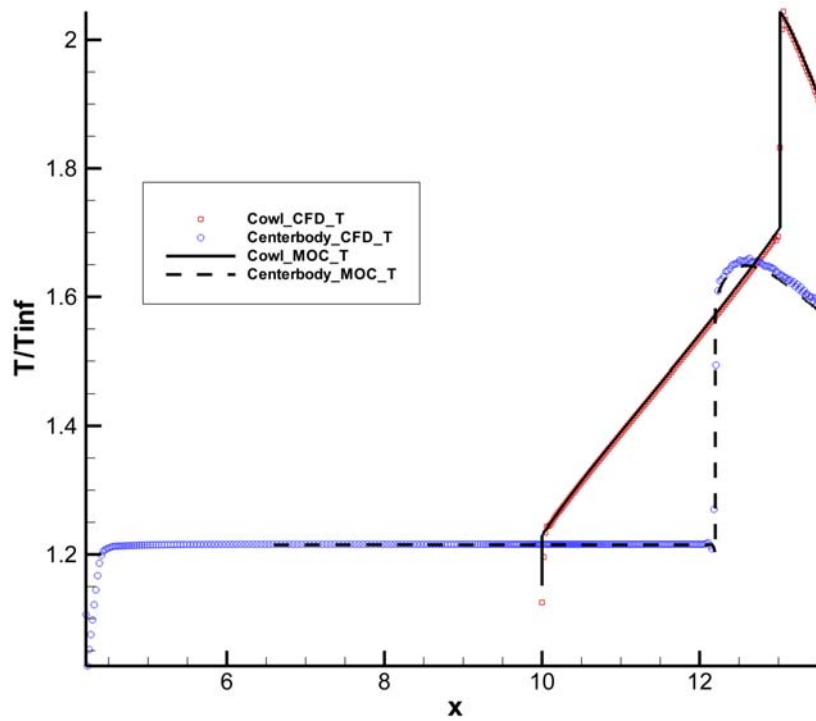


Figure 4.7 Surface Temperature Ratio Comparison

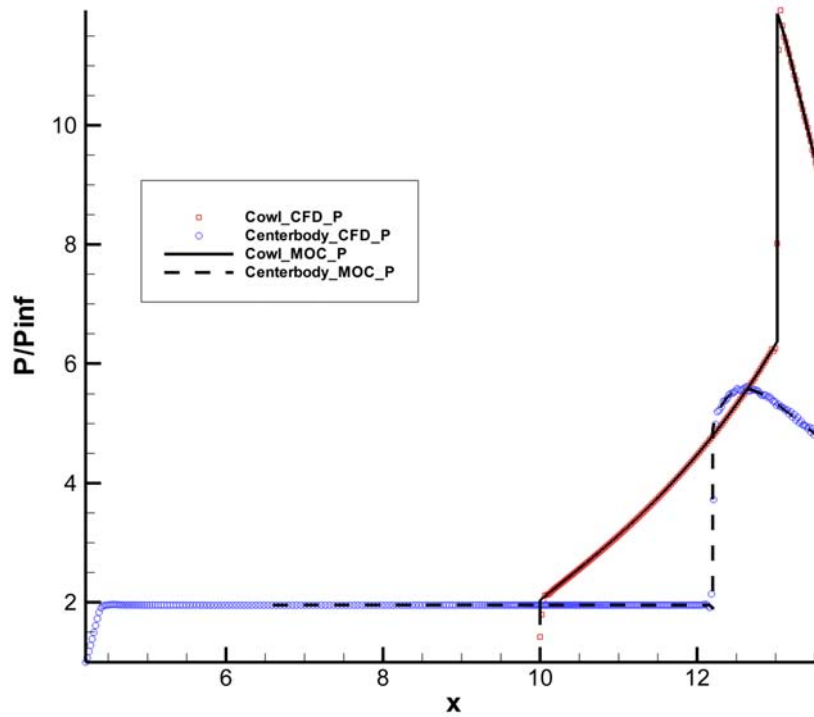


Figure 4.8 Surface Pressure Ratio Comparison

## 4.2 Viscous Analysis

Full viscous analysis of the SR-71 inlet was performed using OVERFLOW2. The turbulence model used was the one-equation Spalart-Allmaras  $R_T$  model (fully turbulent). The results are presented in Figure 4.9. [Note these results are displayed for qualitative purposes only. Each contour shown does not represent a converged solution, i.e. this is not time accurate CFD.] At 500 iterations, the boundary layers along both the cowl and centerbody are developing. At the impingement location of the initial reflected cowl shock, the boundary layer separates and then reattaches—similar results are seen in the shock train downstream. However, at 1000 iterations, the boundary layer along the centerbody appears to have separated even further, but

an oblique shock train still exists. At 1500 iterations, the centerbody boundary layer has almost fully separated, and the shock train downstream has transitioned into a normal shock train. Finally, at 2000 iterations, the inlet has completely unstalled as evidenced by the subsonic flow present throughout the internal duct. The final contour plot shows a second oblique shock is generated on the centerbody surface (outside of the cowl face) followed by a very strong oblique shock that causes the entire inlet flowfield to be subsonic. These results show why the original SR-71 inlet used a bleed system on the spike slightly downstream of where the initial reflected cowl shock impinged on the centerbody. Additionally, the results demonstrate why the designers selected a design such that the impingement location remained relatively constant as the spike retracted as previously discussed in Section 3.3.

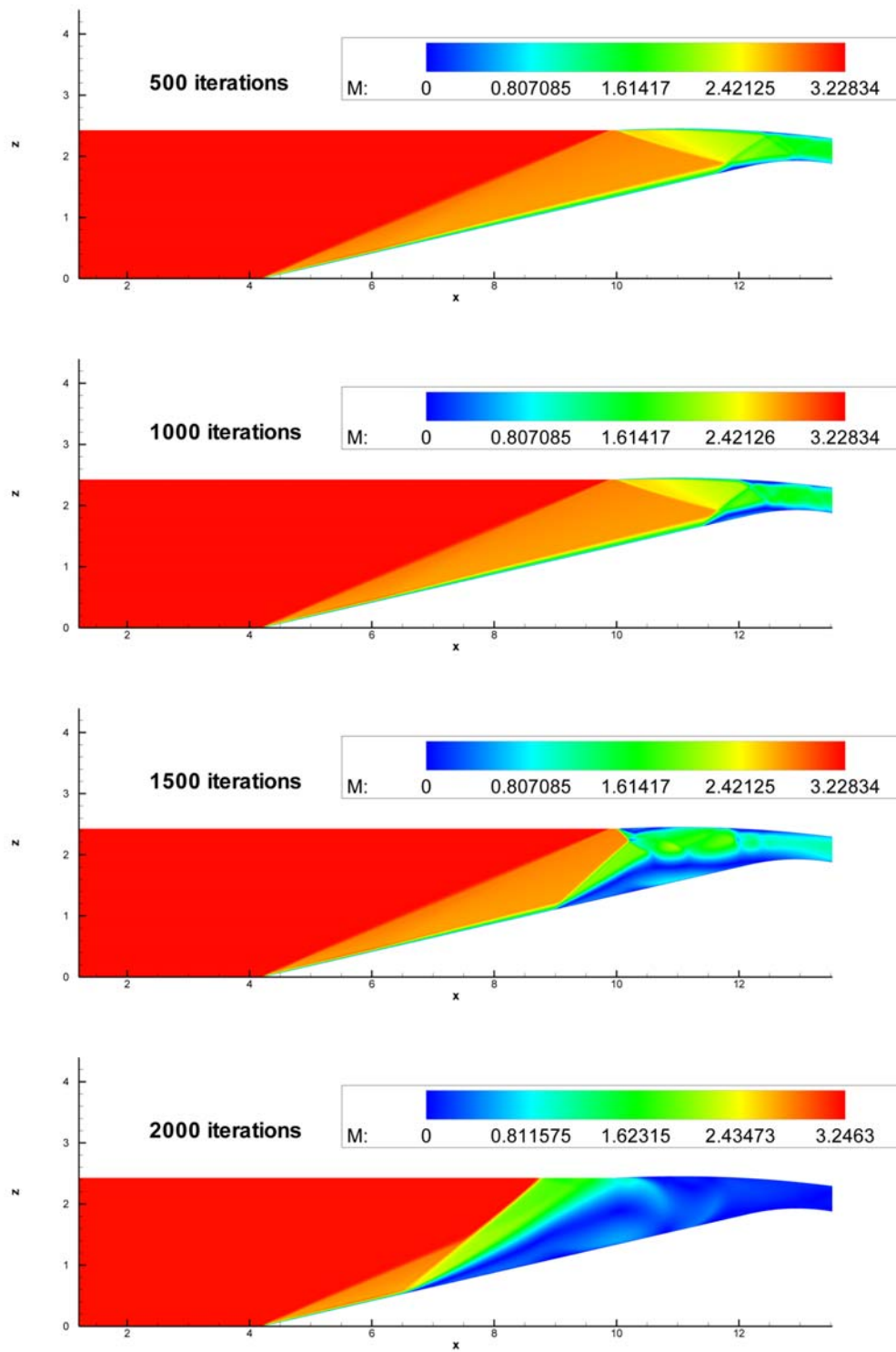


Figure 4.9 Viscous CFD Results

## 5 Modification Analysis & Results

The next six sections detail a variety of means to modify the SR-71 inlet to extend its operation into the hypersonic flight regime. With no modification to the inlet, the centerbody spike shock will move inside of the cowl (past Mach 3.2) and the resulting inlet flowfield would likely degrade. The effect on the overall system (especially mass and installation factors) due to the design changes are not be taken into account at this time. Just as with the original SR-71 inlet, the self-starting characteristics of each scheme are analyzed and, for those inlets that are able to start well past Mach 3.2, the full flow properties will be determined. The constraints on these changes are that the slope of the duct after the throat remains fixed and the new designs have to fit within the original SR-71 cowl. The throat is located at the same axial position as was described in the original SR-71 inlet. Accordingly, the flow is tripped at the throat.

Interestingly, several websites<sup>42,43</sup> have claimed (through published reports) that the SR-71 flew upwards of Mach 3.5 and that the Skunk Works performed studies to see how fast the SR-71 could actually fly. The websites cited the limiting factors to be the interaction of the nose conical shock with the inlet spike and the heat

load on the airframe past Mach 3.5. However, these published reports were never located and the modifications of the inlet (if any) are not known to the author. Additionally, declassified CIA reports indicate that the maximum speed obtained by the SR-71 was actually Mach 3.29<sup>44</sup>. Note that previously mentioned NASA reports said that the inlet Mach number was generally 3 percent less than the flight Mach number. Three percent less than Mach 3.29 is Mach 3.2.

## 5.1 Re-extension of the Original Inlet

As Mach number increases, the shockwave angle decreases. Therefore, the most obvious way to overspeed the inlet (and the least expensive) would be to re-extend the centerbody spike in increments to maintain the shock-on-lip condition at the higher Mach numbers. Assuming the spike could be extended to its original low speed location (and fixing the conical half angle at  $13^\circ$ ), the inlet could be oversped up to a freestream Mach number of about 6.1. Beyond this point, the conical shockwave generated off of the spike would move inside of the cowl.

### 5.1.1 Self-Starting Characteristics

The self-starting characteristics (i.e. the ratio of throat area to cowl area compared to the Kantrowitz limit) of the first redesign scheme are shown in Figure 5.1. As is shown, the inlet would violate the Kantrowitz limit near a freestream Mach number of 4.8. The violation occurs because as the spike is moved forward the throat area decreases while the cowl area increases. This causes a rapid increase in the area ratio (as is seen by the discontinuity in the curve).

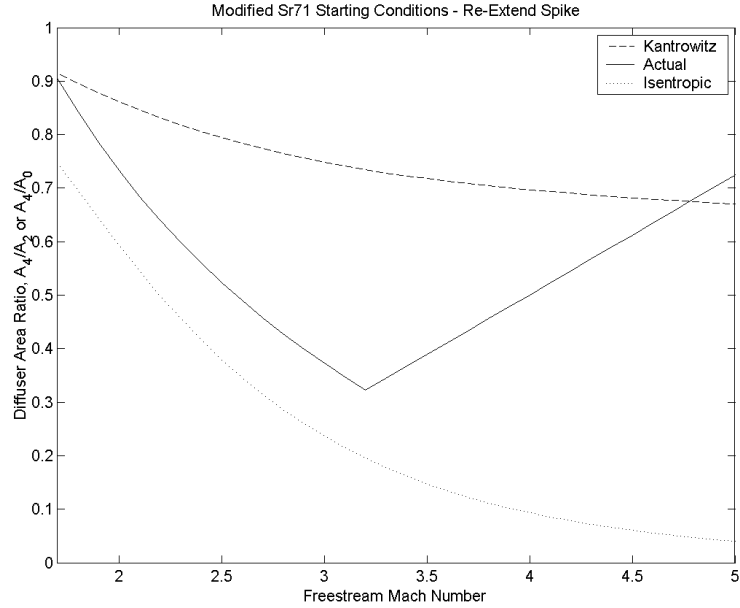


Figure 5.1 Self-Starting Characteristics of the Re-extended Spike

### 5.1.2 Flowfield Properties

Contours of the flowfield of the re-extended spike are shown in Figures 5.2 through 5.6 for a range of freestream Mach numbers within the self-starting regime. The contours show that as freestream Mach number increases, the impingement location of the first reflected cowl shock advances onto the shoulder. This effect, again, causes expansion waves to be generated prior to the first reflection off of the centerbody. As the spike retracts and the initial reflection moves up and around the centerbody shoulder, local regions of high temperature and pressure are present along the cowl; however, these effects are eventually overcome by the presence of the expansion waves. The expanding of the duct also restricts the number of reflections—as is shown by Mach 4.0, two total reflections exist prior to the throat

section. By Mach 4.5, the leading edge shock has moved around the shoulder and by Mach 4.8, it is on the opposite side of the shoulder and is highly curved. Large expansion regions exist prior to the first reflection and large gradients in the flow properties can be seen as a result of this process.

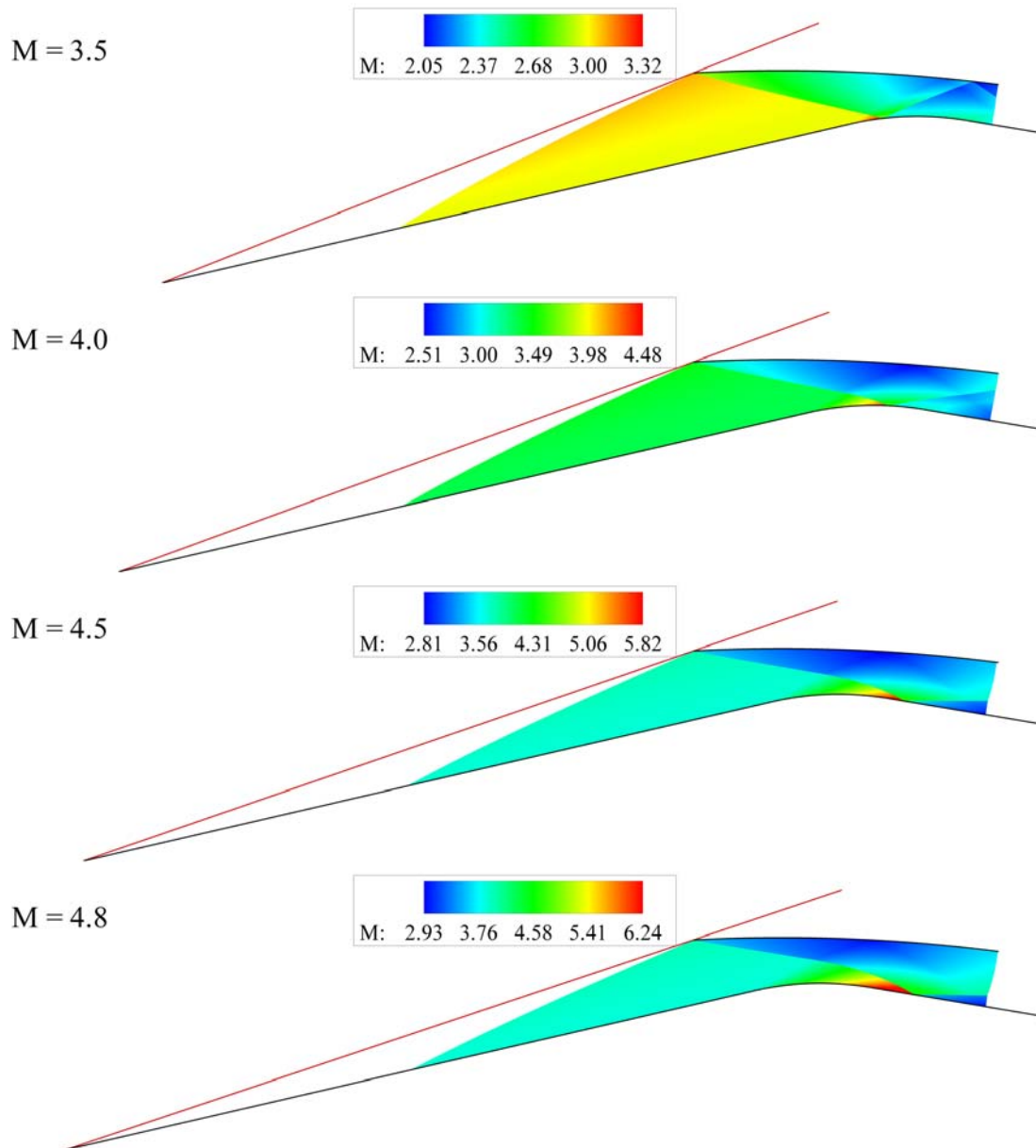


Figure 5.2 Re-extended Spike Inlet Mach Number Contours

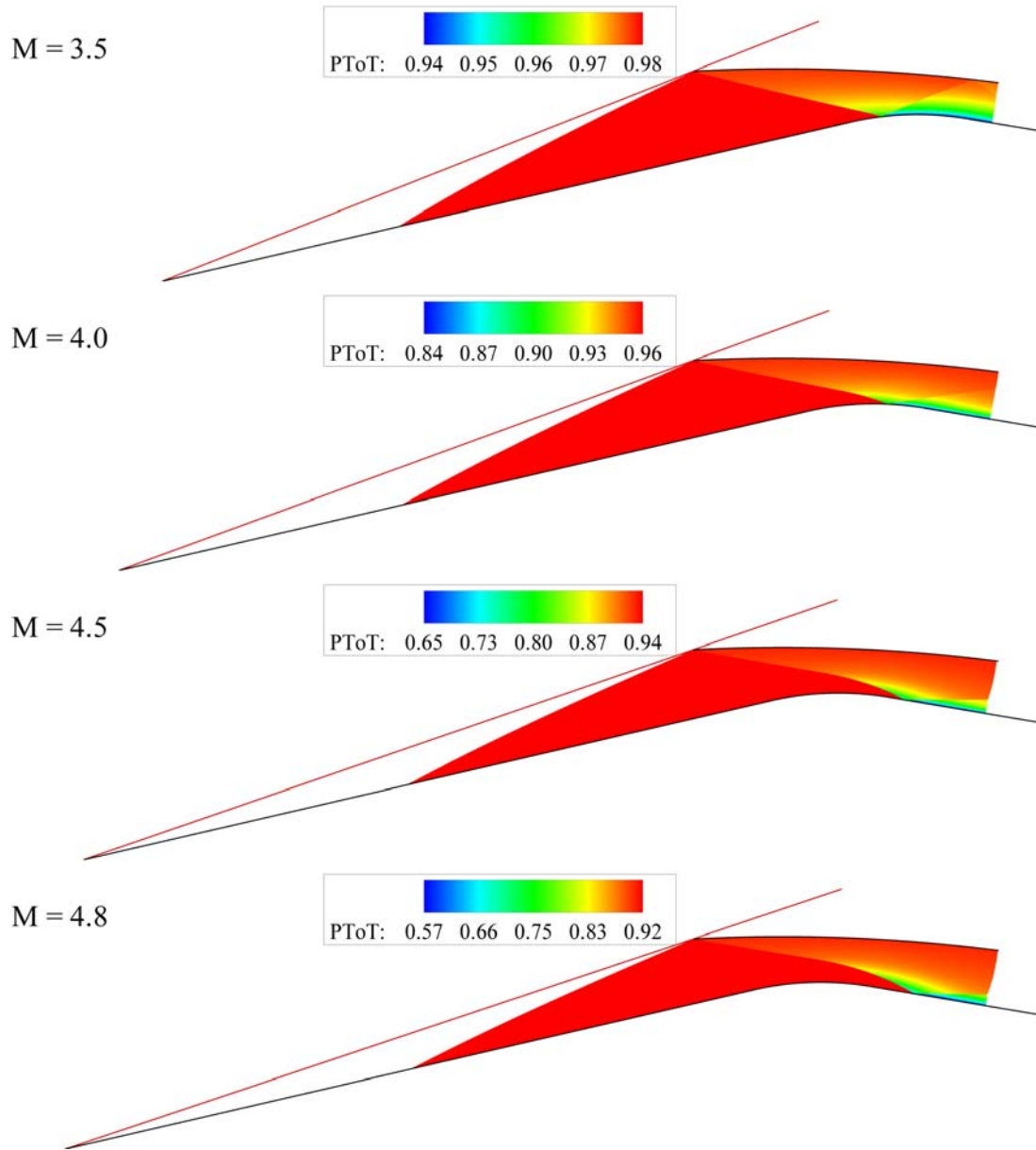


Figure 5.3 Re-extended Spike Inlet Total Pressure Ratio Contours

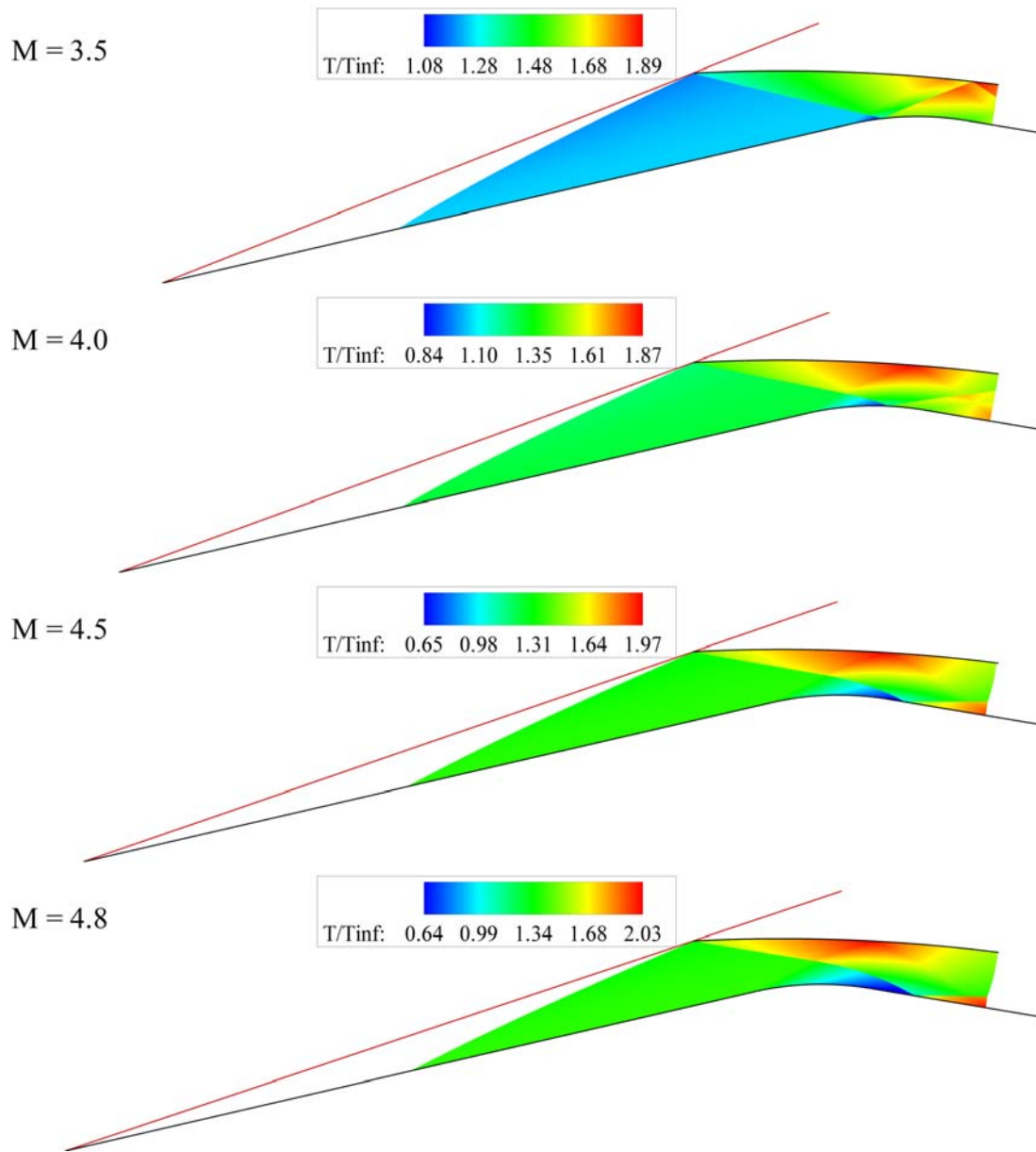


Figure 5.4 Re-extended Spike Inlet Temperature Ratio Contours

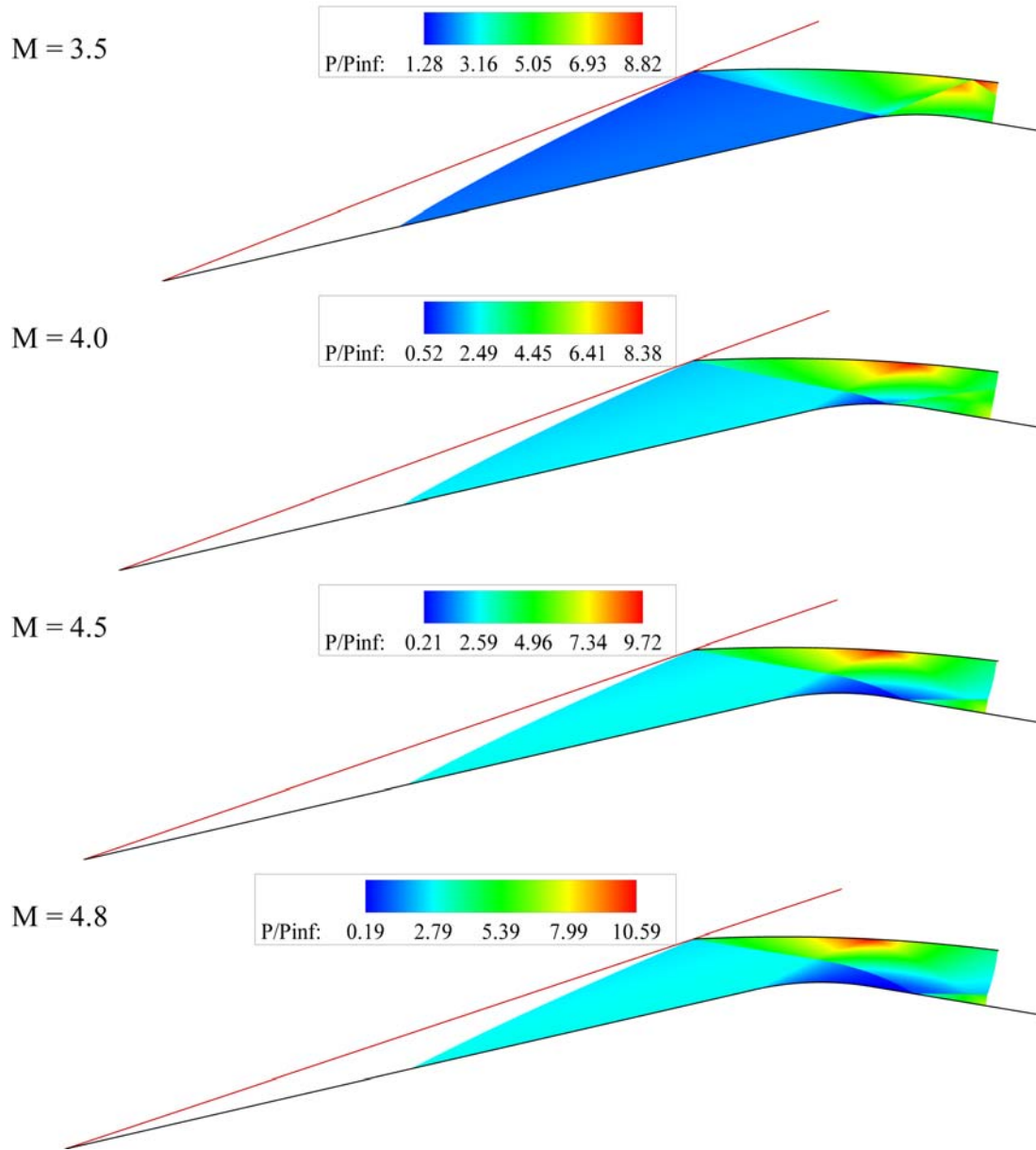


Figure 5.5 Re-extended Spike Inlet Pressure Ratio Contours

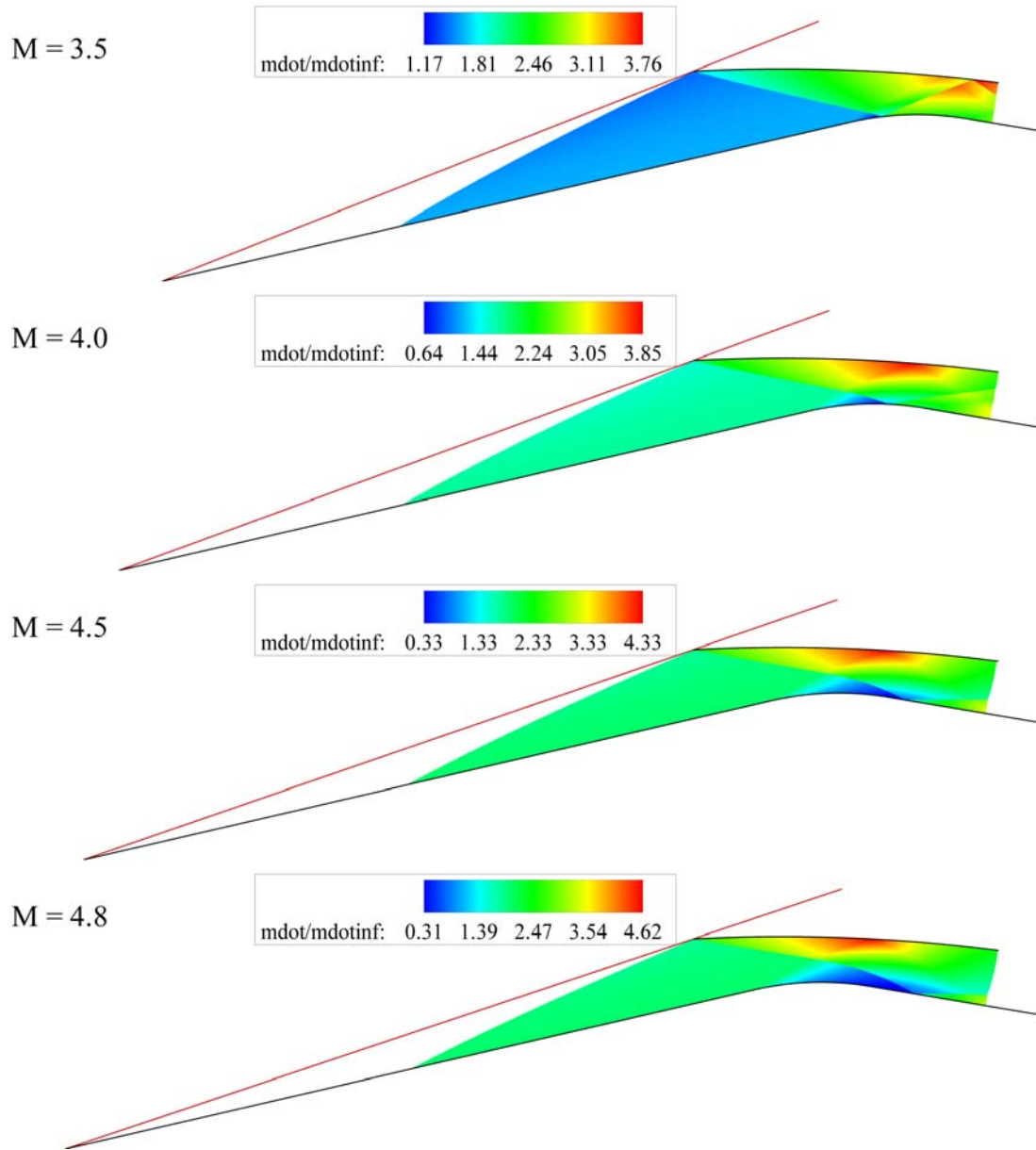


Figure 5.6 Re-extended Spike Inlet Mass Flow Ratio Contours

### 5.1.3 Throat Conditions

Gas properties at the throat for the re-extended spike are shown in Figures 5.7 and 5.8. Because of the limited number of shock reflections, the effective entry Mach number remains one less than the flight Mach number for the entire flight regime.

Entry total pressure losses are small (the total pressure ratio remains above 0.86 at Mach 4.8), mostly because of the small number of shock reflections. Entry temperature, pressure and mass flow ratios decrease to about 1.6, 4 and 2.3, respectively, as the inlet is oversped. However, all flow properties appear to be highly distorted (the pressure and mass flow distortion levels are at 140 and 75 percent at Mach 4.8, respectively). This is expected because of the large curvature in the first reflected shockwave.

The Mach number at the throat exit is rather low, beginning below Mach 0.6 and ending at  $\sim 0.45$  (which is good for ramjet operation) but because the entry Mach numbers are high, the total pressure losses are substantial (the total pressure ratio is  $\sim 0.7$  at Mach 3.3 and falls to  $\sim 0.2$  at Mach 4.8). Exit pressure and temperature ratios are also large because of the high entry Mach numbers (the temperature and pressure ratios are  $\sim 5.7$  and  $\sim 55$  at Mach 4.8, respectively). The distortion levels for Mach number and temperature ratio are acceptable (remaining below 10 percent for the entire regime), but the levels of distortion for total pressure, static pressure and mass flow ratio are all still very high (above 50 percent for most of the regime) at the higher speeds.

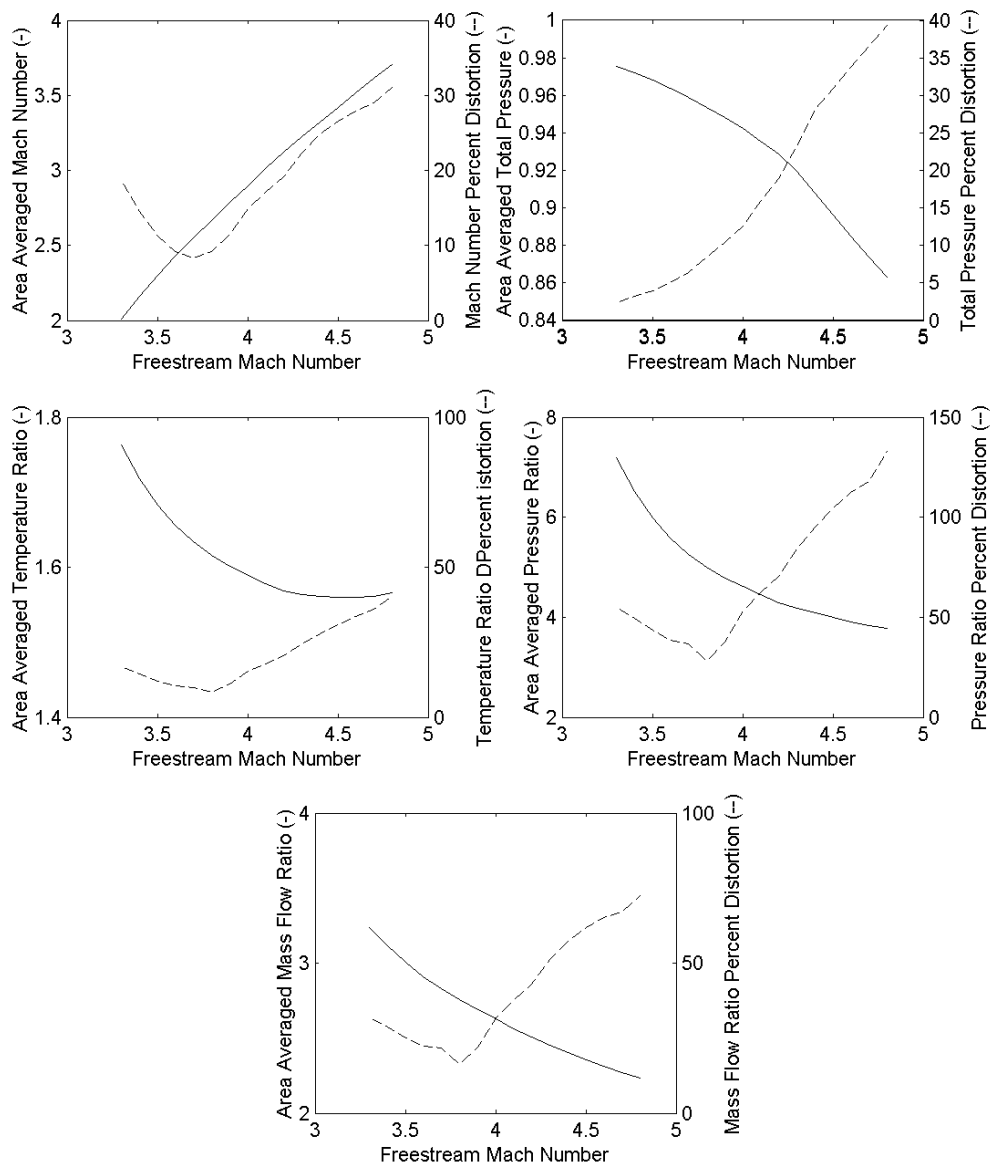


Figure 5.7 Supersonic Re-extended Spike Throat Properties

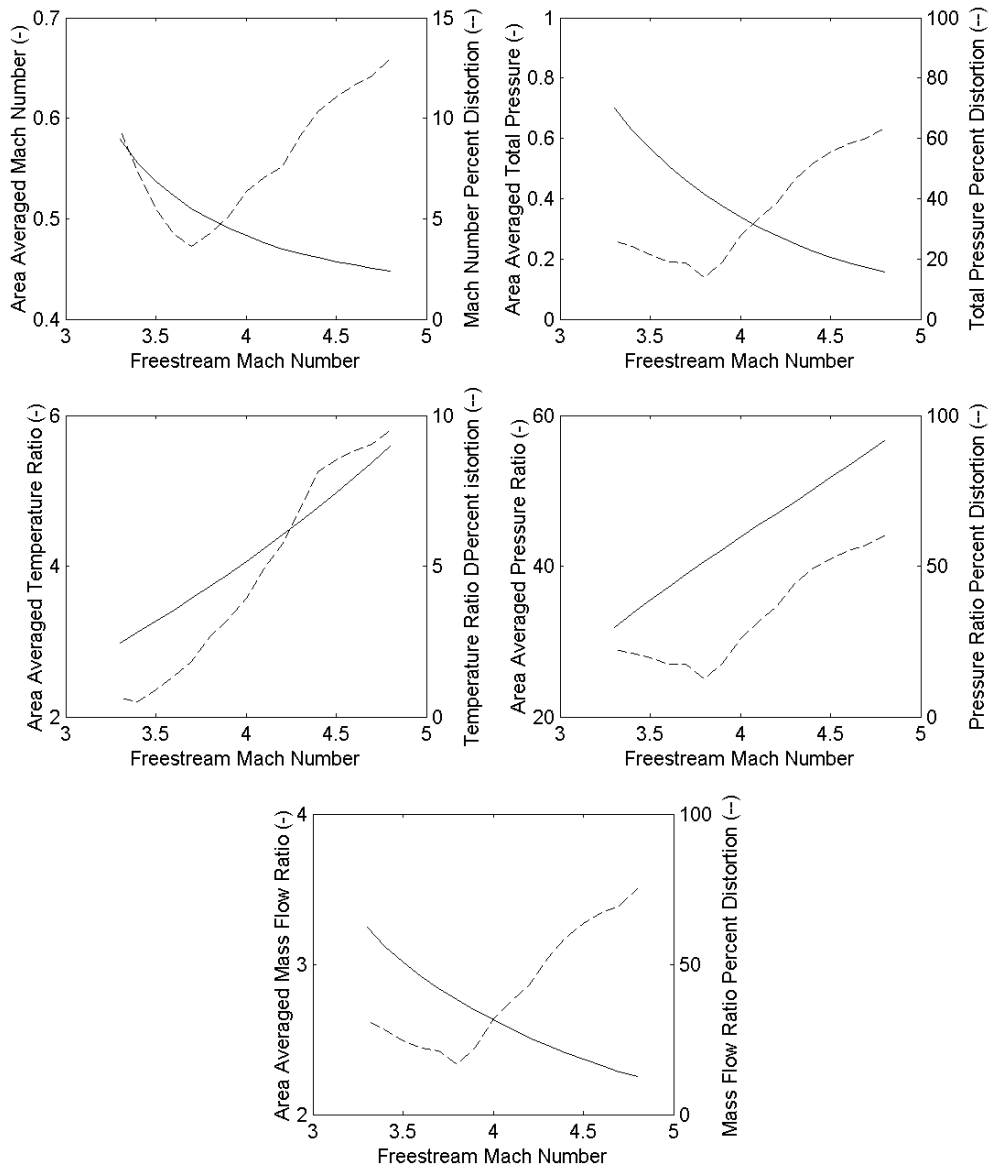


Figure 5.8 Subsonic Re-extended Spike Throat Properties

## 5.2 Variable Cowl Leading Edge

The second proposed redesign scheme involves allowing the radial portion of the cowl leading edge to vary while keeping the spike in its aft most position. This would enable the leading edge of the cowl to be aligned with the conical shock (as is shown in Figure 5.9) at every oversped Mach number. The dashed lines shown (starting from top to bottom) illustrate the cowl position at Mach numbers of 3.3, 3.6, 3.9 and 4.2, respectively.

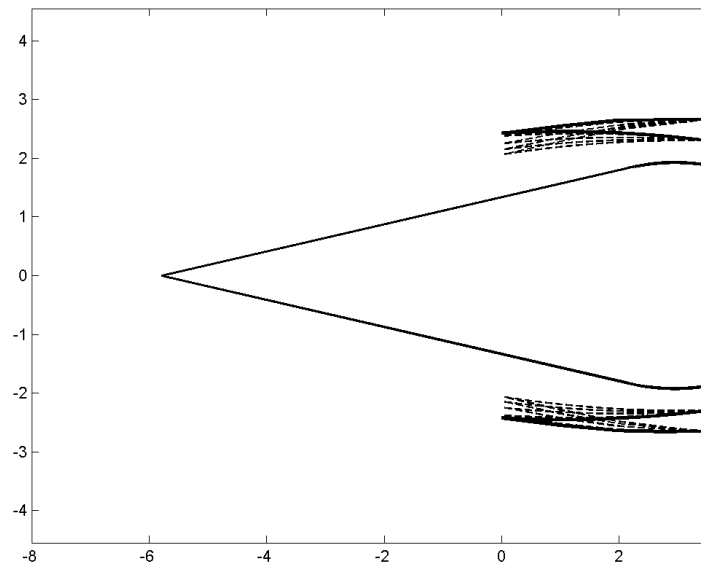


Figure 5.9 Diagram of the Variable Cowl Leading Edge

### 5.2.1 Self-Starting Characteristics

The resulting self-starting characteristics are shown in Figure 5.10. As the figure shows, the self-starting performance is poorer than the previous redesign (the inlet would unstart at about Mach 4). This occurs because of the rapid change in the

area ratio, caused by the decrease in the cowl area. This design would also introduce a large penalty in added cowl drag. Because of the poor self-starting characteristics, full flow analysis of this redesign scheme was not completed.

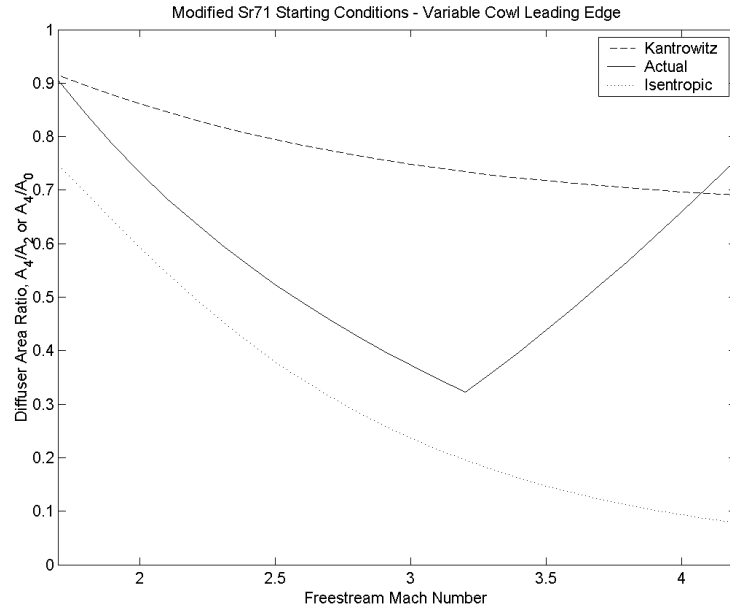


Figure 5.10 Self-Starting Characteristics of the Variable Cowl Leading Edge

### 5.3 Re-extension with a Widened Shoulder

The major problem with both of the previous redesign schemes is the high rate at which the cowl/throat area ratio increases as the inlet is oversped. One way to alleviate this problem is to fix the throat area while re-extending the centerbody. In order to perform this operation, the shoulder on the centerbody spike would need to have the ability to widen as shown in Figure 5.11. The dashed lines (going from right to left) in the figure represent the centerbody geometry at Mach numbers of 4, 5 and 6.1, respectively.

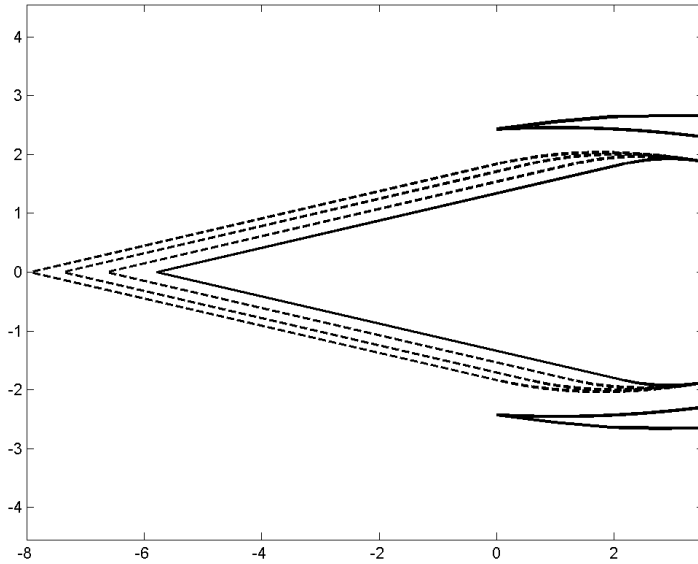


Figure 5.11 Diagram of the Re-extension with a Widened Shoulder

### 5.3.1 Self-Starting Characteristics

The self-starting characteristics of the widened shoulder centerbody are shown in Figure 5.12. The figure shows a marked improvement in the starting performance. The curve still shows a sharp discontinuity but it also demonstrates that the inlet has the ability to maintain starting capability up until the maximum oversped Mach number of 6.1 discussed in Section 5.1. The inlet is mechanically limited by the re-extension constraint imposed on the problem. If the inlet were allowed to re-extend beyond the original low speed location of the SR-71 inlet, it would be able to remain self-started past Mach 6.1.

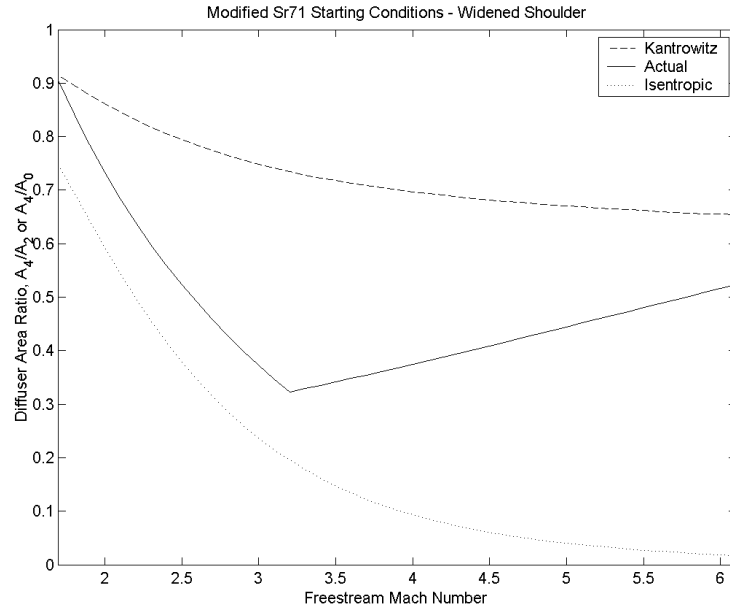


Figure 5.12 Self-Starting Characteristics of the Widened Shoulder Centerbody

### 5.3.2 Flowfield Properties

Property contours are presented in Figures 5.13 through 5.17 for the widened shoulder centerbody. The general trend is similar to that of the re-extended spike except that the widened shoulder slows the progression of the initial reflected cowl shock onto the shoulder. Unlike the re-extended spike, the reflected shock never moves completely over the shoulder. However, both systems result in only a 2 shock internal reflection system. Local regions of high temperature and pressure (the temperature and pressure ratios rise to 2.4 and 15.24, respectively) are again apparent on the cowl prior to being affected by the expansion waves. Since the initial reflected cowl shock is not as curved for the widened shoulder centerbody, the gradients in the flow properties are not as severe as they are with the simple re-extended spike.

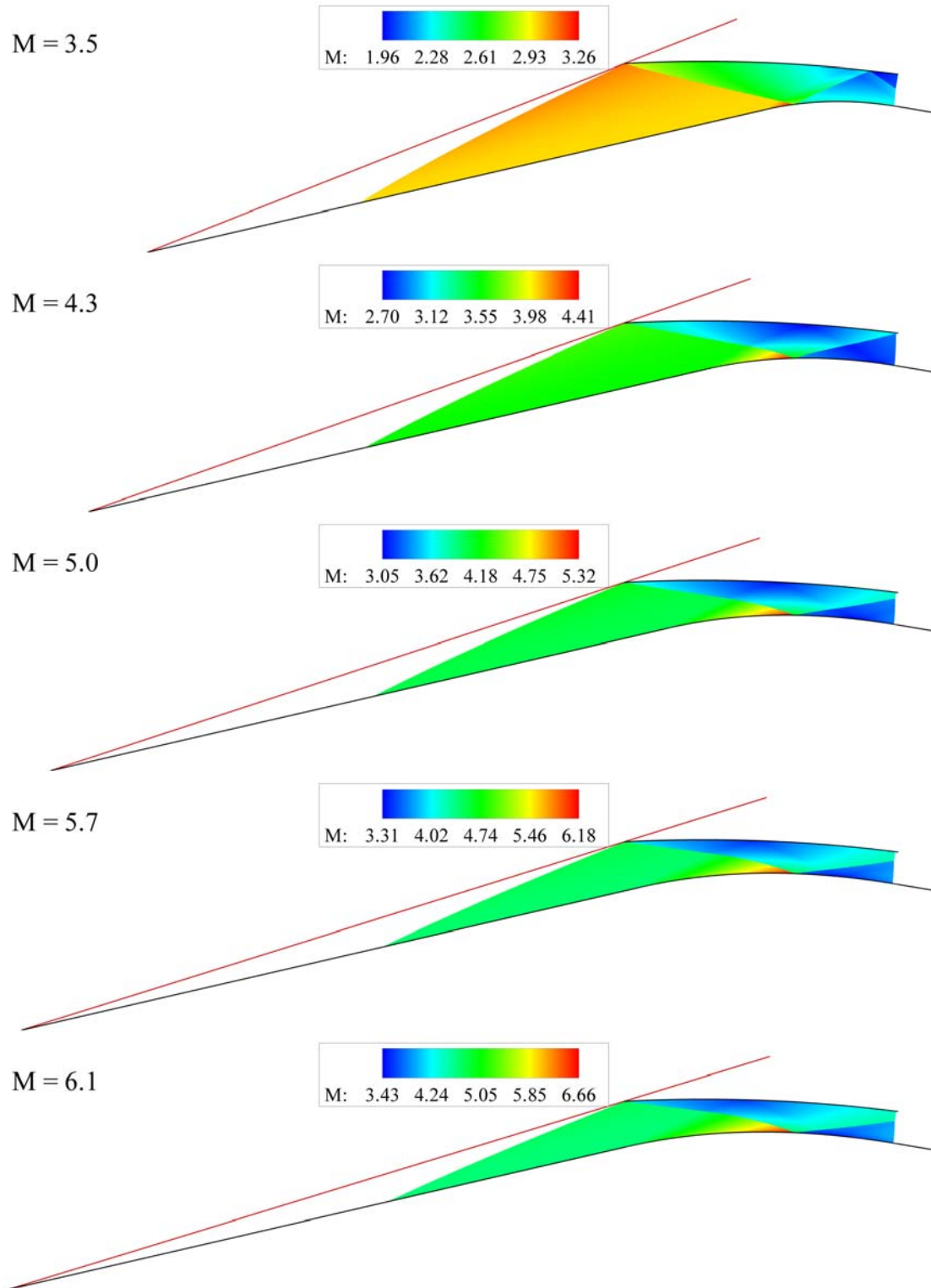


Figure 5.13 Widened Shoulder Centerbody Inlet Mach Number Contours

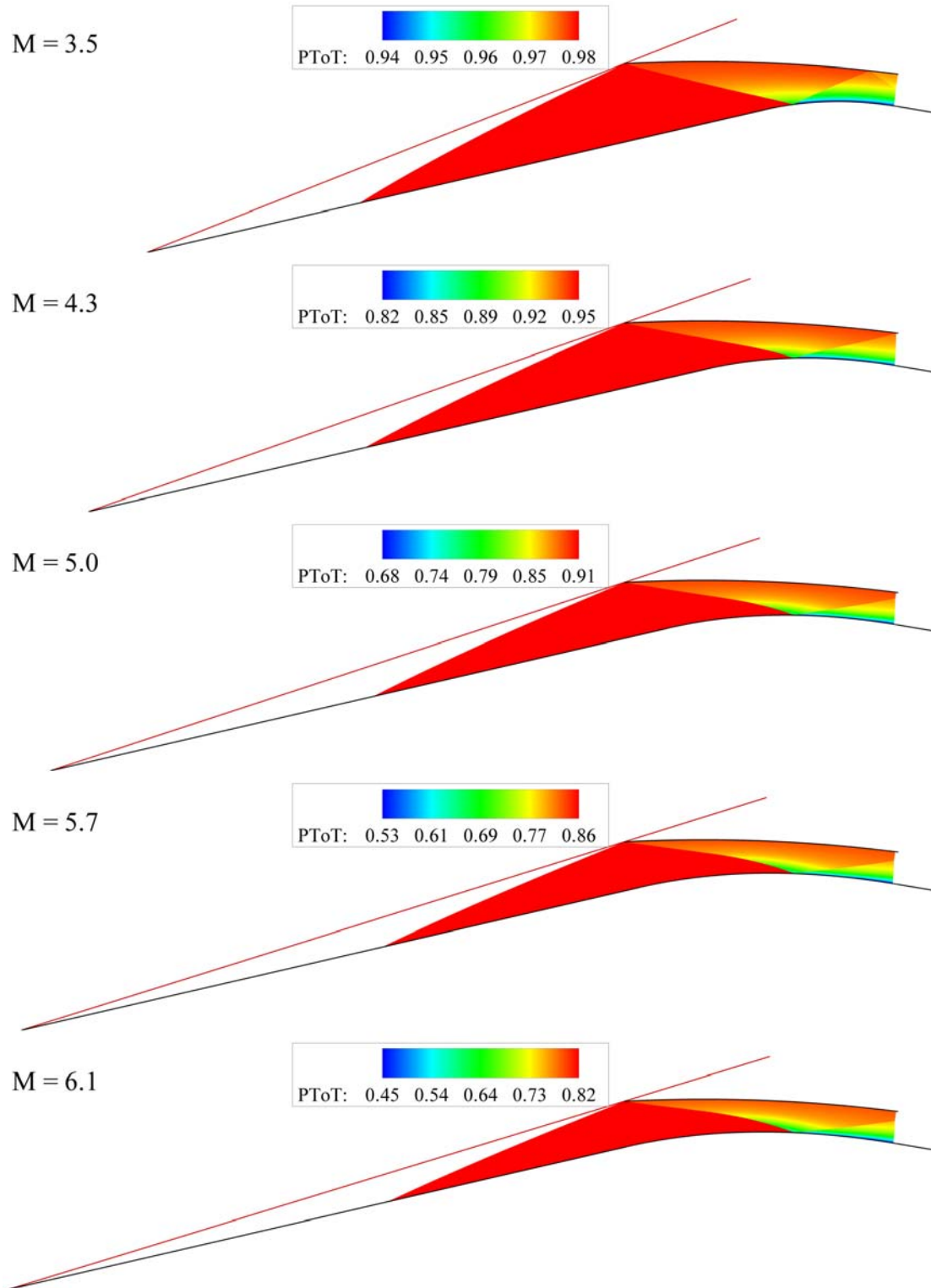


Figure 5.14 Widened Shoulder Centerbody Inlet Total Pressure Ratio Contours

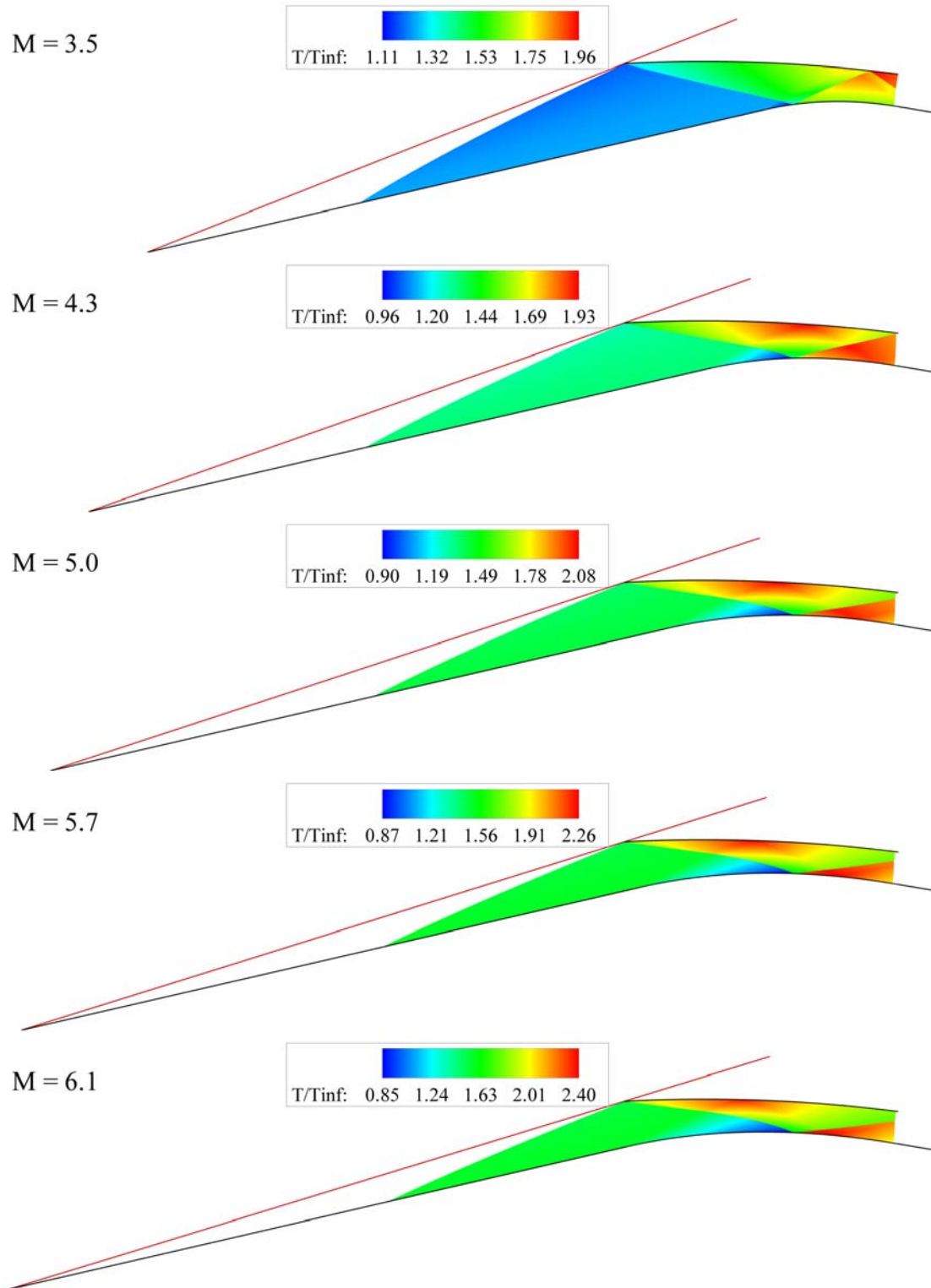


Figure 5.15 Widened Shoulder Centerbody Inlet Temperature Ratio Contours

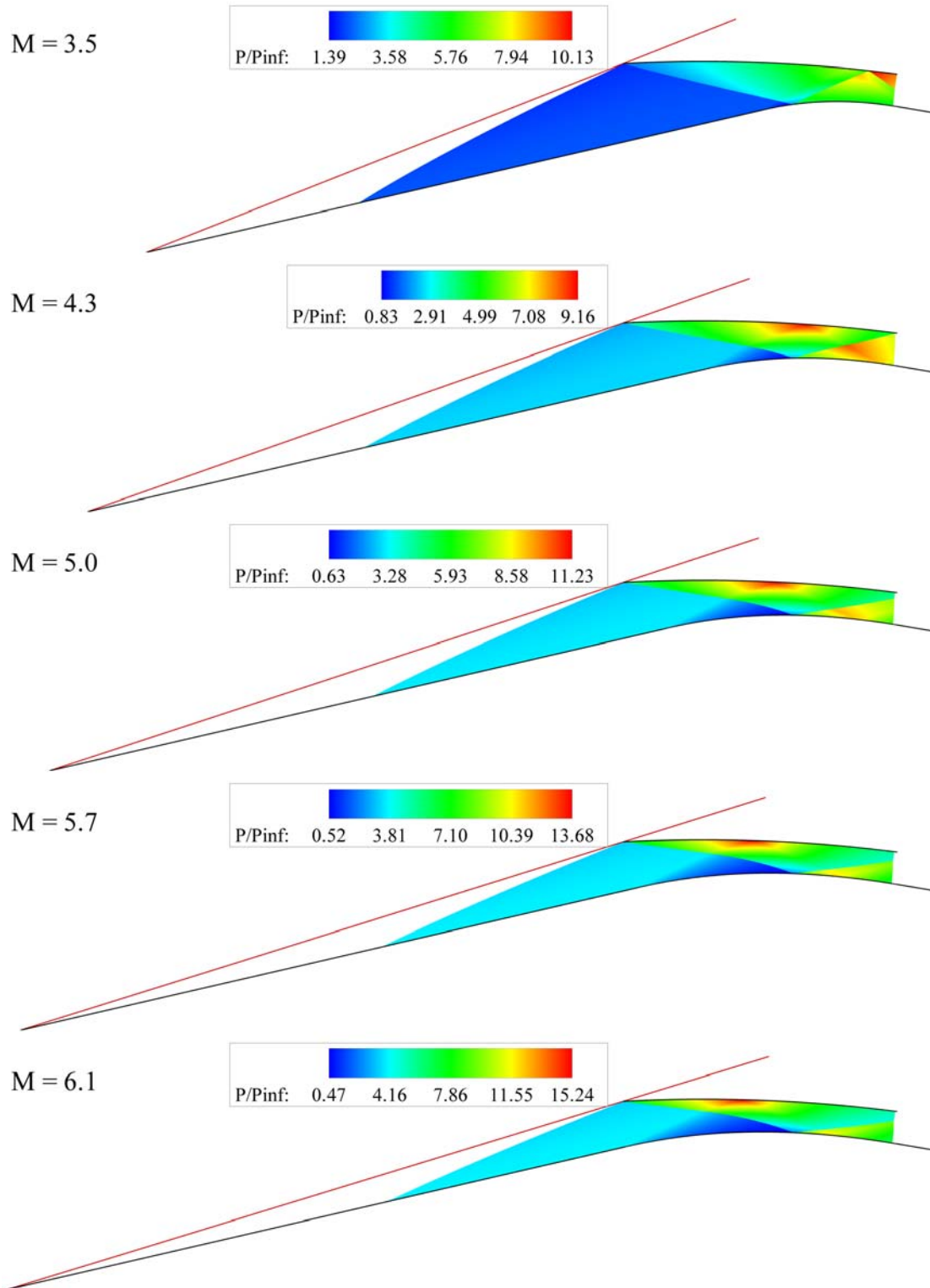


Figure 5.16 Widened Shoulder Centerbody Inlet Pressure Ratio Contours

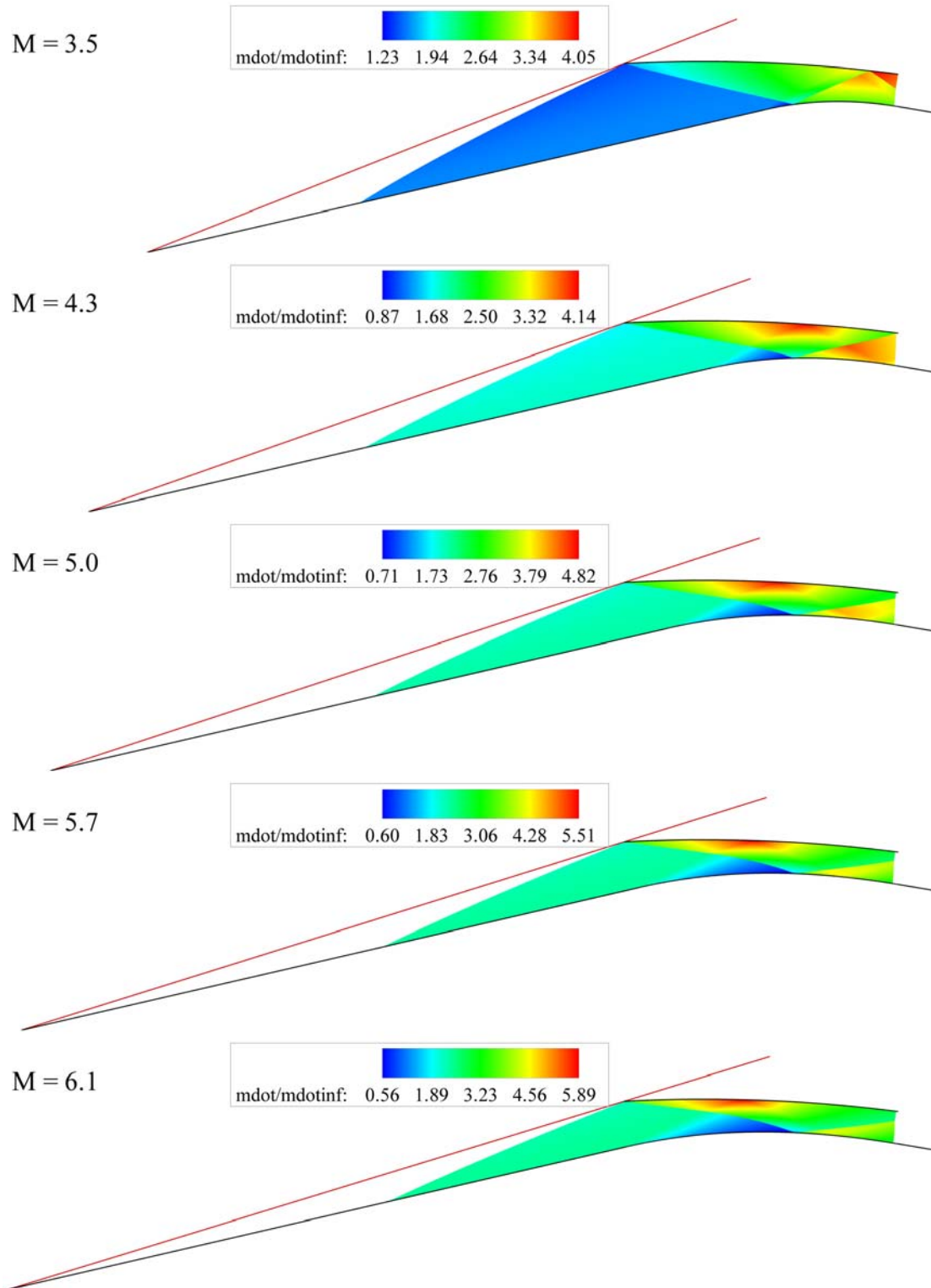


Figure 5.17 Widened Shoulder Centerbody Inlet Mass Flow Ratio Contours

### 5.3.3 Throat Conditions

The throat entrance and exit properties shown in Figures 5.18 and 5.19 show a marked improvement in the flow quality over the re-extended spike. The supersonic plots reveal that at similar speeds, the Mach number entering the throat is lower, the temperature and pressure are higher, and the distortion levels are much lower for four of the flow properties. The total pressure ratio is about the same entering the throat at similar speeds. The mass flow ratio similarly decreases from 3.37 at Mach 3.3 to 3.32 at Mach 6.1, but the change is sufficiently small such that the mass flow ratio is essentially constant. The plots also show that the temperature ratio starts at about 1.8, decreases to about 1.75 near Mach 4, and then increases with a final ratio of about 2 at Mach 6.1. Similarly, the pressure ratio starts at about 7.7, and then decreases to about 6.7 near Mach 4.5 and then increases with a final ratio of about 7 near Mach 6.1.

The subsonic plots also show that performance is better overall. Total pressure ratio (starting at about 0.75 and ending below 0.2), Mach number (starting at about 0.59 and ending near 0.43) and pressure ratio (starting at 30 and ending at about 140), for any given Mach number, are higher than the re-extended spike with slightly lower distortion levels. The temperature ratio (starting at about 3 and ending at about 8), interestingly, is essentially equal, albeit with differing levels of distortion. In all likelihood, transition to scramjet would occur somewhere along the flight path because of the large increases in pressure ratio and the considerable losses in total pressure as the flight speed is increased.

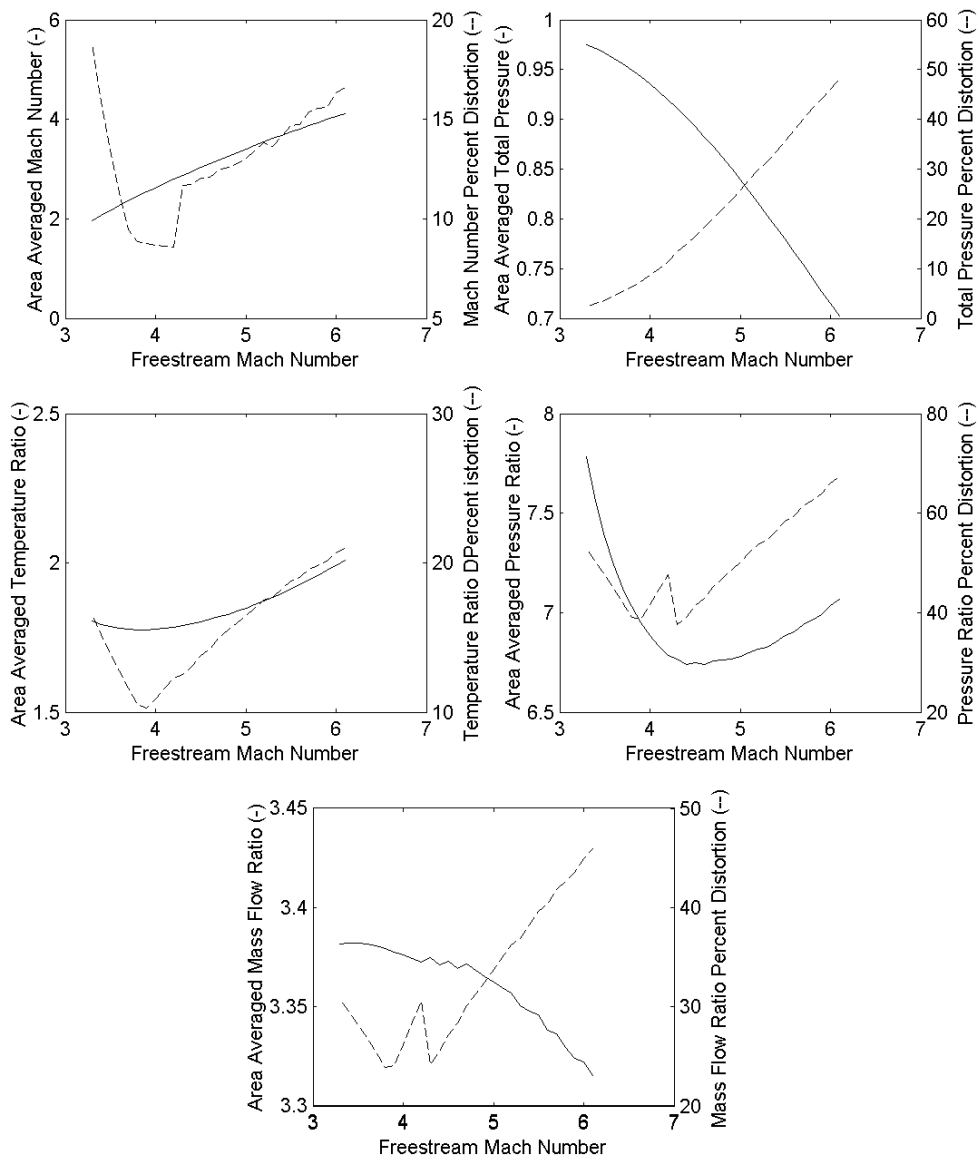


Figure 5.18 Supersonic Widened Shoulder Centerbody Throat Properties

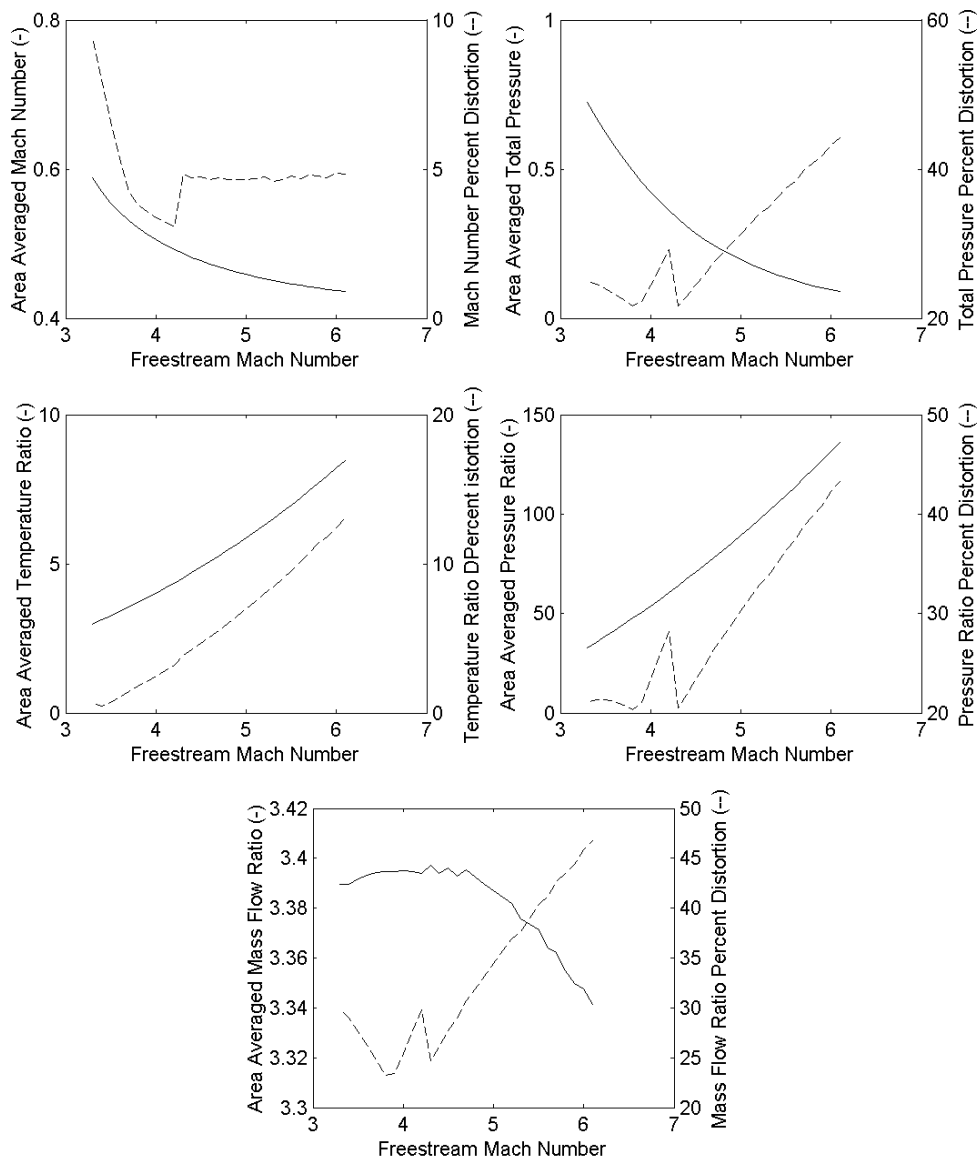


Figure 5.19 Subsonic Widened Shoulder Centerbody Throat Properties

## 5.4 Variable Cone Centerbody

Yet another option would be to install a variable cone on the centerbody spike. In this scenario, the spike would remain fixed its axial location at Mach 3.2 and then increase its conical half angle to maintain the shock-on-lip condition. However, this design has major limitations (beyond the obvious mechanical complexity) as shown in Figure 5.20. The dashed lines in the figure are the change in the centerbody geometry needed to maintain the shock-on-lip condition at freestream Mach numbers of 3.3, 3.4, 3.5, 3.6 and 3.7. As the figure illustrates, the variable centerbody can only be enlarged up to an angle of about  $15^\circ$  (corresponding to a freestream Mach number of 3.7) before the throat would be completely closed. [Note this design still assumes a cubic spline shoulder.]

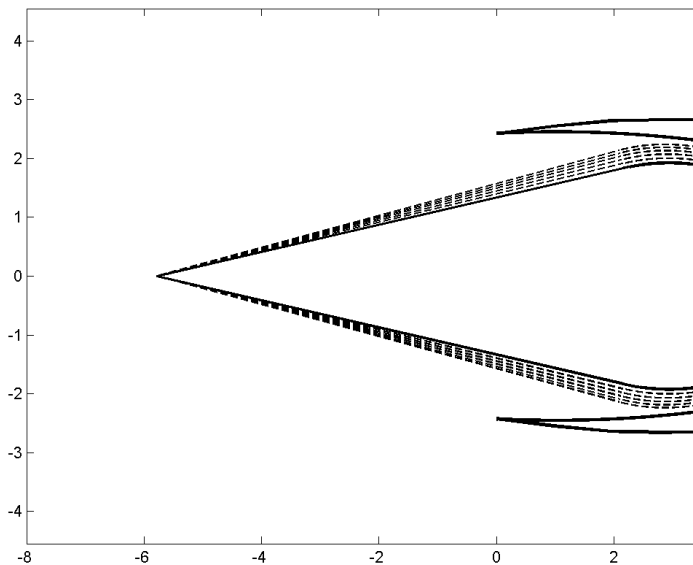


Figure 5.20 Variable Cone Centerbody Diagram

### 5.4.1 Self-Starting Characteristics

Besides the obvious physical problems with this inlet modification, Figure 5.21 shows that the self-starting characteristics of this inlet are very poor. The inlet would violate the maximum isentropic contraction ratio limit (due to the decrease in throat area) before it penetrates the outer cowl. As with the variable cowl leading edge design, this inlet was not fully analyzed due to its poor starting performance.

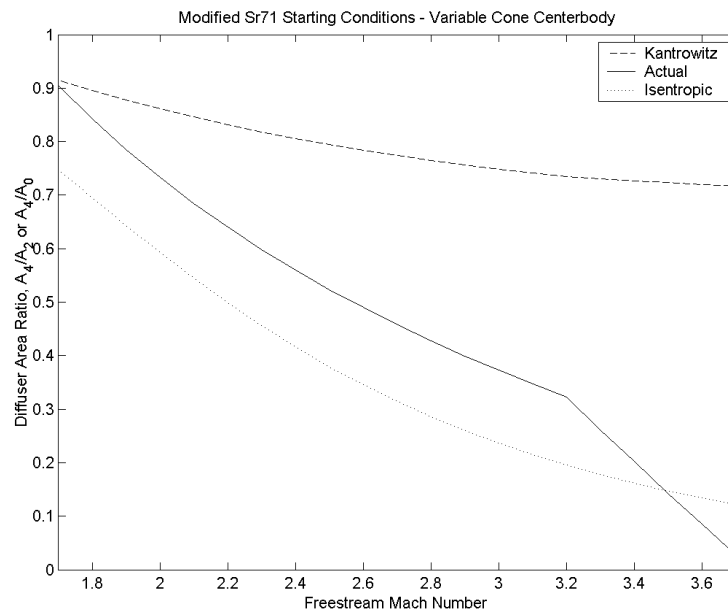


Figure 5.21 Self-Starting Characteristics of the Variable Cone Centerbody

### 5.5 Variable Cone Centerbody with Re-extension

The inlet shown in Figure 5.22 can be constructed by combining the variable cone and re-extension aspects. In this situation, as the spike is pushed forward the cone expands to maintain the shock-on-lip requirement (a highly non-linear solution). In the current design, the throat area remained fixed as well. Theoretically, this inlet

could maintain the shock-on-lip condition for any freestream Mach number (the maximum cone angle needed would only be about  $16^\circ$ ) before reaching the re-extension limit. The dashed lines correspond to the centerbody geometry (starting from right to left) at Mach numbers of about 3.5, 4, 5.25 and 8.25, respectively.

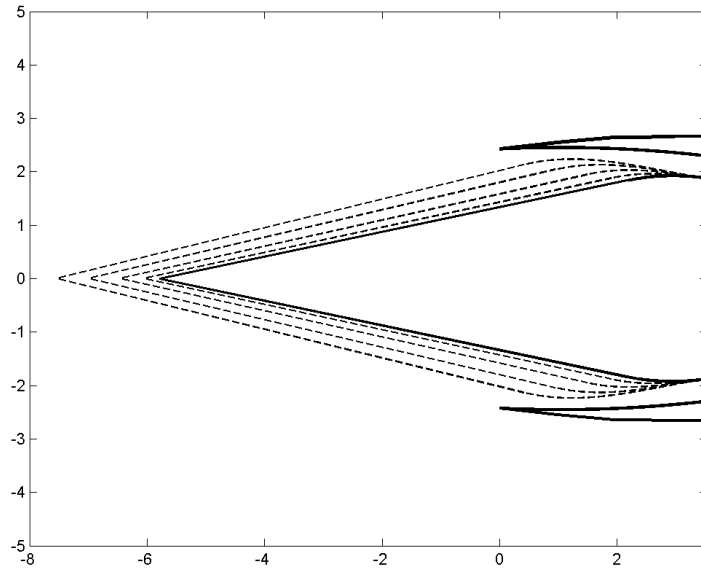


Figure 5.22 Variable Cone Centerbody with Re-extension diagram

### 5.5.1 Self-Starting Characteristics

While the variable cone with re-extension inlet could be oversped to any freestream Mach number and remain within the geometrical constraints, it would violate the Kantrowitz limit at about Mach 7.2 (Figure 5.23). Again, this occurs because of the change in throat/cowl area ratio. However, while it will not be considered in the current report, the starting performance would likely improve if the constant throat area constraint were relaxed.

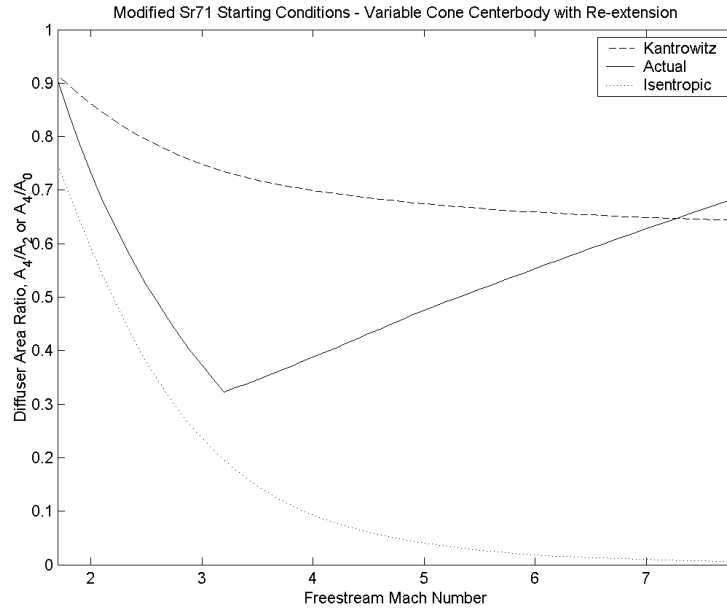


Figure 5.23 Self-Starting Characteristics of the Variable Cone with Re-extension

### 5.5.2 Flowfield Properties

Contours for the variable cone with re-extension modification scheme are shown in Figures 5.24 through 5.28. The new conical half angle is indicated on each figure. Again, the basic structures of the flowfields are very similar to that of the widened shoulder and the re-extended spike schemes. However, as the plots demonstrate, the advancement of the impingement location of initial reflected cowl shock is slower than that of the widened shoulder thus delaying the pre-reflection expansion. Accordingly, the impingement locations of the both the initial cowl reflected shock and the centerbody reflection appear to be constant from about Mach 5.5 through Mach 7.2. The temperature and pressure ratio plots show a rather complex flow structure as the expansion waves propagate through the system creating

multiple regions of high and low temperature and pressure. The major difference between this scheme and the two previously analyzed is that this design maintains the 3 reflected shock system throughout the flight profile.

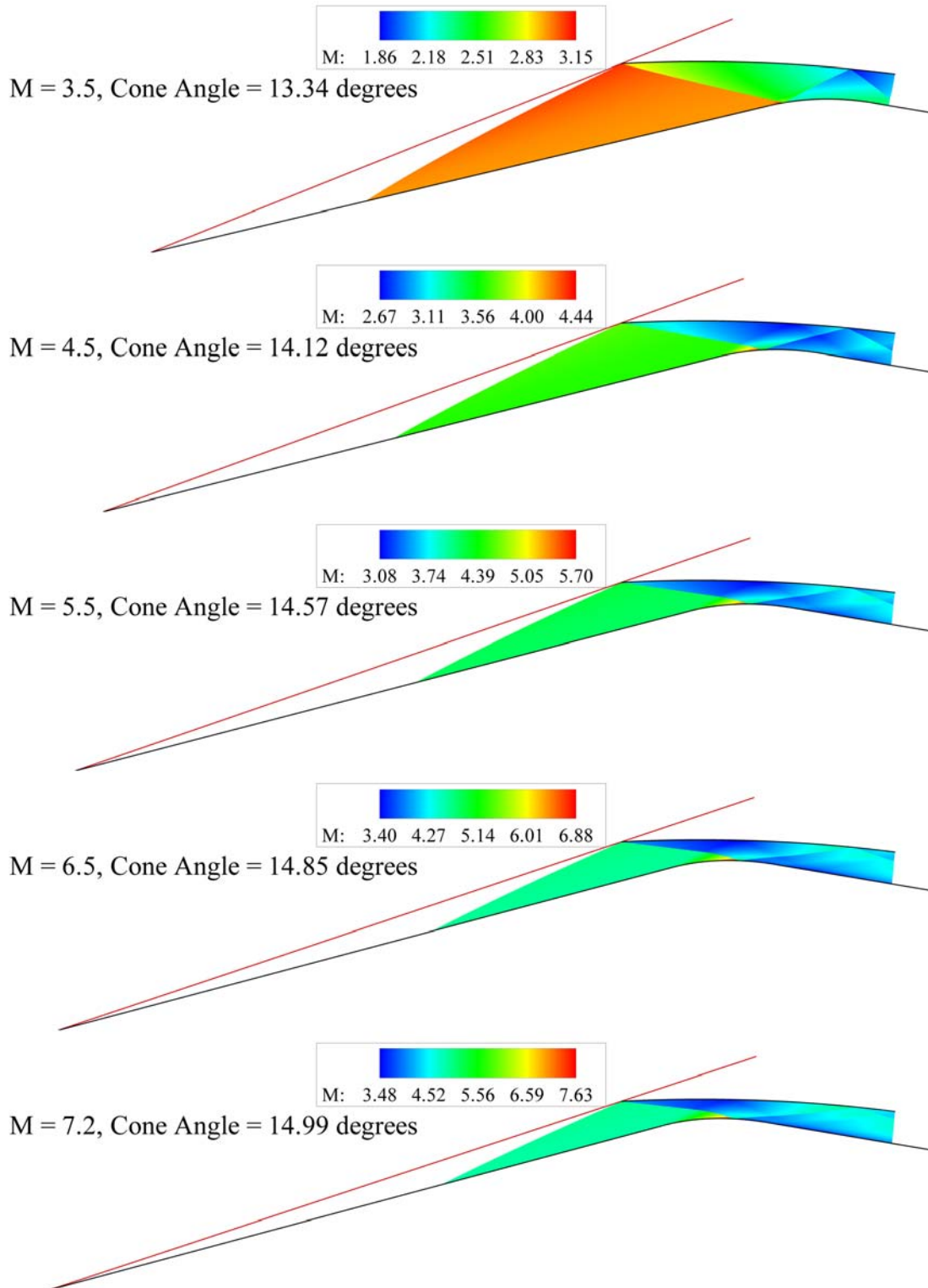


Figure 5.24 Variable Cone with Re-extension Inlet Mach Number Contours

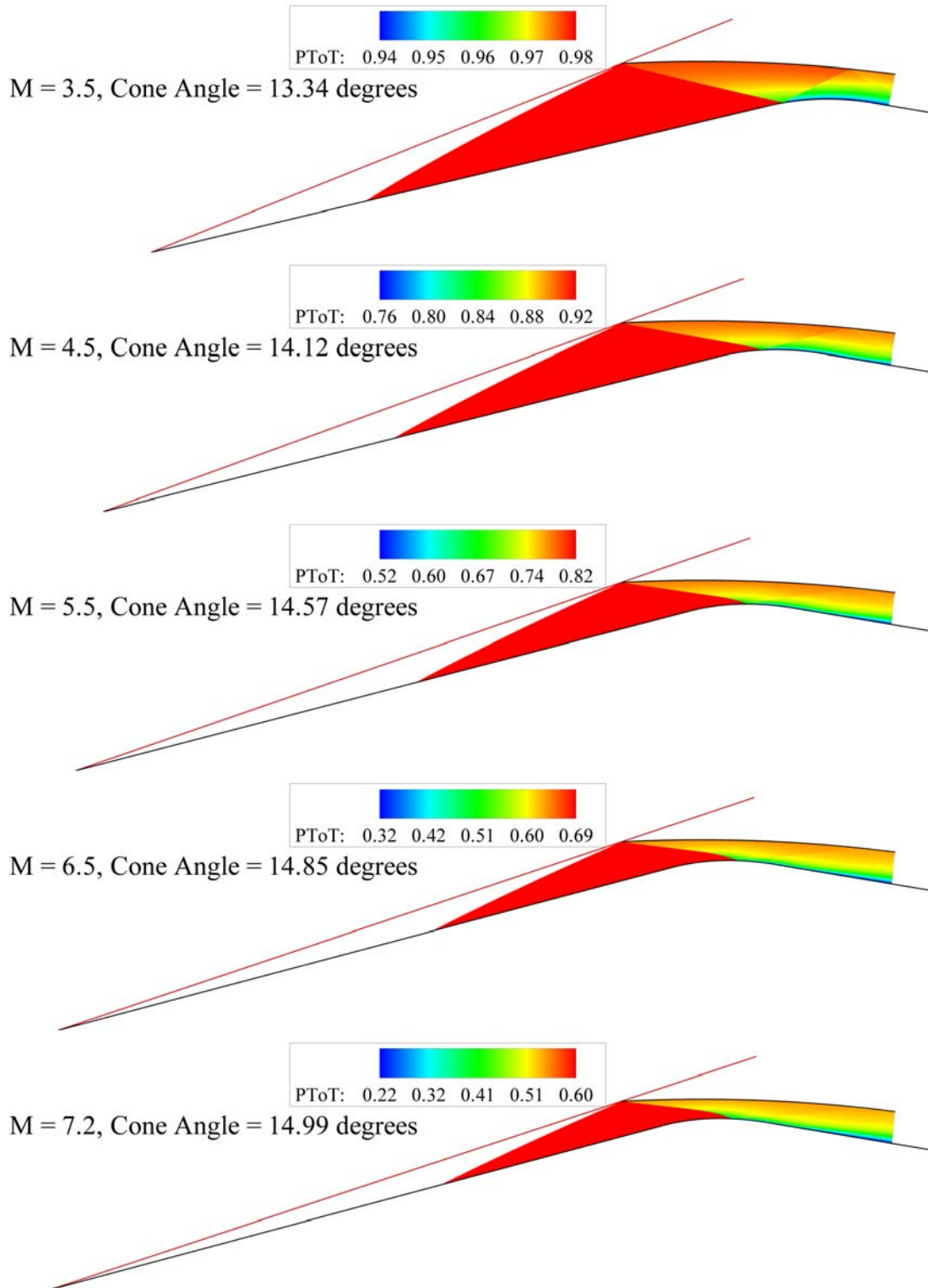


Figure 5.25 Variable Cone with Re-extension Inlet Total Pressure Ratio Contours

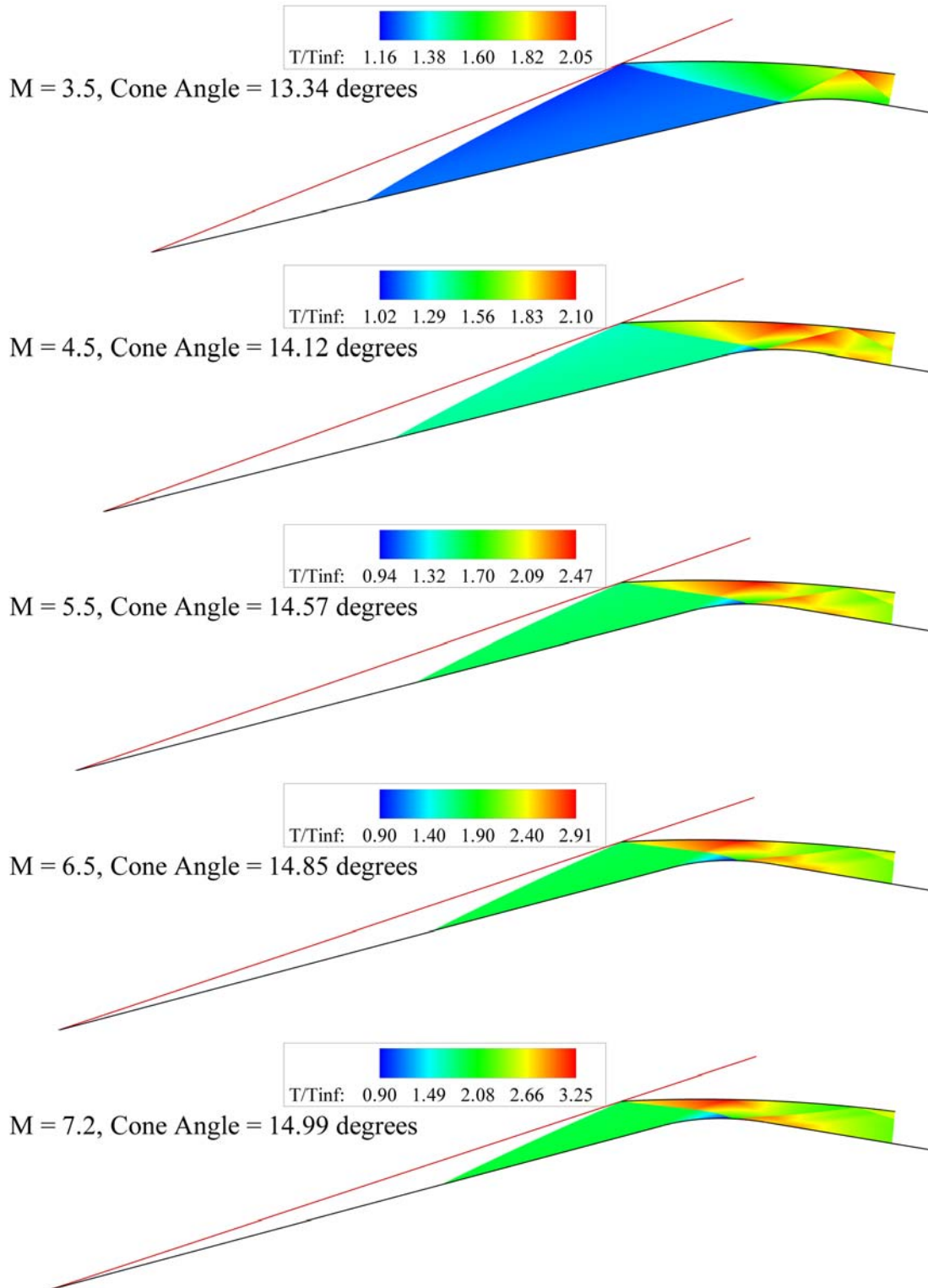


Figure 5.26 Variable Cone with Re-extension Inlet Temperature Ratio Contours

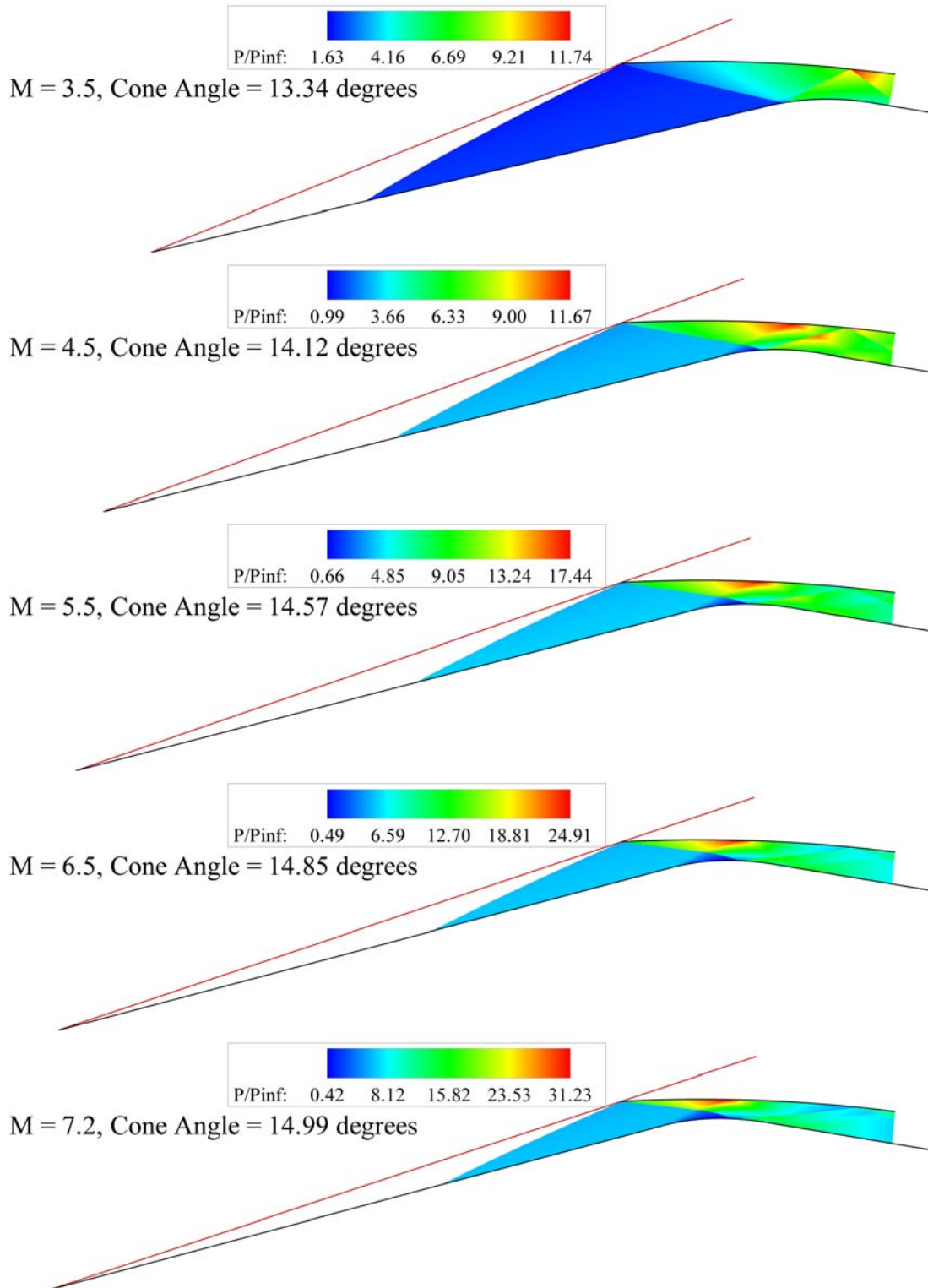


Figure 5.27 Variable Cone with Re-extension Inlet Pressure Ratio Contours

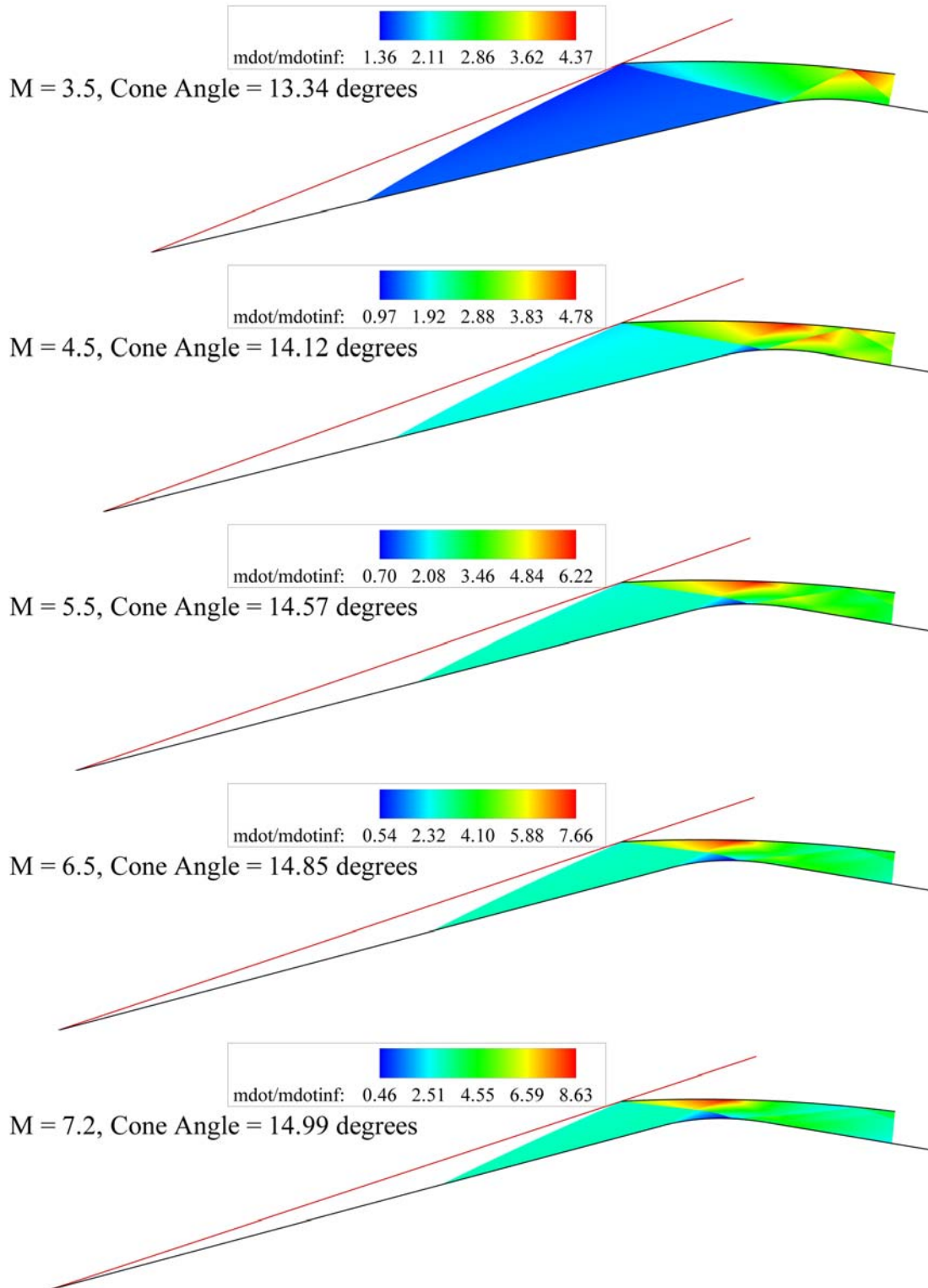


Figure 5.28 Variable Cone with Re-extension Inlet Mass Flow Ratio Contours

### 5.5.3 Throat Conditions

The throat entrance and exit conditions are shown in Figures 5.29 and 5.30, respectively. For similar flight speeds, the entrance Mach number for the variable cone with re-extension scheme is essentially the same as that of the widened shoulder. Likewise, the temperature and pressure ratio entrance properties are similar, but the total pressure ratio is lower. This makes sense because in this case the flow passes through two stronger shockwaves and an additional reflected shock. Overall, the distortion levels are slightly lower compared to the widened shoulder centerbody. Mass flow decreases as well from 3.39 at Mach 3.3 to about 3.2 at Mach 7.2, but as with the widened shoulder, is essentially constant.

The subsonic features of the variable cone with re-extension inlet show equivalent trends with the widened shoulder centerbody. The exit Mach number starts at about Mach 0.6 and finishes at about Mach 0.43. The total pressure ratio is effectively the same, starting at about 0.7 and ending below 0.1. The exit temperature and pressure ratios are fairly consistent; however, the distortion levels are moderately better for the variable cone with re-extension inlet.

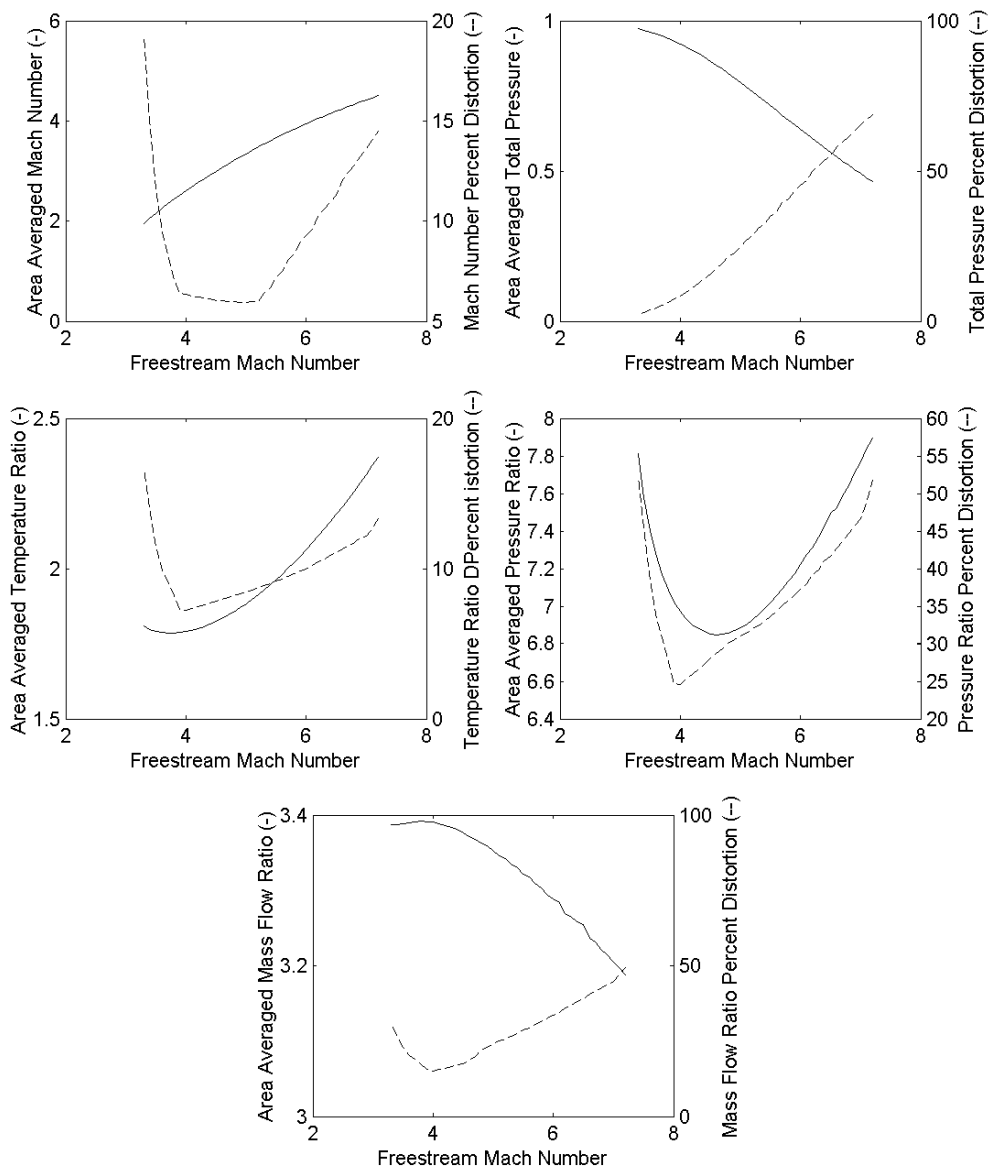


Figure 5.29 Supersonic Variable Cone with Re-extension Throat Properties

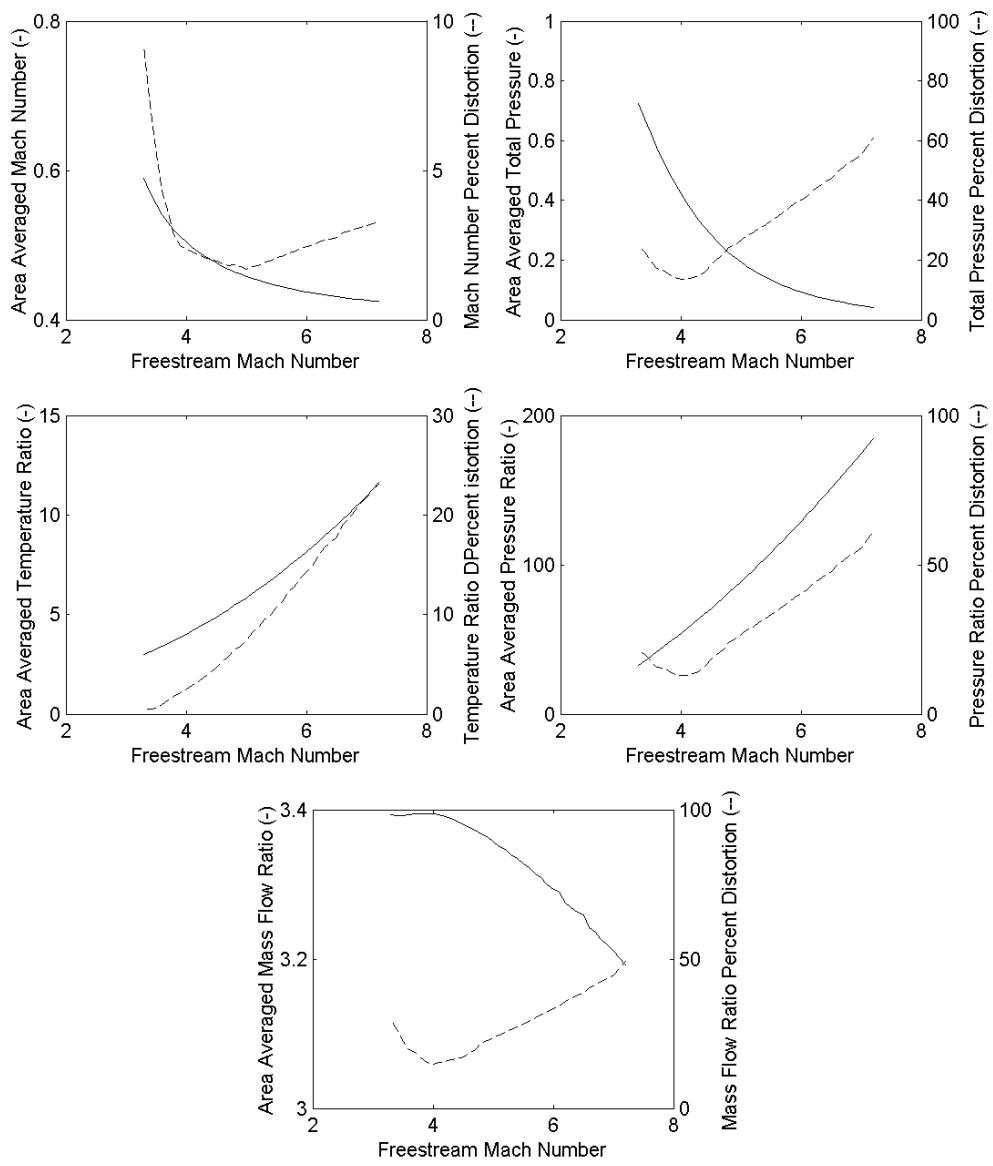


Figure 5.30 Subsonic Variable Cone with Re-extension Throat Properties

## 6 Summary and Conclusions

This thesis developed a new strategy for designing inlets for turbine-based combined-cycle engines. Rather than starting the design process with a clean slate, the performance of a specific supersonic inlet was analyzed and certain aspects of the inlet were redesigned to see if the flight envelope could be pushed into the hypersonic flight regime. A numerical model was developed using the axisymmetric method of characteristics that is capable of calculating the supersonic, inviscid flow properties of axisymmetric inlets. This results from the model were used to quantify important properties of the flowfield (Mach number, total pressure ratio, temperature ratio, pressure ratio and mass flow ratio), and their levels of distortion (spatial non-uniformity), at the throat entrance. A simple lambda shock structure was then used to approximate the flow properties leaving the throat. The Kantrowitz limit was computed to estimate the self-starting limit of the inlets.

Several candidate inlets were examined initially, including those used on the Boeing XB-70, Lockheed D-21 Drone, and the Concorde. However, this work focused on Lockheed SR-71 inlet. The J-58D engines that powered the SR-71 effectively operated as a ramjet at the higher speeds since a good deal of the airflow

bypassed the combustor and turbine and was dumped straight into the afterburner. The SR-71 inlet was chosen because of the TBCC-like qualities of the J-58D engine. The inlet of the SR-71 is a mixed compression inlet that starts at Mach 1.7 and can be run up to Mach 3.2. The inlet utilizes a translating spike and a series of bleeds and bypasses to control the position of the terminating normal shock and to regulate the amount of airflow passing through the engine.

Investigation of the SR-71 inlet proved that the inlet indeed satisfies the Kantrowitz limit at Mach 1.7 and maintains the self-starting capability through Mach 3.2. The characteristics model showed that at the low Mach numbers several reflected shock waves are present within the duct. As the inlet speeds up, the shock train propagates through the duct so that at the design Mach number of 3.2, only two internal reflections are present. The inlet performed rather well, losing less than three percent of total pressure (with very low levels of distortion) prior to entering the throat. Downstream of the throat, the total pressure losses stayed above about 23 percent and the Mach number remained nearly constant, varying from 0.66 to 0.62 at flight speeds between Mach 1.7 and 3.2. Pressure, temperature, and mass flow ratios gradually rose at the exit plane as the Mach number was increased. A final pressure ratio of 30 was found at the shock-on-lip Mach number of 3.2. The Mach 3.2 inviscid solution was validated using NASA's OVERFLOW2 CFD tool. In addition, the full viscous solution was performed using OVERFLOW2 and the results demonstrated why the original SR-71 employed a boundary layer bleed on the centerbody—the interaction of the initial reflected shockwave with the boundary layer caused the boundary layer to separate and the inlet unstated.

Five modifications to the inlet were then proposed and their high speed performance ( $> \text{Mach } 3.2$ ) was evaluated. Two schemes, the variable cowl leading edge and the variable cone centerbody, performed poorly—the former would unstart at Mach 4.0, the latter at Mach 3.5. The simplest (and least expensive) redesign method, the re-extended spike, demonstrated the ability to remain self-started until about Mach 4.8. However, the flowfield properties were highly distorted because the initial reflected cowl shock moved all the way around the shoulder of the centerbody causing rather significant gradients in the flow.

The remaining two schemes, the widened shoulder centerbody and the variable cone with re-extension, showed some promise. The widened shoulder centerbody was able to remain self-started (with a healthy buffer from the Kantrowitz limit) up to the maximum constrained Mach number of 6.1, while the variable cone with re-extension remained self started through Mach 7.2. Both inlets displayed comparable flowfield properties at the exit plane as shown in Figures 6.1 and 6.2. The Mach number entering the throat started around Mach 2.0 and increased at the same rate for both inlets. Similarly, for both inlets the temperature ratio entering the throat started at about 1.8, decreased, and then increased at about the same rate. Likewise, the pressure ratio entering the throat started at about 7.7, decreased, and then increased at similar rates. The main difference in the throat entrance properties between the two schemes is that the total pressure ratio is consistently higher for the widened shoulder centerbody and that the distortion levels for the variable cone with re-extension scheme are steadily lower. Figure 6.2 illustrates that the area-averaged subsonic flow properties are fundamentally the same for both schemes. The final

figure also shows that both of these inlets exhibited very large levels of static temperature and pressure at the throat exit at higher speeds suggesting that transition to scramjet operation could be possible.

The overriding conclusion of this work is that complex variable geometry is probably needed in order to design an inlet that is operable over a span of flight speeds that ranges from the low supersonic regime into the hypersonic corridor. The mechanical complexity associated with the complex variable geometry is the main obstacle that would need to be overcome to realize either of the two promising redesign schemes developed in this work. This point underscores the difficulty in constructing a single common inlet that would properly feed the three cycles of a TBCC engine. More detailed flow analysis, including viscous and boundary layer control, is needed to better quantify the flowfield properties and self-starting characteristics of both concepts. Finally, coupling this numerical tool to gas turbine, ramjet and scramjet models is essential.

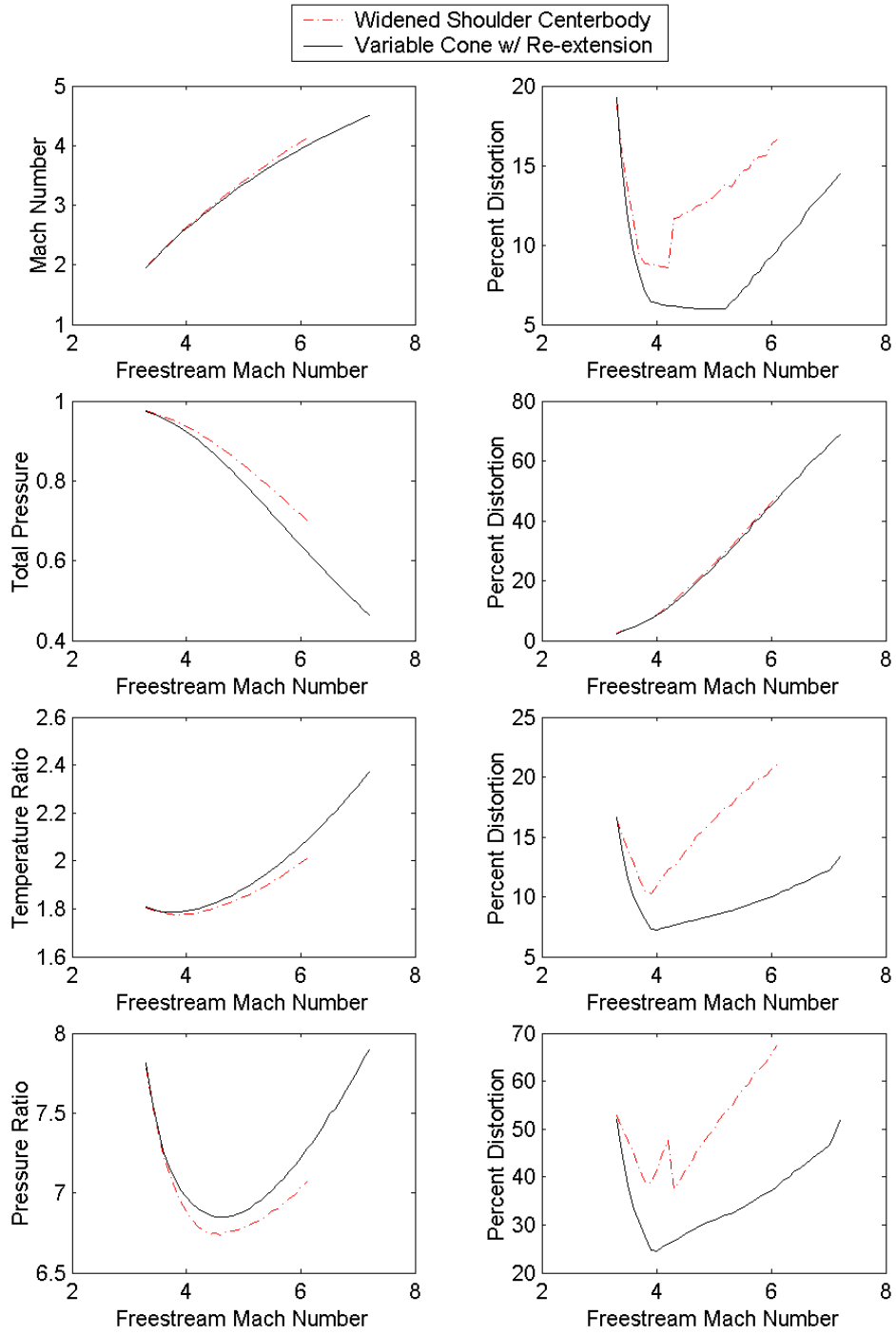


Figure 6.1 Comparison of Area-Averaged Supersonic Throat Properties

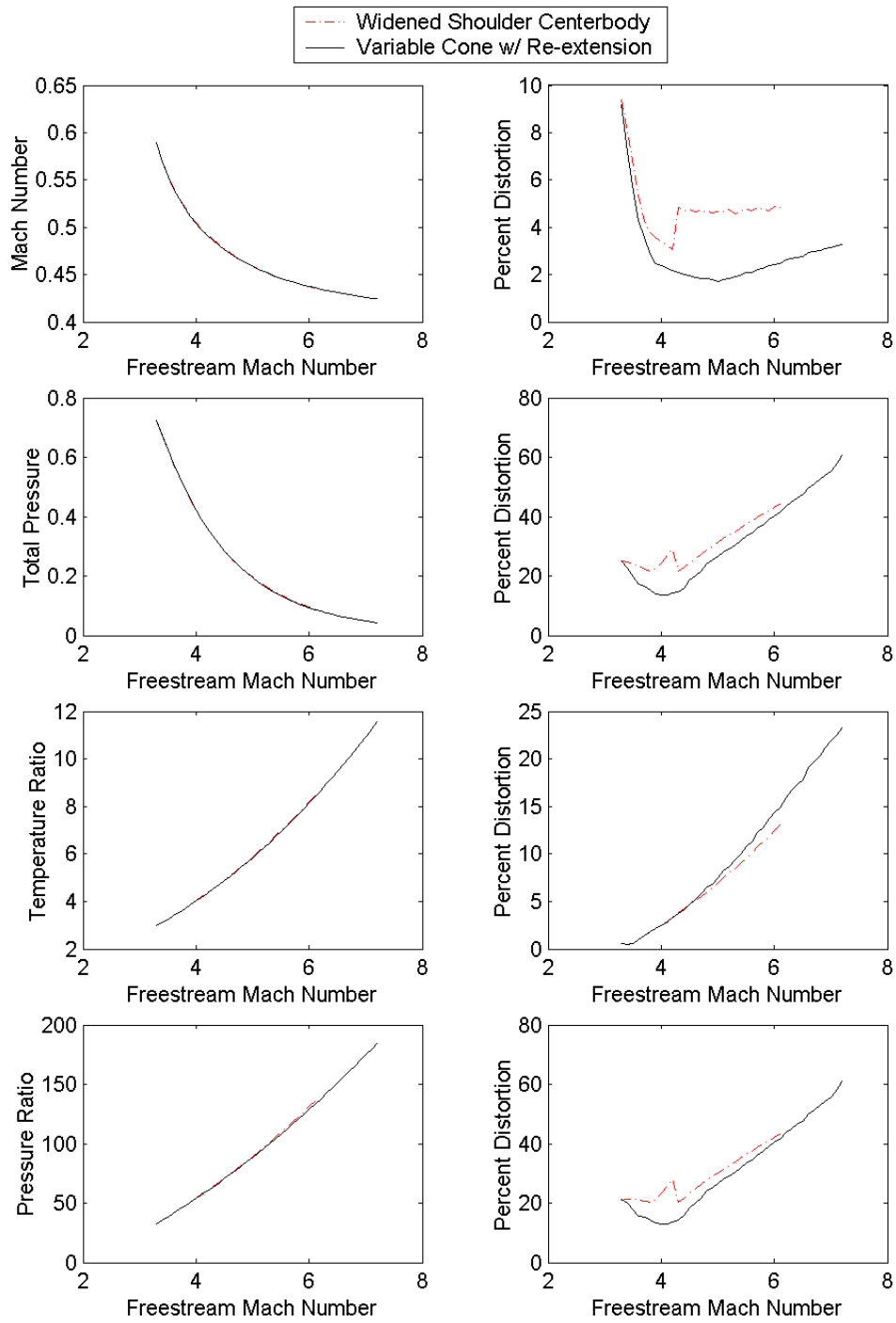


Figure 6.2 Comparison of Area-Averaged Subsonic Throat Properties

## 7 Future Work

This work is believed to be a first step in the development of future turbine-based, combined-cycle engine inlets. However, as with any ongoing research venture, there are several aspects of the process that could use some improvement. Recommendations for improvement to this research project are listed in the following sections.

### 7.1 Model Modifications

Improvements to the method of characteristics code are given below (in no particular order of importance):

- The ratio of specific heats ( $\gamma$ ) was held constant throughout the entire process, even in regions of very high temperatures. Modification of the MOC solution to include the variations in gamma should be done. However, including the variation in gamma also requires the code to be modified to calculate the actual thermodynamic properties instead of ratios. Accordingly, freestream properties would be needed so flying an assumed trajectory (or integrating the trajectory into the code) should be

included.

- Improvement of the triple point calculation is a necessity. Violation of the pressure constraint, while in theory may be correct, produces a highly distorted flow and does not allow for a clear understanding of the design strengths. Likewise, it is doubtful that the strong shockwave angles will be constant on either side of the triple point. Finding (or developing) an analytical method to predict the variation in the shockwave angles above and below the triple point to go along with the MOC solution is a must.
- Viscous effects (as seen in Chapter 4) play a major role in the design of inlets. A simple boundary layer model could be added to the MOC solution; however, an analytical means must then be incorporated to predict the effects of shockwave-boundary layer interaction. Nevertheless, CFD could play a huge role here as well.
- Incorporate the calculation of drag (both internal and external) into the solution.
- Analytically resolve the subsonic portion of the inlet downstream of the throat (it was ignored in this report).
- The code cannot currently handle any case in which a shockwave is canceled so that the remaining flow is isentropic. It should be modified to allow for such a case.

## 7.2 Future Research Topics

Recommendations for future research topics include:

- The current report uses the SR-71 inlet as a baseline and suggests only five re-design schemes to make the inlet a true TBCC inlet. Obviously, there are many other concepts that could be considered (such as isentropic compression) and analyzed and compared to the present work. A modification to the present work would be to allow for the throat area and re-extension limits to be unconstrained and to optimize the designs based upon the starting criteria and throat flow properties.
- Incorporate an engine model into the program so that the inlet can match the engine needs. This allows for the coupling of the design of both the engine and the inlet.
- Research the transition from ramjet to scramjet. As is shown in this work, it would be unwise for the analyzed re-designs schemes to be operated in ramjet mode only at the higher speeds.
- CFD analysis was not done until the very end of the project. In hindsight, it should have been performed in conjunction with the MOC solution much earlier in the research process as the run times were not as slow as originally perceived. This would allow for research into bleed and/or bypass schemes for flow control to prevent the problems associated with shockwave-boundary layer interaction. It would also be desirable to perform time accurate CFD analysis with a moving grid for the entire range of SR-71 Mach number to allow the inlet to start at the low Mach numbers and remain started throughout the entire flight profile.

Additionally, it would be an interesting project to somehow reverse engineer the suction schedule of the original bleed system on the SR-71 inlet. Furthermore, CFD should be used to preview the viscous effects of the initial reflected cowl shock moving up and around the shoulder of the centerbody in the proposed modifications and to then (based upon the suction schedule used on the SR-71) somehow control the interaction.

## Bibliography

1. Clough, J., *Modeling and Optimization of Turbine Based Combined Cycle Engine Performance*, Master's Thesis, University of Maryland, 2004.
2. Seddon, J., and Goldsmith, E. L. *Intake Aerodynamics*. 2<sup>nd</sup> Ed. AIAA Education Series, Reston, VA, 1999.
3. Seddon, J., and Goldsmith, Eds. *Practical Intake Aerodynamic Design*. AIAA Education Series, Reston, VA, 1993.
4. Mahoney, J.J., *Inlets for Supersonic Missiles*, AIAA Education Series, 1990.
5. Fernandez, R., Reddy, D. R., Benson, T. J., Iek, C., Biesiadny, T. J., and Wendt, B. J., "Design Issues for Turbine-Based and Rocket-Based Combined Cycle Propulsion System Inlets," 34<sup>th</sup> AIAA/ASME/SAE/ASEE Joint Propulsion Conference & Exhibit, Cleveland, AIAA-98-3774, July 1998
6. Hill, P. G., and Peterson, C. R., *Mechanics and Thermodynamics of Propulsion*. 2<sup>nd</sup> Ed. Addison-Wesley, Reading, MA, 1992.
7. Kantrowitz, A., and Donaldson, C. "Preliminary Investigation of Supersonic Diffusers." NACA ACR L5D20
8. Van Wie, D.M., "Scramjet Inlets", Chapter 7, *Scramjet Propulsion*, Progress

- in *Astronautics and Aeronautics*, Vol. 189, Ed. Curran, E.T., and Murthy, S.N.B., 2000.
9. *SR-71 Online Aircraft Museum*. <http://www.sr-71.org>
  10. Anderson, E. C., and Lopata, J. B. “Using a Modified SR-71 Aircraft and Air-Launched Expendable Rockets to Place Small Payloads into Orbit.” 32<sup>nd</sup> AIAA/ASME/SAE/ASEE Joint Propulsion Conference and Exhibit, Lake Buena Vista, FL, July 1996. AIAA 96-2774
  11. Anderson, E. C., Lopata, J. B., Hoar, P. R., Nelson, D., “Performance Analysis and Optimized Design of an SR-71 Based Air Launch System for Small Payloads.” 33<sup>rd</sup> AIAA/ASME/SAE/ASEE Joint Propulsion Conference and Exhibit, Seattle, WA, July 1997. AIAA 97-36557.
  12. Rich, B. *Skunk Works: A Personal Memoir of my years at Lockheed*. Little, Brown and Co. New York: 1994.
  13. *SR-71 Flight Manual*. <http://www.sr-71.org/blackbird/manual/index.htm>
  14. Reukauf, P. J., Burcham, F. W., Holzman, J. K., “Status of a Digital Integrated Propulsion/Flight Control System for the YF-12 Airplane.” AIAA Paper 75-1180.
  15. Syberg, J, and Hickcox, T. E., “Design of a Bleed System for a Mach 3.5 Inlet.” NASA CR-2187, 1972.
  16. Cole, G. L., Dustin, M. O., Niener, G. H. “A Throat-Bypass Stability System for a YF-12 Aircraft Research using Self-Acting Mechanical Valves.” NASA TM-X-71779, 1975.
  17. Cole, G. L., Dustin, M. O., Niener, G. H. “Continuous-Output Terminal-

- Shock-Position Sensor for Mixed Compression Inlets Evaluated in Wind Tunnel Tests of YF-12 Aircraft Inlet.” NASA TM-X-3144, 1974.
18. Miller, J. *Lockheed Martin's Skunk Works*. Rev. Ed. Midland Publishing Ltd., England, 1995.
  19. Lockheed D-21 Drone. <http://www.wvi.com/~sr71webmaster/d21~1.htm>
  20. Lockheed Martin Astronautics—Huntsville Operations. “Study on the Modifications Required to Re-engine the Lockheed D-21 Drone.” NASA Doc. N19990110312, October, 1999
  21. Saunders, B. W. and Weir, L. J. “Advanced Technology Inlet Design, NRA 8-21 Cycle II: DRACO Flowpath Hypersonic Inlet Design.” NASA TR-121499. December, 1999.
  22. Andrews, E. H. and Mackley, E. A., “Review of NASA’s Hypersonic Research Engine Project.” 29<sup>th</sup> AIAA/ASME/SAE/ASEE Joint Propulsion Conference and Exhibit, Monterey, CA, June 1993. AIAA 93-2323.
  23. NASA Langley. <http://hapb-www.larc.nasa.gov/Public/Engines/Hre/Hre.html>
  24. Hsia, Y-C. “Full Navier-Stokes Analysis of an Axisymmetric Scramjet Inlet.” *Journal of Propulsion and Power*, Vol. 9, No. 6, 1993.
  25. Andrews, W. H. “Summary of Preliminary Data Derived from the Xb-70 Airplanes.” NASA-TM-X-1240, 1966.
  26. Gallagher, R. J. “Investigation of a Digital Simulation of the Xb-70 Inlet and its Application to Flight-Experienced Free-Stream Disturbances at Mach Number of 2.4 to 2.6.” NASA-TN-D-5827, 1970.
  27. Candel, S. “Concorde and the Future of Supersonic Transport.” *Journal of*

*Propulsion and Power*. Vol. 20, No. 1, 2004.

28. Rettie, I. H. and Lewis, W.G. "Design and Development of an Air Intake for a Supersonic Transport Aircraft." *Journal of Aircraft*. Vol. 5, no 6, 1968.
29. Ferri, Antonio. "The Method of Characteristics." *High Speed Aerodynamics and Jet Propulsion. Vol. VI. General Theory of High Speed Aerodynamics*. Sec. G. W.R. Sears, ed., Princeton University Press, 1954, pp. 583-668.
30. Ferri, Antonio. "Application of the Method of Characteristics to Supersonic Rotational Flow." NACA TR-841, 1946.
31. Taylor, G. I., and Maccoll, J. W., "The Air Pressure on a Cone Moving at High Speed," *Proc. Roy. Soc.*, Vol. 139, 1933, pp. 278-311.
32. Canale, R. P., and Chapra, S. C., *Numerical Methods for Engineers*. 3<sup>rd</sup> Ed. McGraw-Hill Inc, New York, 1998.
33. Anderson, J. D., *Modern Compressible Flow with Historical Perspective*. 3<sup>rd</sup> Ed. McGraw-Hill, Inc, New York, 2003.
34. Connors, J. F., and Meyer, R. C. "Design Criteria for Axisymmetric and Two-Dimensional Supersonic Inlets and Exits." NACA TN 3589, 1956.
35. Wellmann, J. "Vereinfachung van Rechnungen am schiefen Verdichtungsstoß," *Deutsche Luft und Raumfahrt*, Jan. 1972.
36. vonEggers Rudd, J., and Lewis, M. J., "Comparison of Shock Calculation Methods," *Journal of Aircraft*. Vol. 35, No. 4, July-Aug. 1998.
37. Johnson, H. J. and Montoya, E. J. "Local Flow Measurements at the Inlet Spike Tip of a Mach 3 Supersonic Cruise Airplane." NASA-TN-D-6987, 1973.

38. Cole, G. L., Cwynar, D. S., Geysler, L. C. "Wind-Tunnel Evaluation of the Response of a YF-12 Aircraft Flight Inlet to Internal Airflow Perturbations by Frequency-Response Testing." NASA-TM-X-3141, 1974.
39. Tomaro, R. F. and Wurtzler, K. E., "High Speed Configuration Aerodynamics: SR-721 to SMV," *17<sup>th</sup> Applied Aerodynamics Conference*, Norfolk, VA, July 1999, AIAA-99-3204.
40. Buning, P. G., Jespersen, D. C., Pulliam, T. H., Chan, W. M., Slotnick, J. P., Krist, S. E., and Renze, K. J., "Overflow User's Manual." Version 1.8aa. NASA Langley Research Center, 2003.
41. Chan, W. M., Chiu, I.-T., and Buning, P. G., "User's Manual for the HYP-GEN Hyperbolic Grid Generator and the HGUI Graphical User Interface," NASA TM 108791, 1993.
42. Skunk Works Digest, Vol. 2, Num. 56. <http://www.netwrx1.com/skunk-works/v02.n056>
43. New Oregon Trail: SR-71. <http://www.neworegontrail.com/sr-71.htm>
44. McIninch, T. P., "The Oxcart Story," Central Intelligence Agency website [http://www.odci.gov/csi/kent\\_csi/docs/v15i1a01p\\_0023.htm](http://www.odci.gov/csi/kent_csi/docs/v15i1a01p_0023.htm)